# Optical Measurements of Viscous Interactions on a Hollow-Cylinder / Flare in a Mach 4 Freestream

A Thesis Presented for the

Master of Science

Degree

The University of Tennessee, Knoxville

Jack William Cobourn

December 2020

Copyright © by Jack William Cobourn, 2020
All Rights Reserved.

*To my family, thank you for all your support.*

# Acknowledgments

This manuscript is based on research supported by the Office of Naval Research under award number N00014-19-1-22421. I would like to thank Mark Gragston and Andrew Ceruzzi for their assistance in designing the FLDI system and Lauren Lester, Haley Goldston, and Kate Stamper for their help in conducting experiments. I would further like to thank Kirk Davenport, for his assistance in conducting experiments and experimental design and Gary Payne and Jack LeGeune for their assistance in fabrication of the test models.

Further, I would like to thank my family for their constant and continued support throughout my academic career.

# Abstract

Despite decades of research, shock-wave/boundary-layer interactions and laminar-turbulent transition remain uncertainties in the design of hypersonic vehicles. Due to the significant demand for hypersonic capabilities and the relevance of these flow physics to air-breathing, high-lift, hypersonic vehicles, continued study is necessary. In order to support such study at the University of Tennessee Space Institute, two optical diagnostics were investigated for use in the Mach 4 Ludwig tube at the Tennessee Aerothermal Laboratory, focused laser differential interferometry and schlieren. Significant attention was given to the theory behind and application of focused laser differential interferometry to support future work at the University of Tennessee Space Institute. These diagnostics were constructed and utilized in two studies, one investigating a laminar shock-wave/boundary-layer interaction on an axisymmetric hollow cylinder flare geometry, and one tracking the boundary layer transition along a hollow cylinder. Results of these studies show that FLDI and schlieren are an effective method for the non-intrusive study of boundary layer structure and breakdown, and show promising use for the study of shock-wave/boundary-layer interactions. Reported results include spectral distributions from the boundary layer, separation region, and reattachment region of a laminar shock-wave/boundary-layer interaction and from laminar, transitional, and fully turbulent regions in a boundary layer. In this study, the boundary layer was found to transition at a local Reynolds number of $Re = 1.71 \times 10^5$ and gave way to fully turbulent behavior at $Re = 3.34 \times 10^5$.

# Table of Contents


**1 Motivation** **1**

1.1 A Brief History of Hypersonics . . . . . 1

1.1.1 A 'New' Arms Race? . . . . . 3

1.2 The Current Field of Hypersonics and Hypersonic Research . . . . . 10

1.2.1 Hypersonic Viscous Interactions . . . . . 10

1.3 The Case for Focused Laser Differential Interferometry . . . . . 14

1.3.1 Optical Diagnostics . . . . . 16

1.4 Other Experimental Considerations . . . . . 18

1.4.1 High-speed Wind Tunnels . . . . . 18

1.4.2 Hypersonic Aerospace Models . . . . . 18

**2 Literature Review** **20**

2.1 Hypersonic Viscous Phenomena . . . . . 20

2.1.1 The Hypersonic Boundary Layer . . . . . 20

2.1.2 Shock Wave/Boundary-Layer Interactions (SBLI) . . . . . 22

2.1.3 The Hollow Cylinder Flare Geometry . . . . . 22

2.2 Diagnostics: FLDI and Schlieren . . . . . 24

2.2.1 Laser Differential Interferometry . . . . . 24

2.2.2 Focused Laser Differential Interferometry . . . . . 33

2.2.3 2-Point Focused Laser Differential Interferometry . . . . . 36

2.2.4 High-speed Schlieren . . . . . 37

**3 Experimental Methodology** **38**
3.1 Facility . . . 38
3.1.1 UTSI TALon Mach 4 Tunnel . . . 38
3.2 Models . . . 39
3.2.1 Hollow Cylinder Flare . . . 39
3.2.2 Hollow Cylinder . . . 46
3.3 Diagnostics . . . 46
3.3.1 2-Point Focused Laser Differential Interferometry . . . 48
3.3.2 Schlieren Systems . . . 55
3.4 Uncertainty Quantification . . . 56
3.4.1 Photo-diode response . . . 56

**4 Results** **62**
4.1 Hollow Cylinder Flare . . . 62
4.1.1 Schlieren . . . 62
4.1.2 FLDI . . . 62
4.2 Hollow Cylinder . . . 69
4.2.1 Schlieren . . . 69
4.2.2 FLDI . . . 74

**5 Conclusions and Future Work** **79**
5.1 Conclusion . . . 79
5.2 Future Work . . . 80
5.2.1 FLDI Study of Transitional SBLI and Upstream Influence Shock . . . 81
5.2.2 Improvements to FLDI Apparatus . . . 81
5.2.3 Interferometric Schlieren . . . 81

**Bibliography** **83**

**Appendices** **95**

**Vita** **99**

# List of Tables

2.1 Sellmeier equation coefficients for quartz ($SiO_2$). . . . . 30

3.1 List of FLDI Components . . . . . 49

# List of Figures


1.1 The X-15 in flight. . . . . 2
1.2 Tripped boundary layer test during STS-119. . . . . 4
1.3 Recent covers of Aerospace America and Aviation Week. . . . . 5
1.4 Hypersonic vehicles are capable of defeating detection and defense systems. . 8
1.5 US and Russian Hypersonic Vehicles. . . . . 11
1.6 Comparison of the technological challenges in HGV and HCM development. 12
1.7 Canonical SBLI test configurations . . . . . 15

2.1 Structure of a compression ramp or flare SBLI . . . . . 23
2.2 A schematic of a typical LDI . . . . . 26
2.3 A schematic of a typical two crystal birefringent Wollaston prism . . . . . 32
2.4 a schematic of an FLDI . . . . . 34
2.5 Comparison of turbulent intensity calculations using HWA and FLDI . . . . 35

3.1 Recorded pressures in the TALon Mach 4 facility. . . . . 40
3.2 The Mach 4 Ludwig Tube at TALon. . . . . 41
3.3 Diagram of the TALon facility optical stands . . . . . 42
3.4 Photograph and 2-D CAD schematic of the UTSI Hollow Cylinder Flare model. 44
3.5 Roughness measured on the HCF model . . . . . 45
3.6 Photograph and 2-D CAD schematic of the UTSI Hollow Cylinder model. . . 47
3.7 A schematic of the UTSI 2-point FLDI system, with integrated schlieren. . . 50
3.8 Photographs of UTSI FLDI as installed in the TALon Mach 4 Ludwieg Tube. 51
3.9 Results from sensitivity study . . . . . 53
3.10 Measurement of beam separation with beam profiler. . . . . 54

3.11 Photographs of UTSI integrated schlieren system . . . . . 57
3.12 Frequency response of PDA36A2 Photo-diode, used in this experiment, with no gain, as calculated from response to 1 ns square wave. . . . . 59
3.13 Frequency response of PDA36A2 Photo-diode, used in this experiment, with 10 dB gain, as calculated from response to 1 ns square wave. . . . . 60
3.14 Frequency response of example short rise-time Photo-diode as calculated from response to 1 ns square wave. . . . . 61

4.1 A montage of the flow around the Hollow Cylinder Flare. . . . . 63
4.2 Color waterfall plot of HCF runs . . . . . 65
4.3 Spectra from FLDI measurements along HCF Model . . . . . 67
4.4 A montage of integrated schlieren of the Hollow Cylinder Flare reattachment. 68
4.5 A montage of the flow around the Hollow Cylinder. . . . . 70
4.6 Calculated boundary layer height along the hollow cylinder model. . . . . 71
4.7 Schleiren image colored with low frequency fluctuation intensity . . . . . 72
4.8 Spectra extracted from Schleiren on the Hollow Cylinder. . . . . 73
4.9 A montage of the boundary layer above the Hollow Cylinder . . . . . 75
4.10 Color waterfall plot of HC runs, using calculated local Re . . . . . 76
4.11 Spectra calculated using 2-point FLDI along the HC model. . . . . 77
4.12 Spectrogram of 2-point FLDI measurement along the Hollow Cylinder model. 78

# Chapter 1

# Motivation

To what degree can optical diagnostics determine the state of a Mach 4 axisymmetric boundary-layer? Motivation of this question requires background in the field of hypersonics and the current drive for further research, as well as the physics and diagnostics involved.

Hypersonics refers the atmospheric flight above Mach 5, five times the speed of sound, along with its corresponding technologies. Unlike the field of supersonics, hypersonics does not have a distinct bright-line demarcating a change in physics. Instead, hypersonic flow introduces several physical phenomena that complicate design in, and analysis of, the hypersonic flow regime; which increase in number and severity as Mach number and flow enthalpy increases. In general, a flow is considered hypersonic when these phenomena, such as non-equilibrium gas chemistry and temperature, rarefaction to the point of non-continuum flow, and extreme aero-structure interaction, significantly effect flow physics[2, p. 15]. Hypersonics has a long history of research in the United States (US), the USSR, continued by the Russian Federation (Russia), and by the People's Republic of China (China).

## 1.1 A Brief History of Hypersonics

The age of hypersonics is generally considered to begin with the flight of the X-15 hypersonic research vehicle in June 1959, a rocket propelled space-plane platform for testing scramjets and other hypersonic technologies [8]. The X-15 is depicted in flight in fig. 1.1[76]. This and




**Figure 1.1:** The X-15A-3 in flight during a mission in the 1960s. Many consider the first flight of the X-15 the beginning of the field of hypersonics[76].

other early hypersonics programs, though successful research platforms, often discovered so-called 'unknown unknowns', at significant cost. This research occurred against the backdrop of Intercontinental Ballistic Missiles (ICBMs), which had outpaced high-speed bomber aircraft, and were considered effectively unstoppable. By being mutually unstoppable, ICBMs kept the strategic threat of nuclear arms relatively balanced. This concept is referred to as 'mutually assured destruction.' This balance, coupled with the significant availability of and research into ballistic missiles, allowed the great powers to shift from an arms race to a space race. High-velocity flows continued to be studied significantly, but with the goal of decreasing the cost of access to space, or, occasionally, increasing the speed of travel. This result in a significant preference for the study of low lift-to-drag (L/D) capsule-type reentry vehicles over more expensive maneuverable options [8].

In the 1970s and 1980s the Space Shuttle was intended to be a solution to the cost of access to space. The Space Shuttle should be thought of as the first fully realized hypersonic vehicle, and much of the results the huge research effort supporting its design and continued use is fundamental to our understanding of hypersonic flows today. Figure 1.2 demonstrates results from one such experiment [18]. However, the Space Shuttle program, with its significant turn-around time between flights, was unable to sufficiently decrease the cost of access to space. As the historical motivator for hypersonics research, decrease in cost (or dreams of hypersonic airlines) has resulted in hypersonic research being closely tied to particular technology systems or applications. This has lead to a roughly 15-year boom-and-bust cycle in the hypersonics field. However, neither reducing the cost of access to space nor speed for its own sake is the primary driver of the renewed interest in hypersonics beginning in the early 2000's, although eventually hypersonics research may contribute to decreases in the cost of space access.

### 1.1.1 A 'New' Arms Race?

Rather, the renewed interest in high speed, low-altitude, highly maneuverable vehicles is driven by a defense motivation, both in the US and abroad. The idea of defense applications for hypersonic systems is not new, due to their unique use at the onset of hostilities and against time critical targets [8]; however overcoming the boom-and-bust cycle required

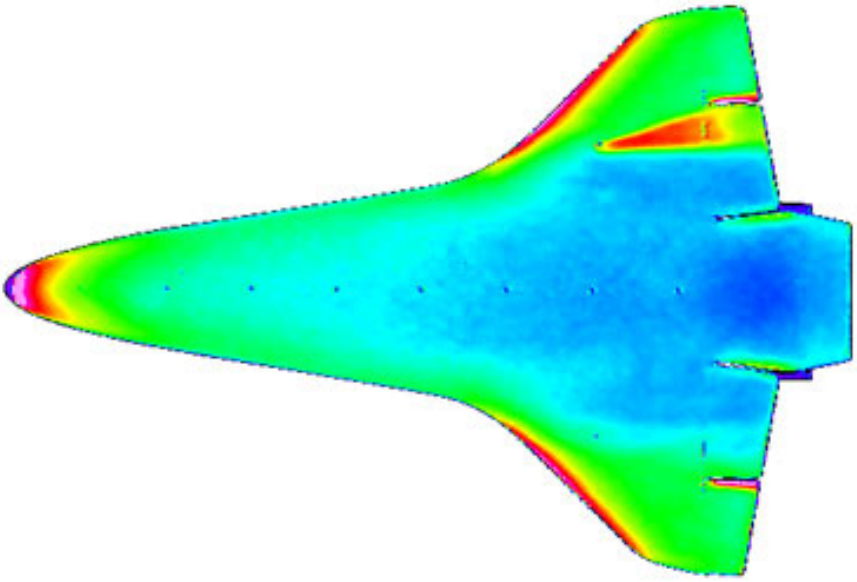


**Figure 1.2:** Tripped boundary layer test during 2009 space shuttle flight STS-119 [18].




**(a)** Aerospace America [11].




**(b)** Aviation Week & Space Technology [46].

**Figure 1.3:** Recent covers of Aerospace America and Aviation Week suggest a new hypersonics arms race.

something more poignant. Development and rapid deployment of US hypersonics systems has become a primary goal for the DoD due to the fact that that Russia and China are expected to field hypersonic weapons as soon as this year, 2020 [57]. As the news articles in fig. 1.3 suggest, hypersonics has been turned into an arms race and there is significant interest in these vehicles.

### Nuclear Deterrence

Russian and Chinese motivations are a bit more nuanced however. An outside observer might ask, "What prompted the initial investment by China?" First, it must be noted that several Russian and Chinese systems are not simply 'conventionally armed'. 'Conventionally armed' refers to weapons containing high explosives (containing their own oxidizer) or fuel-air explosives (which combust with air). In the context of hypersonic vehicles, a conventionally armed system would merely be kinetic, converting it's kinetic energy into heat upon impact, as the added weight of conventional explosives would be unnecessary. However, the Chinese armed forces have, and Russian's are considering, optional nuclear payloads for their hypersonic weapons.

This is generally considered to be a response to US anti-ICBM missile defense increasing in number, quality, and coverage area, disrupting the 'balanced' nature of nuclear arms. Thus hypersonic nuclear weapons could be said to re-establish the 'at-risk' nature of nuclear arms [57, p. 9]. Russia may also be motivated by the US withdraw from the Anti-Ballistic Missile Treaty in 2001[1]. It should be noted that the US does not have a defense network capable of defending against the Russian or Chinese nuclear arsenals. The stated purpose of the US "Ground-Based, Mid-Course Defense" (GMD) system is to defend from nuclear threats from countries with small nuclear arsenals, such as Iran and North Korea. Simply put, the 44 kinetic Ground-Based Interceptors of the GMD pale in comparison to the 1550 deployed warheads permitted to Russia in the 2010 New START Treaty [48]. For these and several other reasons, e.g. Russia's ability to spend on hypersonic research, many question the veracity of Russian claims to their progress in fielding hypersonic systems [11, 57]. China's arsenal is much smaller than Russia's, consisting of 125 missiles, but is more focused on regional capabilities. Regional Defense systems including the Terminal High Altitude Area

Defense (THAAD), the Aegis Weapon System, and the Patriot Advanced Capability-3 (PAC-3), placed with US allies throughout Europe and the pacific, leave the US defenses and China's missiles more evenly matched, leaving prime territory for an arms race.

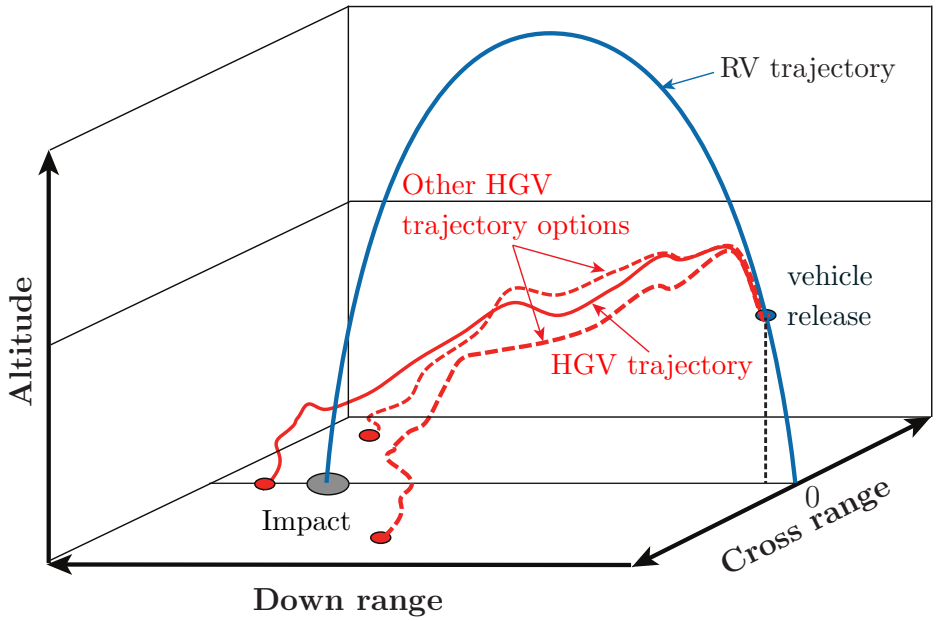
Regardless, current US defense or detection systems would not be effective against hypersonic weapons due to their 10 to 20 times smaller signature from space, unpredictable trajectories, and the effect of being below the horizon of ground based systems for much of their flight path[57], although anti-hypersonic technologies are being explored [48]. See fig. 1.4b [57] for illustrations of how hypersonic weapons defeat conventional detection.

A hypersonic weapon with a nuclear payload has a significantly alters the implications of hypersonic weapons. Such a system could be 10 to 100 times less accurate then a conventional kinetic system and still achieve its aims. A regional use of a nuclear armed hypersonic missile would likely have global implications, and confusion between conventional and nuclear uses, due to the co-mingling of the two systems, may lead to unintended escalations[65]. Speier et al. [65] also notes that the speed of such a system creates the feasibility, and therefore expectation, of a preemptive attack aimed at disarming the enemy. Such a threat encourages a 'launch-on warning' posture, a strategy in which a retaliatory attack is launched before incoming missiles have reached their targets. This is further complicated by the aforementioned unpredictability of the target of hypersonic vehicles (fig. 1.4a [65, 25]). Together these effects work to introduce real threat to global nuclear stability [35]. For these reasons Hypersonic systems cannot be considered outside the context of nuclear deterrence, arms races and control, etc. The US is not currently considering any nuclear armed hypersonic systems [57]. How this fact will affect the uses and proliferation of hypersonic technologies remains to be seen.

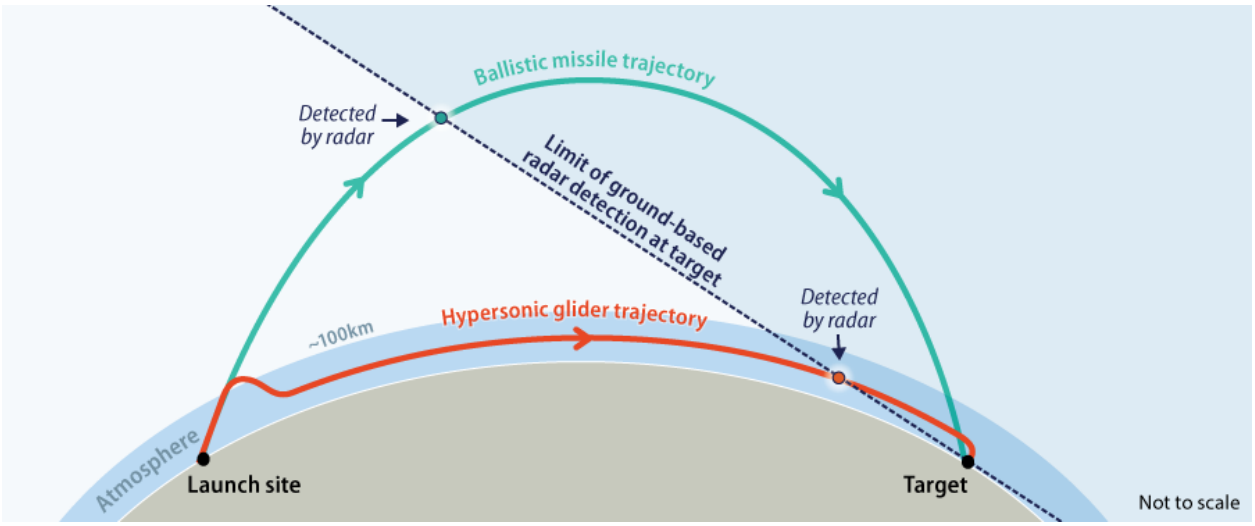
### Force Projection in the South China Sea

Increasing regional conflict between China and the US and its allies in the South China Sea (SCS) is worth particular mention. Trillions of dollars in commerce flow through the region annually [78]. Historically, and through today [63], the US has used the Navy to protect

[1]The motivation for withdrawal from the treaty was the creation of the GMD system, and therefore defense against blackmail by countries with small nuclear arsenals.




**(a)** Hypersonic Vehicles can avoid defenses with unpredictable 'evasive maneuvers'. Their intended target is also obscured. Figure based on [65, 25], here HGV is hypersonic glide vehicle (see section 1.1.1), and RV is the ballistic reentry vehicle that the hypersonic vehicle is released from.




**(b)** Hypersonic vehicles can avoid detection by ground based radar technologies with trajectories below the horizon [57].

**Figure 1.4:** Hypersonic vehicles are capable of defeating detection and defense systems intended for ballistic missiles using unpredictable trajectories, and trajectories below the horizon to ground-based radar.

its allies and interests in the region and project force internationally. China's hypersonic weapons research seems intended, along with its nuclear arsenal, to back up its claims to international waters, which are based on the construction of artificial islands in the SCS.

### Current Hypersonic Vehicles

Hypersonic vehicles are broadly classed into two main categories, which leads some to call hypersonics "The two hardest problems in Aerospace Engineering":

**Hypersonic Glide Vehicles (HGV)** are brought up to velocity by conventional rocket propelled ballistic missiles, are released in the range of 50 km to 100 km, and then maneuver to a target without self propulsion.

- HGVs represent the hypersonic equivalent of maneuvering reentry vehicles (MaRVs) developed previously for the delivery of nuclear arms; however, they differ fundamentally in that they are released from the launch vehicle while still in the atmosphere, rather than traveling a whole ballistic trajectory above 1000 km, and cannot be targeted while at a low velocity at apogee, as MaRVs are [65, 57].
- Range increases linearly with launch altitude and with the square of launch Mach number ($Ma^2$), so HGVs are launched at the top of the atmosphere, (where there is extreme rarefaction), at extreme Mach number, up to Mach 25[2](causing chemical and thermal equilibrium).
- These flow conditions challenge the limit of what is known about hypersonic flow, and require significant fundamental experimental and computational experiments on a case-by-case basis. Many rate dependent thermal and chemical energy release processes require further precise study [59].
- Examples of HGVs include a number of systems by the US Army, Navy and Air Force based on the Common Hypersonic Glide Body (C-HGB) (see fig. 1.5a), and the Russian Avangard HGV (see fig. 1.5b).

**Hypersonic Cruise Missiles (HCM)** which, after being brought up to velocity by a ballistic missile or supersonic aircraft, are able to self-propel using scramjets.

- HCMs are 'simply' very fast cruise missiles, but due to their fuel and range requirements, often must forgo the conventional rocket propulsion in favor of a supersonic combustion ramjet (SCRAM jet)[65, 57].
- HCMs travel at a lower Mach number and therefore are unlikely to experience significant effects from the extreme flow chemistry experienced by HGV, but their increased complexity results in technical issues with system integration and increased need for full characterization of the behavior and impact of laminar–turbulent transition and unsteady shock interactions [59]. Thus, the work in this study is most relevant to HCMs.

fig. 1.6 [59] demonstrates the different challenges in HGV and HCF design.

## 1.2 The Current Field of Hypersonics and Hypersonic Research

This recent renewed interest has lead to significantly increased research, investment, and progress in hypersonics [59]. Significant engineering challenges persist in the design and modeling of hypersonic vehicles, primarily due to uncertainty surrounding critical flow phenomena, e.g. scramjet unstart, aero-material interactions, and flow distortion and unsteadiness due to interaction between a shock-wave and the viscous boundary-layer on the vehicle surface.

### 1.2.1 Hypersonic Viscous Interactions

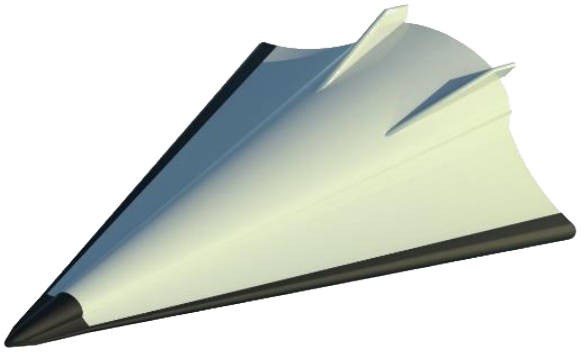
#### The Hypersonic Boundary Layer

A boundary layer is a thin region of fluid that grows around an object due to friction. Outside the boundary layer, high speed flows are inviscid, while inside the boundary layer viscous forces affect the fluid flow. In fact, early computational and engineering methods calculated the size of the boundary layer and solved these two regions separately [21]. However, this

[2] Around a launch velocity of Mach 25 an HGV can circumnavigate the globe.



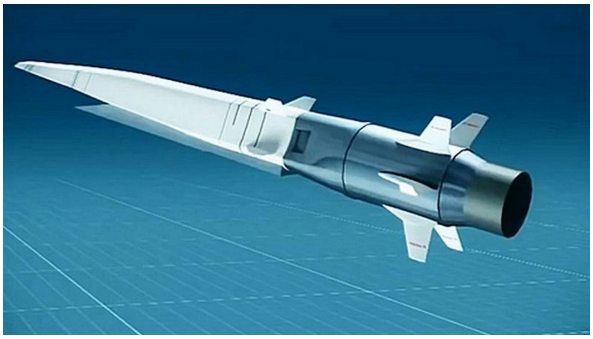
**(a)** A photograph of the US Common Hypersonic Glide Body (C-HGB), shown without a boost vehicle. [US Army]



**(b)** A computer render of the Russian Avangard HGV[57].



**(c)** A photograph of A Boeing X-51 HCM test platform at at Edwards Air Force Base in California in 2010 [40]



**(d)** An artist's rendering of the Russian 3M22 Tsirkon HCM[77].

**Figure 1.5:** Examples of US and Russian HGVs and HCMs.

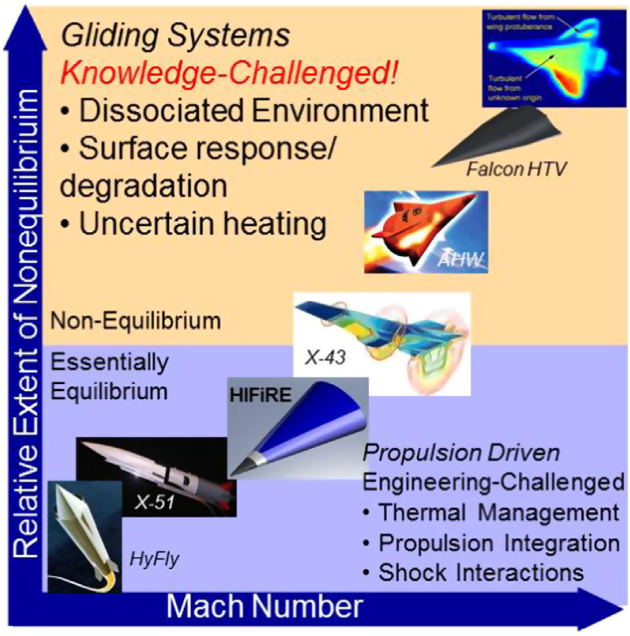



**Figure 1.6:** Comparison of the technological challenges remaining between a number of hypersonic systems. Systems whose main technical difficulties are related to flow uncertainties, shaded in peach, roughly correspond to HGVs, and systems limited by engineering challenges, shaded in blue, roughly correspond to HCMs [59].

does not provide a complete picture due to interaction between the growth of the boundary layer and the inviscid flow. The nature of the boundary layer suggests the use of the Reynolds number

$$Re = \frac{\rho \ell U}{\mu} = \frac{\ell U}{\nu} \tag{1.1}$$

Where $\rho$ is flow density, $\ell$ is a relevant length scale, $U$ is the local flow velocity, $\mu$ is the flow dynamic viscosity, and $\nu$ is the flow kinematic viscosity. The Reynolds number is a ratio of inertial forces to viscous forces in the flow [58].

Boundary layers often undergo a transition process from laminar, with smooth streamlines and no vorticity, to turbulent, characterized by random fluctuating motion, brought on by the growth of instabilities. These instabilities may originate upstream and convect into the boundary layer or develop locally due to surface roughness, heat transfer, or both. Instability growth is governed by flow parameters and is predicted with linear stability theory. Historically, much work was done in predicting transition based on the Reynolds number calculated using relevant local length scales, such as the Roughness Reynolds number $Re_k$, and although simple Reynolds number correlations are often used for transition prediction for low-speed flows, these are not sufficient for work in hypersonics [2, 33].

Understanding of the transition process is important to hypersonics as the nature of the boundary layer significantly effects the flow field around a hypersonic vehicle. A turbulent boundary layer has a number of effects on a vehicle, including substantially increasing surface heat flux, increasing mass flux near the surface, and increasing viscous drag [2, p. 345]. Furthermore, the nature of the boundary layer governs the behavior of viscous interactions such as the shock-wave/boundary-layer interaction (SBLI)[36].

This study is conducted in a Mach 4 facility. As relevant viscous phenomena are present at Mach 4, but the increasingly complex nonequilibrium phenomena prevalent at higher Mach numbers have not become significant, a Mach 4 facility is as useful tool for studying relevant flow physics. Additionally, due to the decrease in Mach number behind a shock wave, a hypersonic vehicle may have design relevant sections of flow significantly below the flight Mach number, such that observations at Mach 4 may be directly relevant to a Mach 5 to 7 vehicle. Extrapolation from low hypersonic Mach numbers is also often relevant to high

Mach number flows as phenomena such as lift and drag coefficients and flow field structure exhibit diminishing marginal difference with increasing Mach number, a behavior know as Mach number independence [2].

### The Shock-Wave/Boundary-Layer Interaction

Shock-wave/boundary-layer interactions (SBLI) have been studied for more than 70 years [36] due to the inherent risk they represent to the aero-thermodynamic performance of a high-speed vehicle. These interactions create strong thermal and pressure loads on a vehicle [27], which can lead to catastrophic failure to a variety of components, including the airframe, control surfaces, and propulsion systems. Despite extensive research, SBLI remain a source of uncertainty due to their fundamental coupling to the underlying boundary layer. In the laminar case, SBLI are inherently steady [36, 17], and can be well modeled computationally; however, the transitional and turbulent cases are inherently unsteady. Although previous work has primarily focused on turbulent shock-wave/turbulent boundary layer interactions, current efforts have increasingly focused on the interaction involving a transitional boundary layer [36] which have an increased chance of occurrence on weapon-scale hypersonic vehicles designed for extended regions of laminar flow. Figure 1.7 [27] diagrams an number of canonical SBLI test configurations and the structures they produce.

## 1.3 The Case for Focused Laser Differential Interferometry

The study of aerodynamic phenomena through experiment requires a number of real-world considerations. As flight tests are prohibitively expensive for all but the final phase of most development programs, ground test facilities must be constructed that simulate a number of flow quantities similar to the flight regime in question. It is generally considered that a ground test facility cannot match all flow characteristics; therefore, some flow quantities will be matched at the expense of others. Secondly, aerospace models must be constructed that reasonably approximate the vehicles to be evaluated or that recreate the physics to be

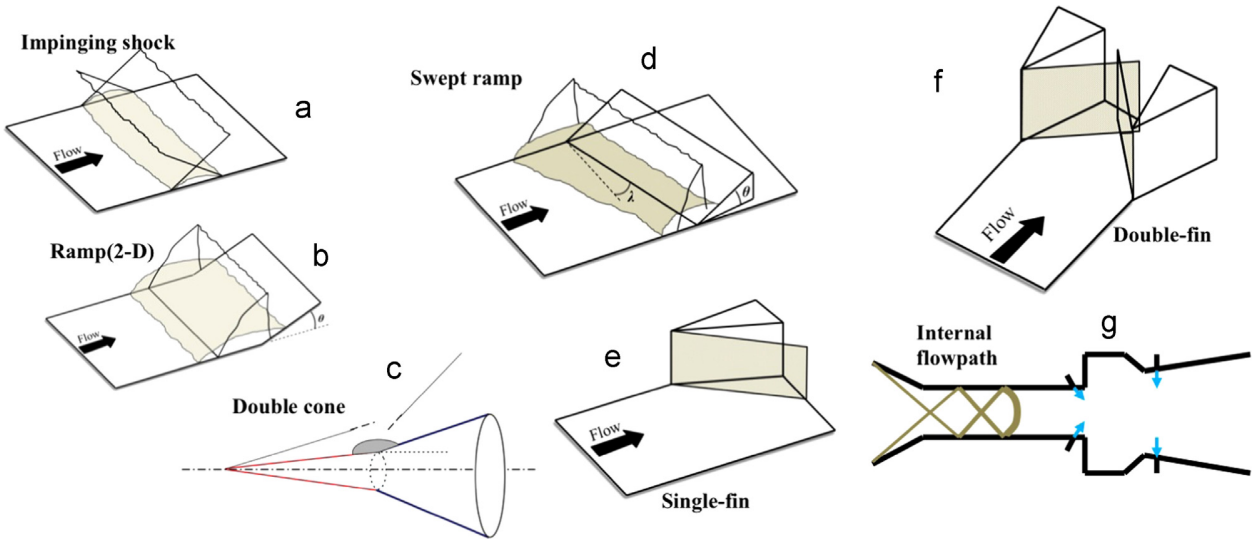



**Figure 1.7:** An illustration of a number of canonical SBLI test configurations and their flow fields [27]

studied sufficiently, are feasible to construct, and are either instrumented or lend themselves to other diagnostics. Finally, the model must be studied with a diagnostic technique that measures the desired flow quantities around the model with sufficient temporal and spatial resolution and without undo perturbations of the flow. In order to further the study of SBLI at the University of Tennessee Space Institute (UTSI), this work seeks to characterize an optical diagnostic technique, Focused Laser Differential Interferometry (FLDI), whose use is expanding rapidly in the aerospace community.

### 1.3.1 Optical Diagnostics

Optical diagnostics are a broad category of aerospace measurement techniques that employ the electromagnetic spectrum to probe flow properties based on a fluid's absorptive, emissive, or refractive properties [24]. This indirect measurement lends itself to subtle or difficult to measure phenomena, and in some cases is more simple or less costly to utilize. Advances in a number of fields, including laser technology, light-emitting diode (LED) capabilities, and data acquisition systems are rapidly making new optical diagnostic techniques possible.

#### Flow Fluctuation

Measurement of turbulent fluctuations in a flow is necessary for the study of a number of viscous phenomena. Historically,

> "For the characterization of turbulent flows, the most popular methods used in moderate supersonic flows are hot wire or film anemometry (HWA) and laser Doppler velocimetry (LDV) [9]".

HWA provides a low-cost, continuous signal of velocity and temperature fluctuation, but is fragile and intrusively perturbs the flow it is measuring. LDV has its own limitations, such as that it requires seeding the flow with particles, which is difficult in a closed system such as a Ludwig tube.

In the case of study involving a transitional boundary layer, where small perturbations are likely to grow to affect the flow, the intrusive nature of these older diagnostics may effect results. For this reason Collicott et al. [16] conclude that "...techniques to complement

hot wire anemometry [are] clearly necessary." They go on to suggest Laser Differential Interferometry (LDI), an optical diagnostic based on the refraction of laser beams passing through the test environment, as a successor to HWA.

Optical diagnostics are generally categorized by their field of view, either as collective, point, line of sight, or imaging [9, p.234]. Focusing of LDI using lenses, which is the premise of FLDI, turns it from a line of sight measurement into a point measurement, but line of sight effects remain [see section 3.3.1 or [13, 14]]. LDI and FLDI measure an approximation of the local gradient of density. A variant of the system, 2-point FLDI, as implemented in this study, additionally allows the measurement of local velocity. Although (F)LDI and HWA do not return the same parameters, their results can be related and similar conclusions. See fig. 2.5 and Fulghum [26].

### The Big Picture

One limitation of FLDI as a point optical diagnostic is that it struggles to gather information of the entire flow field, requiring many runs of a wind tunnel and often a separate complementary diagnostic to get an idea of the overall flow field. In this work, a large scale schlieren system, built along with the wind tunnel, is used for this purpose. However, drawbacks of a separate 'big-picture' diagnostic include additional facility use and diagnostic setup, as well as challenges with repeatability between experiments with different diagnostics.

For instance, a common anomaly in this work is material from the wind tunnel's mylar diaphragm passing though the test section and striking the model. Although the FLDI detects this, it is not possible to determine exactly what occurred, and large sections of data may be discarded. Further, the FLDI is not able to detect relative motion between the model, the wind tunnel, and the diagnostic itself. In order to address this drawback, a schlieren system was integrated into the FLDI so that the two diagnostics could be run simultaneously, with some success.

Schlieren is an imaging technique, and is susceptible to the general problems of imaging techniques such difficulty in extracting quantifiable information [9]. However, improvements in high speed cameras are increasingly allowing for quantitative measurement [39].

## 1.4 Other Experimental Considerations

### 1.4.1 High-speed Wind Tunnels

A number of hypersonic wind tunnel designs exist, including several intermittent designs such as blowdown, indraft, and Pressure-Vacuum tunnels, as well as continuous closed-circuit designs [53]. Ludwieg tubes are a Pressure-Vacuum intermittent tunnel design where a large driver tube is brought to high pressure and is separated from a low vacuum pressure reservoir by a diaphragm, valve, or other means. When the diaphragm ruptures, high pressure air accelerates though a converging-diverging nozzle to the appropriate Mach number, into the test section, to reach the low pressure reservoir. At the same time, an expansion fan travels backwards throughout the driver tube, reflects off the back wall and returns to the nozzle. Its arrival changes the pressure conditions at the nozzle, ending constant stagnation conditions in the test section. Thereby, the length of the driver tube determines test time. Ludwig tubes generally match their design Mach number precisely, but with extremely low enthalpy.

The Tennessee Aerothermodynamics Laboratory (TALon) at UTSI uses such a Ludwig tube. The TALon Mach 4 Ludwieg tube, currently the highest Mach number and largest facility at UTSI, is used in all experiments in this work. In the TALon Mach 4 facility, Mach 4.0 is reached precisely, at a reasonable flight $Re$, but at extremely low temperature, and thus, flow enthalpy. The facility has a constant stagnation condition run time of approximately 130 ms. This short test time precludes the use of diagnostics that do not acquire data at a very high rate of speed. The Mach 4 facility does provide ample optical access with large BK-7 glass windows. These factors further support the use of optical diagnostics. More information on the TALon facility can be found in section 3.1.1.

### 1.4.2 Hypersonic Aerospace Models

Hypersonic aerospace models are generally metal and sized to fit a specific tunnel [53, p. 284]. This work employs two aluminum, hollow, axisymmetric models, a Hollow Cylinder (HC) model and a Hollow Cylinder Flare (HCF). Aluminum models decrease cost, weight, and difficulty of construction, with less longevity and wear resistance. Section 3.2.2 discusses

how the choice of aluminum models affected this experiment. Axisymmetric hollow models are bodies of revolution that allow high speed flow to pass through their center. A hollow model allows the model to be axisymmetric without inducing conical flow, which varies in flow properties in the normal direction to the model surface [1, p. 366]. To prevent a detached bow shock from forming in front of the model, a sharp edge separates flow passing through the model and that passing around the model, and the flow inside the model must remain supersonic. The minimum area of a hollow model to maintain supersonic flow can be found with a typical diffuser calculation [1],

$$\frac{A_{t2}}{A_{t1}} = \frac{p_{o,1}}{p_{o,2}} \tag{1.2}$$

where $A_{t1}$ is the frontal area of fluid entering the model, $A_{t2}$ is the internal area of the model, accounting for losses due to boundary layer growth in the model, and $\frac{p_{o,1}}{p_{o,2}}$ is the stagnation pressure ratio across a hypothetical standing shock wave in the model.

The goal of using axisymmetric models, as opposed to the flat plate models used heretofore at UTSI, is that they allow for planer, two dimensional diagnostics while avoiding three dimensional effects [5]. That is to say, they can be considered as cylindrically-symmetric and thus still analyzed in two dimensions, and avoid sidewall and finite span interference. Further, these models lend themselves to path-integrated optical diagnostics such as schlieren and FLDI by bending flows off of the plane of interest out of the line of sight of the diagnostic.

# Chapter 2

# Literature Review

## 2.1 Hypersonic Viscous Phenomena

The modern motivations for hypersonic capabilities have lead to significant advancements in the technological and scientific knowledge bases required. The review by Schmisseur [59] outlines this progress and discusses many of the research programs that made it possible. Looking forward, the review suggests that for air-breathing vehicles, understanding the behavior and impact of boundary layer transition and unsteady shock interactions will be critical to decreasing technical risk in the design of hypersonic vehicles.

### 2.1.1 The Hypersonic Boundary Layer

As was discussed in section 1.2.1, the nature of the boundary layer is fundamental to analysis of hypersonic vehicle flow fields. Boundary layer physics, like all fluid flow, are governed by the Navier-Stokes equations, a set of five coupled partial differential equations (PDEs) describing convection of mass, momentum, and energy. In some cases these can be approximated analytically using variable transformation or order of magnitude approximation, but in general numerical methods coupled with empirical results are required, especially for turbulent boundary-layers [2].

Boundary-layer transition is a complex physical phenomena that has not been completely understood. Transition occurs over a loosely defined region of a body and its position is often

defined with an intermittency distribution. The transition location can be determined in an experiment by a number of different physical quantities that change between the laminar and turbulent region. The ones most relevant to this work are the distribution of flow velocity in the boundary layer, the growth rate of the boundary layer, and the spectrum of fluctuating content in the boundary layer.

In turbulent boundary layers, the process by which eddies are generated by viscous forces and their energy is transfered to increasingly small length scales leads to a characteristic frequency distribution when fluctuating content is measured. After a peak frequency corresponding to the largest eddies in the flow, which are on the order of the boundary layer height, the spectra rolls off with a slope of $\frac{-5}{3}$, until extremely small scale eddies are dissipated by viscous dissipation. Laminar boundary layers, without the generation of eddies, will not display such a spectrum [54].

Finally, an important behavior of boundary layers is boundary layer separation, where, due to adverse pressure gradients, the boundary layer detaches from the surface and behaves a a free-shear flow. These regions are characteristic by large-scale unsteadiness and reverse or recirculating flow [54]. Separation regions are common in the study of SBLI due to the sharp rise in pressure behind a shock wave.

### The Second Mode Instability

The second mode, or Mack mode, boundary-layer instability is a mechanism that is particularly relevant to high lift hypersonic vehicles with small nose radius, where it may be the dominant mechanism [60]. The second-mode instability is characterized by a length scale of twice the boundary layer height, and the observable 'rope-like' structures in the boundary layer. Observation of the second mode instability has been noted by a number of studies incorporating the FLDI [4] and is generally observed as a distinct peak in the turbulent spectra. The second mode instability is less prevalent at lower Mach numbers, and was not observed in this study. in a study at Mach 4.5, the second mode instability was only observed when two dimensional disturbances were introduced to the flow [41]

Instead, at lower Mach number the strongest eddies in the boundary layer are likely to be on the scale of the boundary layer height, $\delta$ [60]. In general, a non-dimensional frequency,

the Strouhal number (eq. (2.1) [80], where $\ell$ is a relevant length scale and $U$ is a relevant velocity), can be used to estimate peak frequencies in a flow field. An assumed Strouhal number of $S_t = 1$ is reasonable due to the high $Re$ of aerospace flow fields,

$$S_t = \frac{f\ell}{U} = \frac{\delta}{U} \tag{2.1}$$

### 2.1.2 Shock Wave/Boundary-Layer Interactions (SBLI)

SBLI are a phenomena of any supersonic flight regime that have been studied for over 70 years. A large number of review papers [36, 27, 22] and a book [3] have been written on the topic. Figure 2.1 diagrams the structure of a 2-D compression ramp or axisymmetric flare SBLI [27]. The typical $\lambda$-shock structure is evident, where the inviscid shock of the flare is bifurcated into a separation shock and reattachment shock, sometimes called the forward and rear shock feet. Many studies of transitional SBLI track the motion of these and other induced shocks to measure the low frequency unsteadiness of the interaction [17].

### 2.1.3 The Hollow Cylinder Flare Geometry

The hollow cylinder flare is a relatively new model geometry that is an axisymmetric representation of a hypersonic vehicle control surface or body junction. Initial work on the configuration used LDV and oil-flow, as well as CFD to begin to map out the flow field [5]. Later work analyzed the model using pressure and heat flux probes [42, 79]. This work was compared to CFD and showed good agreement [34]. At high Mach number, the model poses challenges to computational modeling due to the extreme rarefaction in the separation region, but high density behind the reattachment [61]. This work initially set out to further characterize this geometry and the SBLI it causes using FLDI.

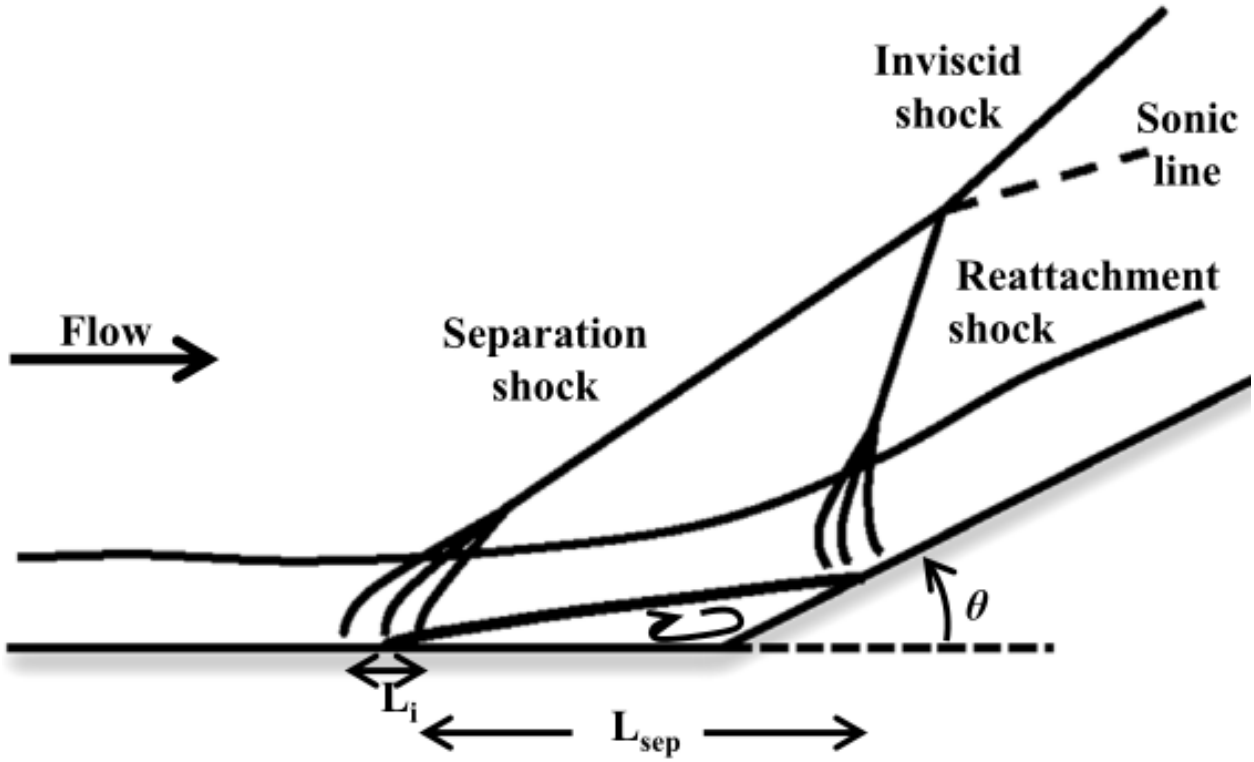



**Figure 2.1:** Structure of the shock-wave/boundary-layer interaction caused by a 2-D compression ramp or axisymmetric flare. Figure based on [27].

## 2.2 Diagnostics: FLDI and Schlieren

### 2.2.1 Laser Differential Interferometry

The report by Smeets and George [64] is the foundational work on Laser Differential Interferometry. Written in 1973 based on work beginning in 1964 at the French-German Research Institute of Saint-Louis, it was translated to English in 1996. This prompted the use of LDI, and subsequently FLDI, in the aerospace community. The report describes a generic common-path differential interferometer where Wollaston prisms are used as beam splitters. Interferometers are a broad class of instruments which use the interference of electromagnetic radiation to conduct measurement. Many interferometers function over an entire wavefront, but LDI and derived systems employ a number of distinct beams.

Two coherent monochromatic waves of lights that are superimposed will interfere. this interference will generate an illumination intensity, E, depending on the relative phase of the two beams,

$$E = E_0 \cos\left[\pi \frac{\Delta\phi}{\lambda}\right] \tag{2.2}$$

where $E_0$ is the intensity of complete constructive interference of the two beams, i.e. completely in phase, $\Delta\phi$ is the phase difference between the two beams, and $\lambda$ is the wavelength of the laser source [64]. This phase difference is often referred to as an 'optical path difference'[64, 26] although it is in fact due to differences in phase velocity between the two beams, not a travel distance as the phrase implies. As perfect interference is unlikely to be achieved in a real system, since there may be a remaining intensity, $\bar{E}$, due to misalignment, but this is insignificant so long as it remains below the order of $E$[64].

Common path interferometers such as the LDI pass both of their beams through the test medium, as opposed to the separate test beam and reference beam of double path interferometers such as the comparable Mach-Zehnder Interferometer. This makes them more robust to vibration and slight misalignment, as both beams will be effected in kind, as well as providing finer control over the system sensitivity [26]. However, it is then necessary to develop some means for the test medium to effect the two beams differently.

In the case of the Laser Differential Interferometer, a type of differential, or 'lateral-shearing', interferometer, this is achieved by the slight spatial separation, $\Delta x$, in the beams caused by the Wollaston prism. The Wollaston prism splits the beam of polarized light[1]from a HeNe laser, oriented at 45° to its axis, into two beams polarized orthogonally, i.e. vertically, generally denoted as 's', and horizontally, denoted as 'p', and cause them to refract apart at an equal angle. A pair of field lenses redirect the beams to pass parallel through the test section. In the second half of the LDI this setup is mirrored to undo this split, and re-combine the beams, and a polarizer is needed to re-match the polarization of the two beams so they can interfere. A schematic of a LDI provided by Smeets and George [64] is given in fig. 2.2.

The phase difference of such a device can be broken in to two parts[64], i.e.

$$\Delta\phi = \Delta\phi_0 + \delta\phi \tag{2.3}$$

where $\Delta\phi_0$ is due to the position of the Wollaston prisms (see section 2.2.1, page 31), and $\delta\phi$ is due to different paths traveled by the beams.

This path difference is generated by differences in the refractive index of the test medium. Light passing through materials with different refractive index will travel with a different phase velocity, $v_p$, i.e. the velocity of one part of the waveform [19], according to

$$v_p = \frac{c}{n} \tag{2.4}$$

where $c$ is the speed of light in a vacuum and $n$ is the refractive index of the material. Thus, the change in phase of a beam of light passing though some medium can be expressed as,

$$\Delta\phi = \frac{2\pi}{\lambda}\int_{s_1}^{s_2} [n(x,y,z) - n_{\text{inf}}]\, ds \tag{2.5}$$

here $\lambda$ is the wavelength, $s$ is the path of the beam, $n(x,y,z)$ defines the distribution of refractive index in the medium, and $n_{\text{inf}}$ is a reference index of refraction. In the case of two

[1]For background on polarization and polarization optics see [10, p. 23] as well as [28, p. 179] and [26, p. 52]

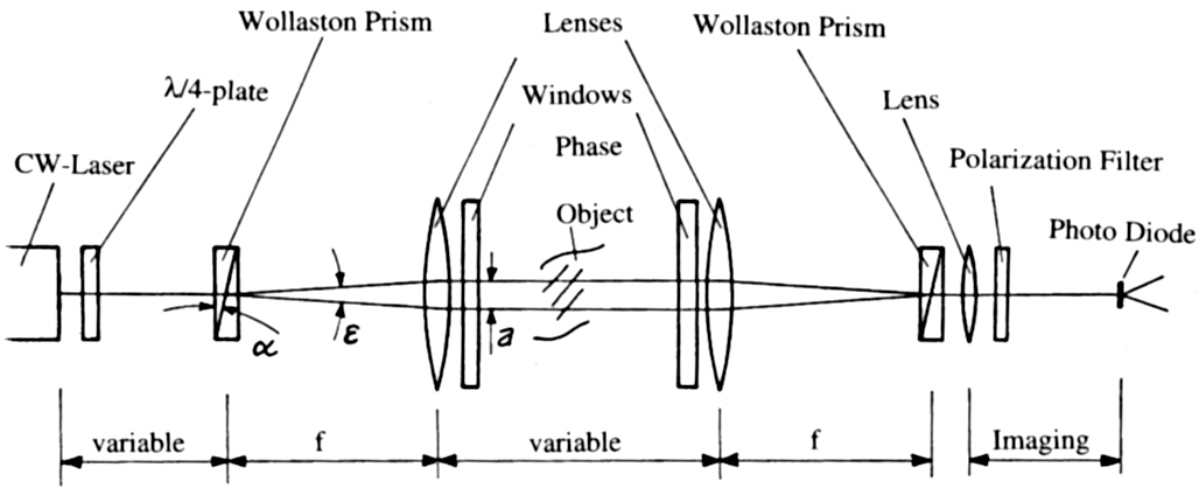



**Figure 2.2:** A schematic of a typical LDI as proposed by Smeets and George [64]. Here 'f' refers to the focal length of the field lenses next to the windows, 'Imaging' refers to a distance sufficient to recreate the size of the beam waist in the test section at the photo-diode, $\alpha$ is the Wollaston prism cut angle, and $\varepsilon$ is the divergence angle of the Wollaston prism, and $a$ is the beam separation. See footnote 2 for information on the quarter-wave ($\frac{\lambda}{4}$) plate.

beams passing through the medium, separated by $\Delta x$, this expands to [26],

$$\begin{aligned}\frac{\Delta\phi_A - \Delta\phi_B}{\Delta x} = \frac{2\pi}{\lambda\Delta x}\Bigg\{&\int_{s_{1,A}}^{s_{2,A}}\left[n\left(x+\frac{\Delta x}{2},y,z\right)-n_{\text{inf}}\right]ds_A \\ &-\int_{s_{1,B}}^{s_{2,B}}\left[n\left(x+\frac{\Delta x}{2},y,z\right)-n_{\text{inf}}\right]ds_B\Bigg\}\end{aligned} \tag{2.6}$$

By definition, as the inter-beam spacing approaches zero, this is the derivative, i.e.

$$\frac{\partial\phi_{AB}}{\partial x} = \frac{2\pi}{\lambda}\int_{s_1}^{s_2}\frac{\partial n}{\partial x}ds \tag{2.7}$$

Although $\Delta x$ must have a finite value in order to generate a signal from the interferometer, Fulghum [26] suggests this approximation is valid depending on flow properties.

Finally, this derivative of the local refractive index can be related to flow properties in the wind tunnel by means of the Gladstone-Dale relation [30], which shows the index of refraction of a fluid is directly proportional to its local density,

$$n - 1 = \sum_i K_{GD,i}\rho_i \tag{2.8a}$$

Thus,

$$\frac{\partial n}{\partial x_j} = \sum_i K_{GD,i}\frac{\partial \rho_i}{\partial x_j} \tag{2.8b}$$

where $i$ operates over the species in fluid, and $K_{GD}$ is the Gladstone-Dale constant, which is approximately $2.257 \times 10^{-4}\,\text{m}^3\,\text{kg}^{-1}$ for air. Thus, the phase shift, and therefore the intensity measured from the interferometer is related to the instantaneous spatial derivative of density in the direction of beam separation as,

$$\frac{\Delta\phi_A - \Delta\phi_B}{\Delta x} \approx \frac{\partial\phi_{AB}}{\partial x} = \frac{2\pi K_{GD}}{\lambda}\int_{s_1}^{s_2}\frac{\partial\rho}{\partial x}ds \tag{2.9}$$

Finally, combining eqs. (2.2) and (2.9) yields

$$E \approx E_0 \cos\left[\frac{2\pi^2 \Delta x K_{GD}}{\lambda^2} \int_{s_1}^{s_2} \frac{\partial \rho}{\partial x} ds\right] \tag{2.10}$$

This equation is sinusoidal, therefore a phase shift greater than $\pm\frac{\pi}{2}$, will result in the signal being aliased. Thus, it is necessary to ensure that that the sensitivity of the device is such that the measured intensity does not approach $E_0$ or $\bar{E}$. Further, it is convenient to keep the instrument in the range of $\pm\frac{\pi}{10}$ in order to use the small angle approximation, and assume the interferometer is linear (see [26, P. 48]). LDI has been used successfully by a number of researchers [55, 13].

### Wollaston Prisms

The Wollaston prism is an optical element that functions on the basis of polarization. It consists of two birefringent crystals, such a quartz ($SiO_2$), calcite, $MgF_2$, or BBO-$\alpha$, cut on a diagonal, and combined with optical cement. The Wollaston prisms used in this work are quartz (the mineral name for optical grade fused silica, $SiO_2$) and so quantities below will refer to quartz. Quantities for $MgF_2$ can be found in [26], and for calcite in [29].

Birefringence is an optical property wherein the effective index of refraction of a material is dependent on the polarization and propagation direction of incident light. In the simple case of biaxial birefringence, this is due to differential effect on electric fields in the material along one axis, generally along the growth axis of the crystal. This special axis of the anisotropic crystal is referred to as the 'optical axis', and light propagating along it will behave according to the ordinary index of refraction of the material, $n_o$, as the electric field wave's amplitude will be oriented along an axis that is not the optical axis. For any other light ray, there exist one polarization state where the electric component of the electromagnetic wave remains orthogonal to the optical axis, and the ray remains 'ordinary' and is still governed by $n_o$.

For any *other* polarization state, however, the situation differs. Any polarization state can be thought of as the superposition of two orthogonal states [10], in this case one with its polarization perpendicular to the optical axis, another ordinary ray, but one with its

polarization to the optical axis. This ray will travel at a different velocity through the crystal, corresponding to the extraordinary index of refraction, $n_e$. As long as the light enters the crystal normal to a facet, these rays will remain superimposed and the light will appear to behave as if flowing through a medium with an index of refraction is between $n_o$ and $n_e$.

The index of refraction varies with wavelength according to the Sellmeier equation [43, 29], eq. (2.11a),

$$n_{o,e}^2(\lambda) = 1 + \sum_i \frac{B_i \lambda^2}{\lambda^2 - C_i} \tag{2.11a}$$

$$n_{o,e}^2(\lambda) = A + \frac{B_2 \lambda^2}{\lambda^2 - C_2} + \frac{B_3 \lambda^2}{\lambda^2 - C_3} \tag{2.11b}$$

where $\lambda$ is the vacuum wavelength and $A$, $B$, and $C$ are determined experimentally. A three term equation is typically used, but at long wavelengths the first term may be approximated eq. (2.11b) as a constant, $A$. Table 2.1 provides the results from several authors. From this $n_o$ and $n_e$ can be calculated. At 632.8 nm, the wavelength of the HeNe lasers used in most LDIs, these result in $n_o = 1.5427$ and $n_e = 1.5517$, giving a birefringence of $\Delta n = n_e - n_o = 0.00906$. A positive birefringence means the extraordinary ray travels more slowly, and so, in quartz, is colloquially referred to as the 'slow' ray, vs the 'fast' ordinary ray.

The Wollaston prism uses this effect to split a polarized beam in half. When electromagnetic radiation changes from a medium with one angle of refraction to another at an angle, it will deflect proportionally to the ratio of the indices of refraction. This is governed by Snell's law [10, p. 39],

$$\frac{\sin\theta_1}{\sin\theta_2} = \frac{n_2}{n_1} \tag{2.12}$$

where $\theta$ is the angle between the light ray and the normal of the medium interface. Assuming the laser beam enters the Wollaston prism at a 0° angle of incidence, the ordinary and extraordinary beams will remain superimposed. Further assuming that the laser is linearly polarized[2] at 45° to the optical axis of the first crystal of the Wollaston prism, the ordinary and extraordinary beams will have equal amplitude.

[2]This work relies on linear polarization. Although Smeets and George [64] use circular polarization, this is not the dominant design for FLDI [26, 13]. This may be due to the fact that the $\frac{1}{4}$ Wave-plates are more expensive than linear polarizers, and must be wavelength specific.

**Table 2.1:** Sellmeier equation coefficients for quartz ($SiO_2$).

| Malitson [43] | $B_1$ | $\sqrt{C_1}$ | $B_2$ | $\sqrt{C_2}$ | $B_3$ | $\sqrt{C_3}$ |
|---|---|---|---|---|---|---|
| $n_o$ | 0.696 166 | 0.068 404 | 0.407 943 | 0.116 241 | 0.897 479 | 9.896 161 |
| Ghosh [29] | $A$ | | $B_2$ | $C_2 \times 10^{-4}$ | $B_3$ | $C_3$ |
| $n_o$ | 1.286 041 | | 1.070 441 | 1.005 851 | 1.102 022 | 100 |
| $n_e$ | 1.288 518 | | 1.095 099 | 1.210 186 | 1.156 625 | 100 |

When these two superimposed beams encounter the diagonal face between the two crystals, they diverge. Because the crystals of the prisms have their optical axes mounted orthogonally to each-other and to the direction of laser propagation, across the face the ordinary ray will become the extraordinary ray and likewise for the extraordinary ray. Thus, they see an equal and opposite change in refractive index, and refract at equal angles away from each-other. As quarts has a small birefringence, this angle will be very small (the half-angle between the two rays for a quartz Wollaston Prism cut at 60° is 38′. However, when the rays leave the second crystal and enter air with $n = 1.000\,293$, their incoming angles will be opposite, the difference in the ratio of refractive indexes is negligible and those ratios are comparatively large, i.e.

$$\frac{n_o}{n} \approx \frac{n_e}{n} \gg \frac{n_o}{n_e}$$

so they will refract away from each-other a significant amount. The diversion angle $\varepsilon$ follows as [64],

$$\varepsilon = 2 \tan \alpha |n_e - n_o| \tag{2.13}$$

where $\alpha$ is the angle at which the crystals are cut. Further, the separation in the beams of an LDI, $a$ can be found[64],

$$a = 2f \tan \alpha |n_e - n_o| \tag{2.14}$$

where $f$ is the focal length of the LDI field lenses. Should the beams not impinge on the Wollaston prism in the center, they will see a different amount of travel distance in the two crystals. This will lead to phase shift, as a peak in the waveform of the 'fast' ray will exit the crystal before a peak in the 'slow' beam that entered the quartz crystal at the same time. This phenomenon allows the two phase difference to be continuously adjusted between two beams. Figure 2.3 depicts such a Wollaston Prism.

In some cases, the expense of two or more finely matched Wollaston prisms may be a barrier of entry to the use of FLDI. In such cases, birefringent plastics may provide a solution [56]. Certain plastics exhibit birefringence when placed under stress. Sanderson [56] presents prism design based on a screw mechanism, creating a constant stress in a plastic bar. This effectively creates an adjustable Wollaston prism, referred to as a Sanderson prism. Two

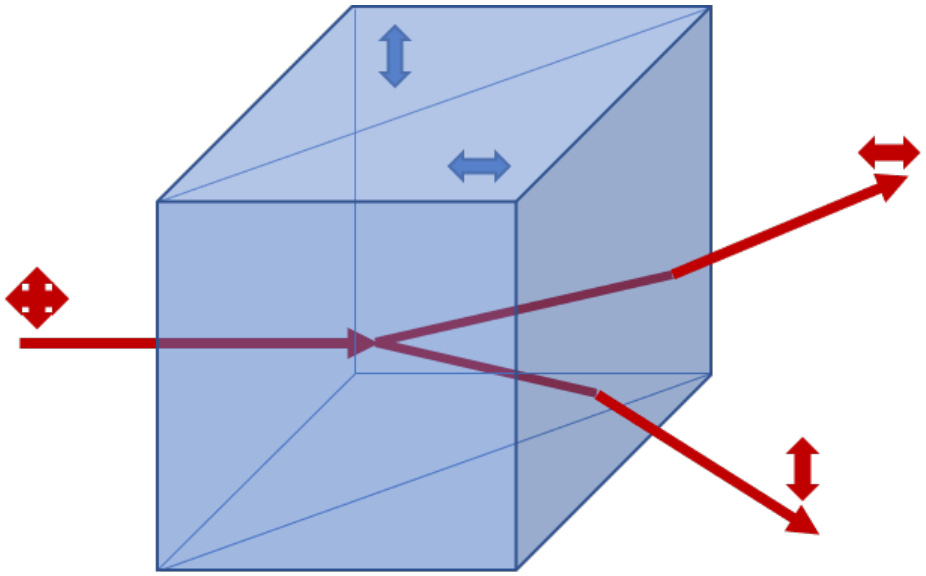


**Figure 2.3:** A schematic of a typical two crystal birefringent Wollaston prism. Angles exaggerated for clarity.

such implements can be tuned to match for use in an FLDI, at minimal cost[3]. The author of this work attempted to recreate such Sanderson prisms while the Wollaston prisms used herein were on order, and while the birefringent behavior was observed, the required splitting angles could not be achieved. Note that the critical work by Fulghum [26] used Sanderson prisms.

### 2.2.2 Focused Laser Differential Interferometry

LDI does have limitations when it comes to high-speed wind tunnel testing. Namely, the instrument must pass though, and therefore measure, the large turbulent boundary-layers along the walls and windows of the wind-tunnel. Smeets and George [64] suggests a solution to this, selective focusing of the LDI in the center of the test section, in the technique that has come to be known as FLDI.

In an FLDI, the laser is expanded with a negative lens or a telescope following the laser source. It is then re-focused on the test object using the same LDI field lenses. By passing thorough the wall boundary layer with an increased diameter, the effect on the signal is averaged over many large-scale eddies, thereby spatially filtering out the signal from the wall boundary layers. Figure 2.4 provides a schematic of an FLDI.

The concept was reintroduced by Parziale et al. [50, 51] in 2012, who used it to detect instabilities in a boundary layer. Subsequently, significant work was completed by Fulghum [26] to describe and characterize the system, using transfer functions to model the system's behavior. The work then goes on to compare the turbulent intensity calculated from HWA (velocity TI%) and that from FLDI (density TI%) showing that they are comparable metrics. This result is shown in fig. 2.5.

FLDI has been used in a number of studies Ceruzzi and Cadou [13] compared the effectiveness of LDI and FLDI and show that the noise rejection of the wall boundary layer due to the focusing effect is effective at high and medium frequency, but that low frequencies remain. Benitez et al. [6] examined an axisymmetric separation Bubble at Mach 6 and found spectral indication of the second mode instability . Benitez et al. [7] also looked at the effect of curved windows on the FLDI.

[3]The required parts could probably be scavenged from the average university engineering building

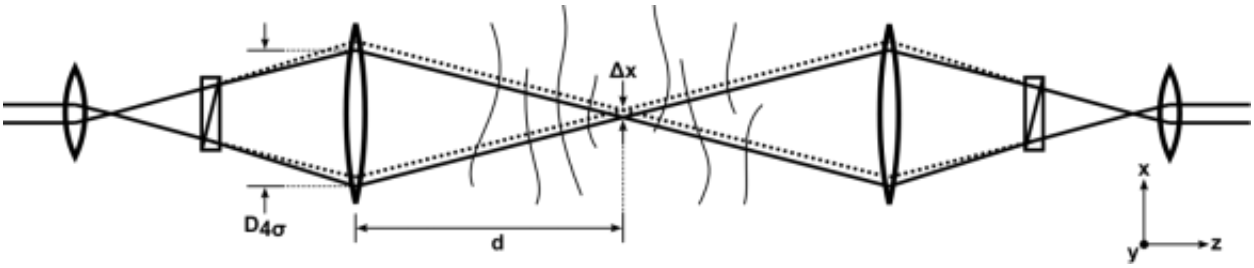



**Figure 2.4:** A schematic of an FLDI [26]. Here $D_{4\sigma}$ is the diameter of the laser at its largest and 'd' is the effective focal length of the combination of the expanding lens and field lens.

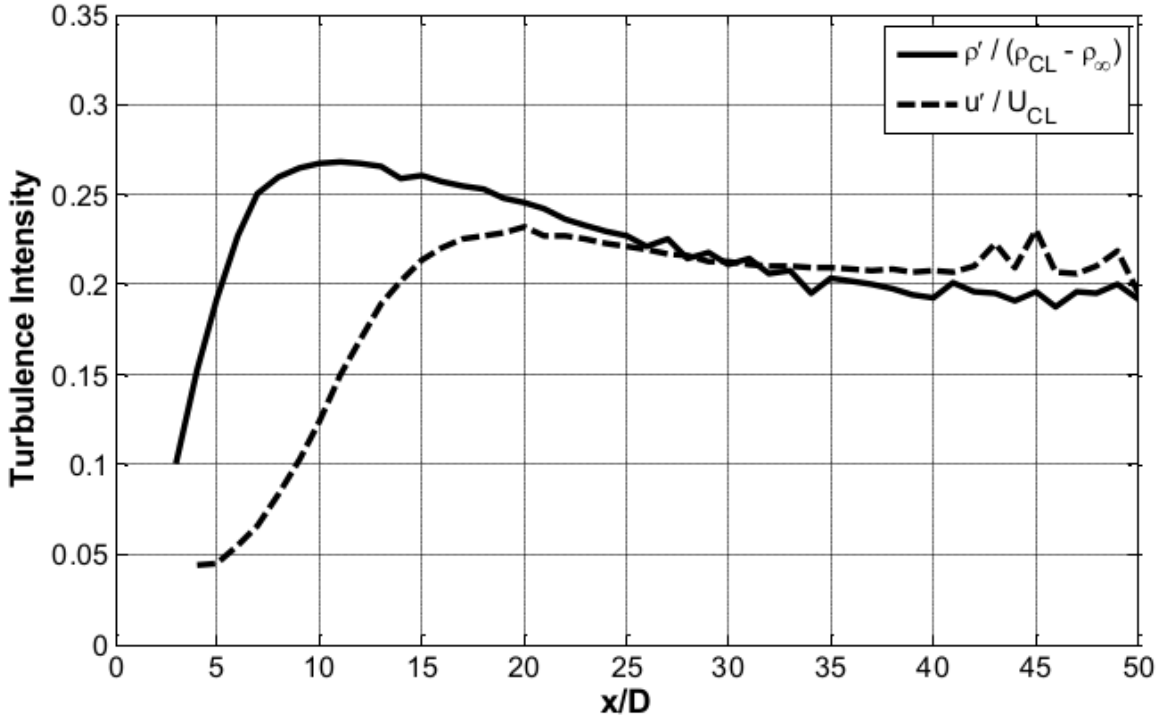



**Figure 2.5:** Comparison of Turbulent Intensity calculations using HWA and FLDI. From [26].

### 2.2.3 2-Point Focused Laser Differential Interferometry

2-point FLDI is a technique that uses an additional wide-angle Wollaston prism, a polarizer, and an additional photo-diode to split the system into two distinct FLDIs and measure them independently. This device is then able to measure the local velocity as well as the local density derivative due to Taylor's hypothesis, which states that that over as sufficiently short distance, $\Delta X$, turbulence does not change significantly in character, but simply travels with the bulk fluid. Thus, function of time and functions of space are directly related by the convective velocity. Therefore, as a turbulent spot passes over each beam, it will create a similar signal, and by calculating the time delay between the signals the velocity can be determined. It should be noted that, due to the fact that the FLDI signal is a function of the variation in density of distinct turbulent eddies, the FLDI does not measure the bulk fluid, but turbulent phenomena in a particular size range. In general, these eddies convect at about 85 % of the bulk flow due to induced drag [47].

Although the splitting of the laser into multiple FLDIs using prisms was suggested by Smeets and George [64] and two independent FLDIs were used by Parziale [49] the use of the common path 2-point interferometer used in this work was first shown by Ceruzzi and Cadou [14]. They then demonstrates its use to measure velocity profiles in a Mach 2.6 turbulent boundary layer[15].

Recent developments by Bathel et al. [4] use a Nomarski prism to decrease the cost of wide angle Wollaston Prism. Wollaston and Nomarski prisms differ in the apparent origin of the diversion of the rays, leading to a longer FLDI setup when using a Nomarski prism. Nomarski prisms are commonly used in microscopy and therefore may be available at a lower cost [23].

A 4 point FLDI that detects the second Mode instability at Mach 5.8 has recently been demonstrated [32]. Such multi-FLDI setups are likely the direction of future work (see section 5.2) as they allow for more a more complete picture of flow physics are reduced cost (tunnel operation time).

### 2.2.4 High-speed Schlieren

Schlieren and shadowgraph are longstanding aerospace diagnostic techniques. Settles [62] covered the state of the art in 2001, though high speed camera technology has advanced significantly since then. Schlieren is based on the passage of collimated light though the test section. Differences in density cause differences in refracting index, following the Gladstone-Dale relation as stated above in eq. (2.8a), and cause the light to refract slightly out of collimation. This light is then cut off with a razor or other light pick-off, and the resulting ray of light imaged. This leads to a full-scale image of the resulting flow field with light and dark regions that are a function of local density. High-speed, custom LED drivers and cameras allow for image acquisition up to 400 kHz

Recent work has sought to use high speed schlieren to quantitatively measure the flow, though it is historically it has been regarded as only a qualitative technique. Groups such as Laurence et al. [39], have demonstrated calculation of the spectrum of a transitional boundary layer and detect the second mode instability.

# Chapter 3

# Experimental Methodology

## 3.1 Facility

### 3.1.1 UTSI TALon Mach 4 Tunnel

The facility used throughout these experiments is the TALon Mach 4 low-enthalpy Ludwieg tube at UTSI. The test section has a constant cross-section of 610 mm × 610 mm (24 in × 24 in) and is 1.83 m (72 in) long, divided into three sections. All experiments took place in the first 610 mm (24 in) segment of the test section. The driver tube is 610 mm (24 in) in diameter and 32 m (105 ft) long. The facility is operational with stagnation pressures from atmospheric to 1135 kPa (150 psia). The Ludwieg tube is configured with a single diaphragm section directly upstream of a large 914 mm (36 in) diameter connection pipe next to a 508 mm (20 in) long expansion joint before the two-dimensional planar nozzle and test section. Variation in stagnation pressure, and therefore Reynolds number, is achieved by altering the number and thickness of Mylar® plastic diaphragms. The Ludwieg tube is commonly run at 3 stagnation conditions, using one, two, or three clear Mylar® diaphragms each with a 0.254 mm (0.01 in thickness. These correspond to stagnation pressures of approximately 124 kPa, 248 kPa and 462 kPa and Reynolds Numbers of $2.28 \times 10^6\,\mathrm{m}^{-1}$, $4.87 \times 10^6\,\mathrm{m}^{-1}$ and $8.49 \times 10^6\,\mathrm{m}^{-1}$, respectively. The diaphragms are burst by bringing the nozzle, test section, and vacuum chamber side of the diaphragm down to near vacuum, (on the order of 0.5 kPa) and pressurizing the upstream driver tube (partially evacuated prior to the run to ensure

dry air). Although there is variability in the stagnation conditions between runs due to uncertainty in the diaphragm rupture process, the stagnation conditions are recorded in real time during the run. The stagnation temperature, as measured with a thermocouple inserted in the flow is approximately 305 K. Steady flow operational time is approximately 130 mm. Recorded pressures from a typical three diaphragm run are shown in fig. 3.1. The tunnel achieves $M_a = 4.0$ throughout a large test core and has a flow velocity of about 677 m s$^{-1}$. Optical access for the experiments is provided by 36.0 cm × 43.7 cm (14.2 in × 17.2 in) BK-7 glass windows in the test section sidewalls. Figure 3.2a has a computer render and fig. 3.2b has a picture of the TALon Mach 4 facility. It is important to note that the bottom of the test section is 2 m above the floor of the lab, to facilitate personnel and equipment access, so all diagnostics are mounted on large stands (see fig. 3.3).

## 3.2 Models

Two aluminum models were constructed for use in the Mach 4 Ludwieg tube, a Hollow Cylinder Flare (HCF) and a Hollow Cylinder (HC).

### 3.2.1 Hollow Cylinder Flare

An aluminum Hollow Cylinder Flare (HCF) model at a moderate size was constructed for this work in order to initially characterize the flow-field of an axisymmetric SBLI using FLDI. The Hollow Cylinder Flare model is a 12 cm (4.75 in) cylinder with a 5.1 cm (2 in) outer diameter, followed by a 24° flare, with a 12.7 cm (5 in) maximum diameter. The model is hollow with a 10° internal leading edge and a 4.44 cm (1.75 in) inner diameter throughout.

The boundary layer is laminar with $\delta \approx 2$ mm near the $\lambda$-shock of the SBLI, as determined from schlieren images (section 4.2.1). The shock wave caused by the flare interacts with the boundary layer while it is still laminar, leading to a steady SBLI. The HCF model can be tripped such that the boundary layer is turbulent upon reaching the shock-wave using 4×1 cm strips of 120 grit adhesive sand paper, spaced 1 cm apart, starting 2.54 cm (1 in) from the leading edge. Several configurations of trips were tested, including a single 2.54 cm (1 in) strip and 3 × 1 cm strips configured as above. More testing would be required to determine if the

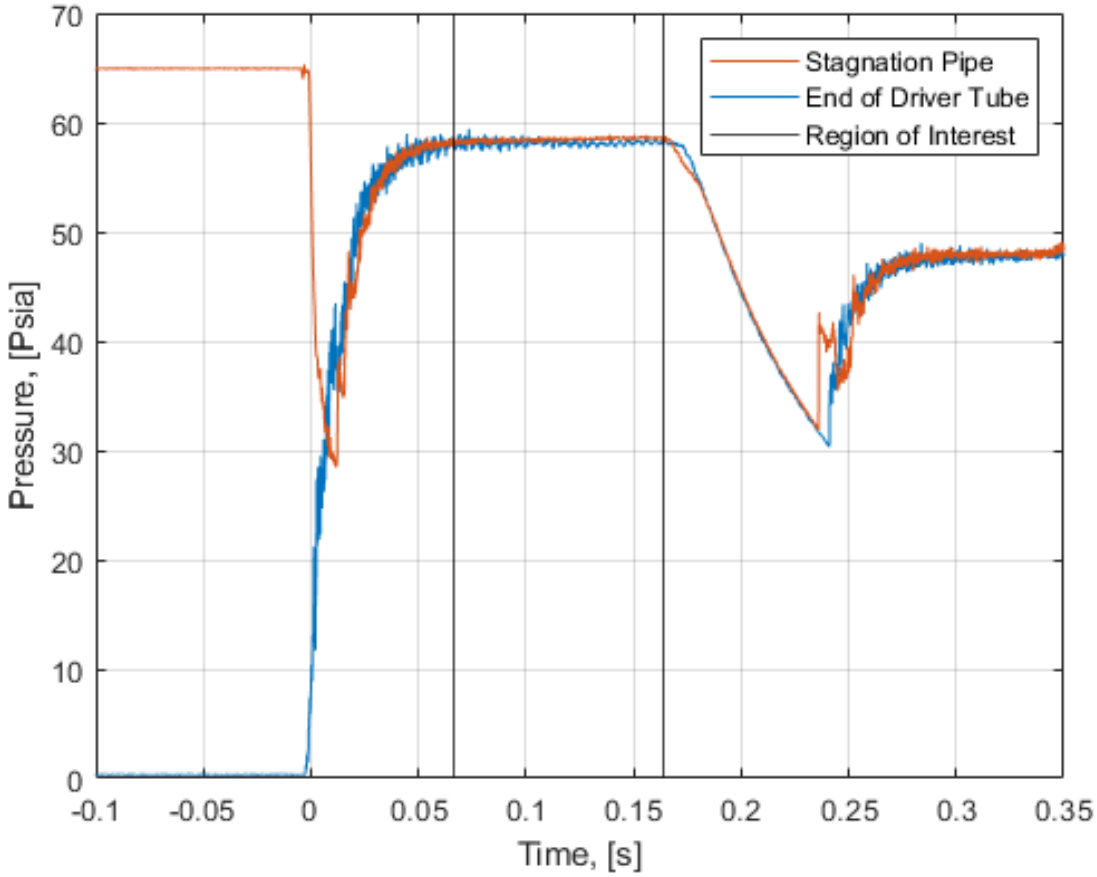
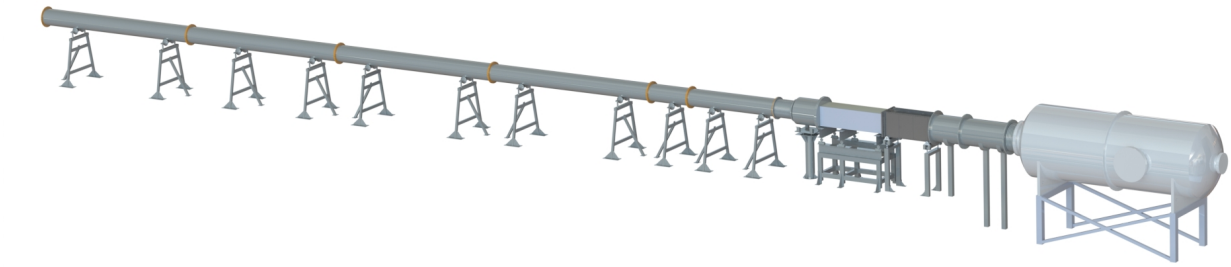



**Figure 3.1:** Recorded pressures in the TALon Mach 4 facility from a typical 3 diaphragm run. Measurements reported here are from the end of driver tube and from the large diameter stagnation pipe, upstream of the test section. The start and end of the quasi-steady-state region of interest used for FLDI and schlieren analysis is marked in black.



**(a)** 3-D rendering of the Mach 4 Ludwig Tube at TALon. No windows are installed in the test section, colored in black, in this render. Note that the large vacuum tank sits outside of the lab.



**(b)** Photograph of TALon and the Mach 4 Ludwig Tube. Note that acrylic windows, rather than the current BK-7 windows are installed in this photograph. A pair of TALon optical stands are visible, center, supporting a 6 in schlieren setup. Note that this schlieren setup is configured with its 'send' and 'receive' sides opposite to the work in this manuscript.

**Figure 3.2:** The Mach 4 Ludwig Tube at TALon.

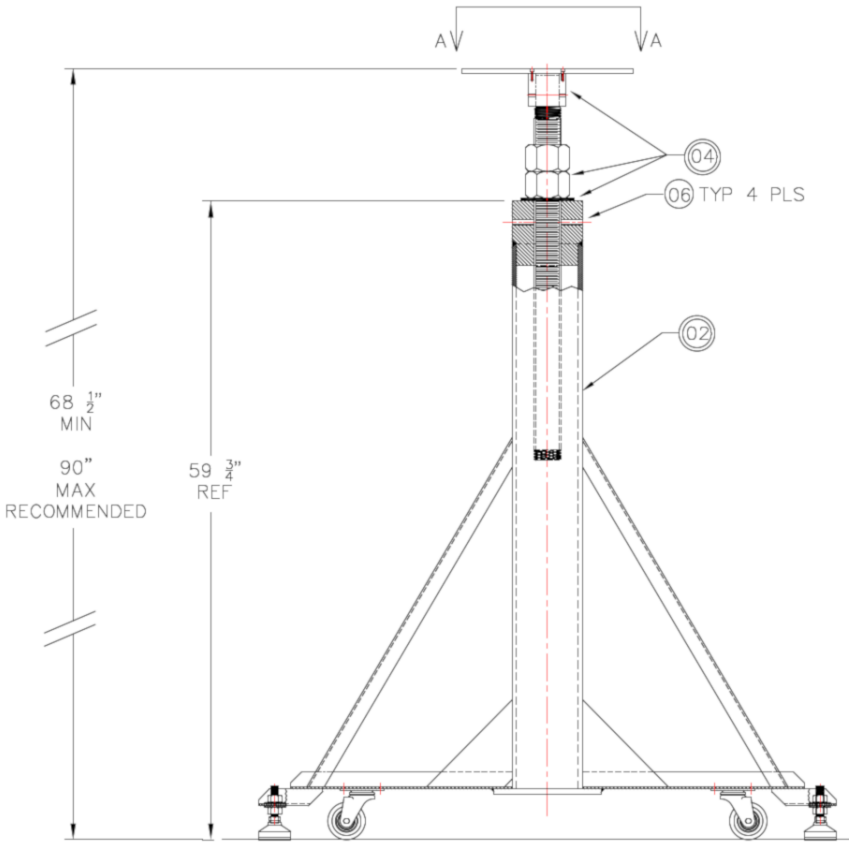



**Figure 3.3:** Diagram of the TALon facility optical stands

tripping action is caused by the roughness of the sandpaper itself, as intended, or the repeated small forward-facing step caused by the strips. See fig. 3.5f for a measure of the roughness of the 120 grit sandpaper. Figure 3.4b depicts the geometry of the Hollow Cylinder Flare. The laminar SBLI generates a large separation and recirculation region; However, as the model does not completely pass the Korkegi Criterion [37, 38], the tripped turbulent SBLI does not generate a significant separation region. After this was discovered with schlieren, the tripped condition was not investigated with FLDI. In order to test transitional and turbulent SBLI behavior, a new model has been developed, but is not documented here.

### Surface Roughness

A coat of unsteady pressure sensitive paint (uPSP)(see [31] for a review) was applied along the whole length of the top of the model during a previous experiment, in a 60° arc, and this was allowed to remain in order to maintain consistent surface conditions. The surface roughness was measured using the Mitutoyo Surftest SJ-210 Portable Surface Roughness Tester[44]. All measurements were 4 mm long in the stream-wise direction, using the 'profile' (low-pass filtered only) settings, except for the calibration test, which used the 'roughness' (low-pass and high-pass filtered) settings for comparison to the manufacturer's data. Figure 3.5 shows the recorded profiles of a variety of surfaces in this experiment, and reports the arithmetic mean deviation

$$P_a = \frac{1}{L}\int_0^L y(x)dx \tag{3.1}$$

the root mean square

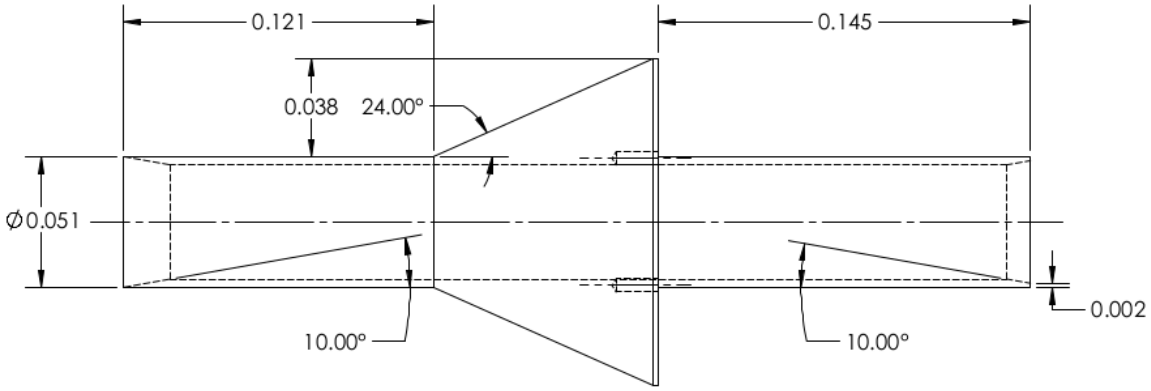
$$P_q = \sqrt{\frac{1}{L}\int_0^L [y(x)]^2 dx} \tag{3.2}$$

and the total distance peak to trough, $P_z$, of the measurements. The calibration test was passed with errors of $P_a \pm 0.02\,\mu$m, and $P_z \pm 0.18\,\mu$m. Other roughness tests were not repeated sufficiently to establish error-bounds.

[1]Enamel paint, typically used to eliminate reflection from the model during oil-flow experiments, was not used in this experiment but is given for comparison to uPSP.

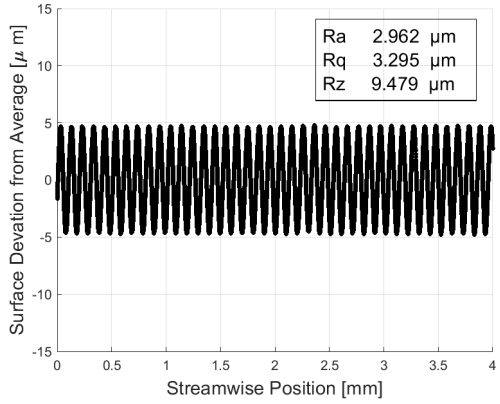


**(a)** Photograph of the Hollow Cylinder Flare.

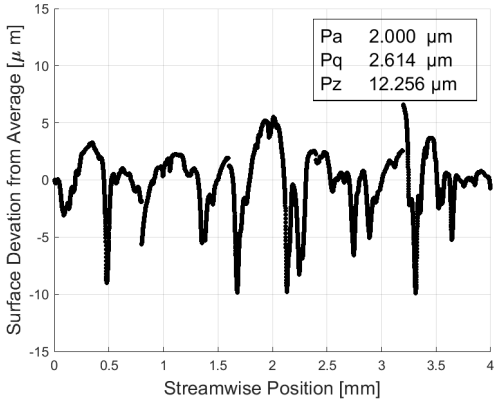



**(b)** 2-D CAD schematic of the Hollow Cylinder Flare. Distance in (m)

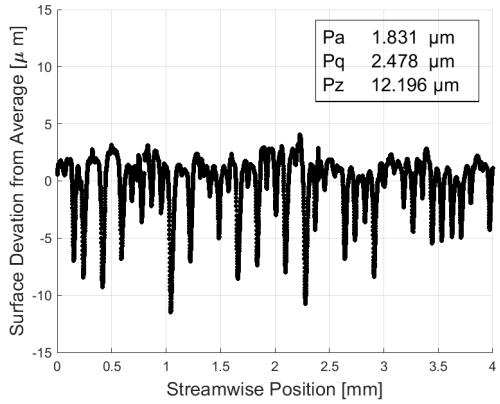
**Figure 3.4:** Photograph and 2-D CAD schematic of the UTSI Hollow Cylinder Flare model.



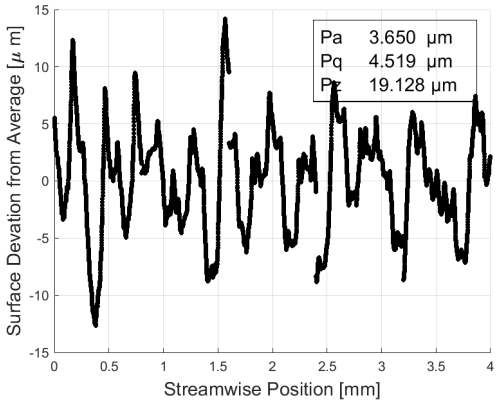

**(a)** Mitutoyo surftest SJ-210 calibration.



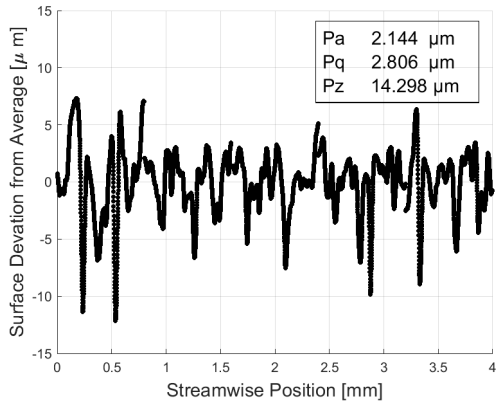

**(b)** UPSP on HCF.



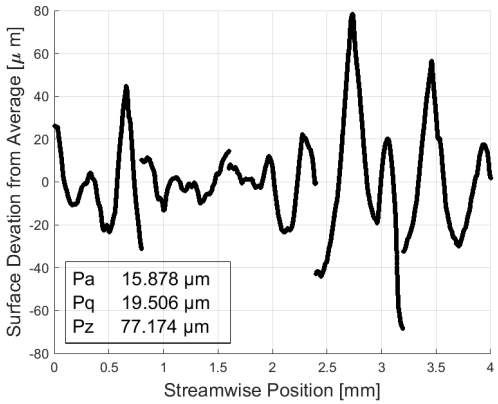

**(c)** Aluminum of Cylinder of HCF.




**(d)** Un-sanded inside of HCF.




**(e)** Enamel paint on HCF[1].




**(f)** 120-grit sandpaper. Note change of axes.

**Figure 3.5:** Roughness measured on various parts of the HCF model. $P_a$ is the arithmetical mean deviation of the profile, $P_a = \frac{1}{L}\int_0^L y(x)dx$, $P_q$ is the root mean square of the profile, $P_q = \sqrt{\frac{1}{L}\int_0^L [y(x)]^2 dx}$, and $P_z$ is total distance peak to trough.

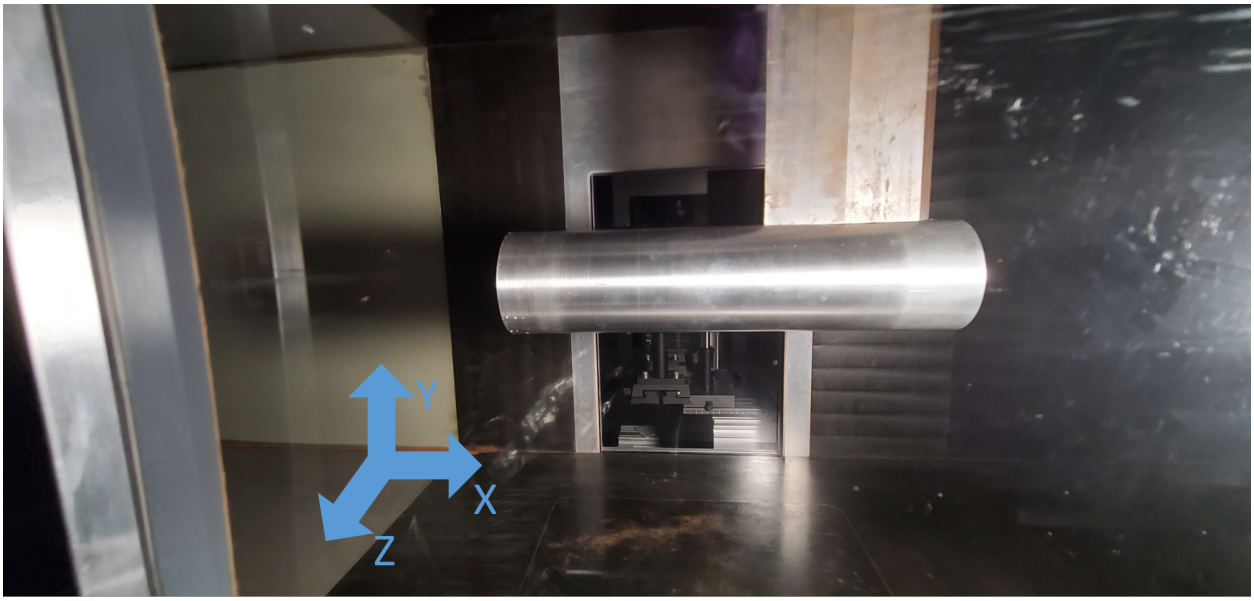
### 3.2.2 Hollow Cylinder

In order to test the FLDI on a simpler model and further understanding of boundary layer growth on a model in the TALon Mach 4 facility to support the design of future experiments, a Hollow Cylinder (HC) model was constructed. Also made of aluminum, the Hollow Cylinder model is a 8.9 cm 93.5 in) diameter by 37.0 cm (14.55 in) long cylinder with a 10° internal leading edge and a 7.6 cm (3 in) inner diameter throughout. The Hollow Cylinder has a polished surface. At the downstream end of the model, there are a number of tapped and through holes to mount the shock generators and access fasteners. A shock induced by the supersonic jet exiting these holes is apparent on schlieren. This region is avoided in the present work, but some influence traveling upstream in the subsonic region of the boundary layer may remain. In the region just before these holes, the boundary layer has a hight of $\delta = 2.5$ mm.

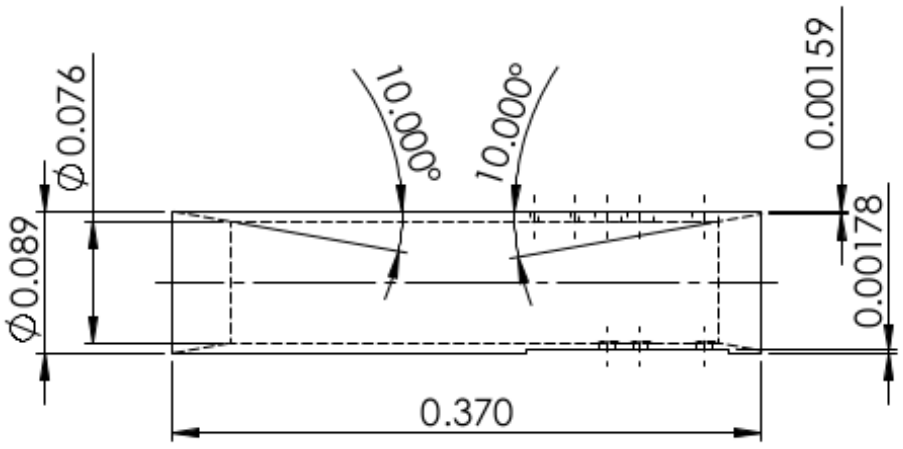
Figure fig. 3.6b depicts the geometry of the Hollow Cylinder, and fig. 3.6a shows the HC model as installed in the TALon Mach 4 facility. A consequence of the larger diameter of the HC as compared to the HCF and the aluminum construction of the model was that the model was susceptible to damage from severed diaphragm material carried downstream during the run. This required refinishing of the model's leading edge and resulted in a decrease in the model length. To account for this and not damage the model edge, all measurements are made from the back of the model and calculated as a distance from the front of the model, based on its length as measured after refinishing.

## 3.3 Diagnostics

These experiments employ two optical diagnostics that partially share an optical path, 2-point FLDI and integrated schlieren, as well as the facilities full-scale schlieren system. As noted in section 1.3.1, optical diagnostics are primarily used in order to prevent the intrusive effects of in-situ diagnostics, which may effect the fluid phenomena being investigated non-negligibly. The TALon Mach 4 Ludwieg tube provides excellent optical access for these diagnostics, however its large scale (60% linear scale of AEDC VKF Tunnel A) requires significant optomechanical fixturing, such as the TALon facility optics stands, diagrammed




**(a)** Photograph of the Hollow Cylinder model mounted in the first test section of the TALon Mach 4 Ludwieg tube, with axes labeled.




**(b)** 2-D CAD schematic of the Hollow Cylinder. Distances in (m).

**Figure 3.6:** Photograph and 2-D CAD schematic of the UTSI Hollow Cylinder model.

in fig. 3.3, as well as the large apparatus used to mount the FLDI and Schlieren systems to the tunnel, see fig. 3.8 for photographs.

Herein, a consistent right-hand coordinate system where $+x$ is downstream in the wind-tunnel, $+y$ is up from the floor of the wind-tunnel, and $+z$ is towards the observer standing with the driver tube on the left and the vacuum tank on the right. The origin was placed at the front of the model, on the centerline. Figure 3.6a shows this coordinate system.

### 3.3.1 2-Point Focused Laser Differential Interferometry

#### UTSI 2-Point FLDI Apparatus

As described in section 2.2.2, an FLDI consists of a laser source, a method of expanding the laser beam, a way to focus the laser into the test section, generally a pair of field lenses, prisms to split and recombine the laser, and a detector to record the phase difference [26]. A 2-point FLDI implementation adds an extra wide-angle Wollaston prism and polarizer. Figure 3.7 details the current iteration of the interferometer at UTSI, with photographs of the sending, fig. 3.8a, and receiving, fig. 3.8b, sides. Table 3.1 provides information on all optical components used, to facilitate repeatability; see section 5.2.2 for information on optomechanics and recommendations on future systems.

A Thorlabs 5 mW HeNe laser has been used in all experiments discussed in this work [67]. These lasers have excellent beam quality and a strong polarization ratio, reducing the need for laser filtering, and a small beam diameter, which directly effects the sensitivity of the FLDI [26, p. 25]. A $f = -9\,\text{mm}$ lens is used to expand the beam, and a pair of $\varnothing = 75\,\text{mm}, f = 200\,\text{mm}$ field lenses focus the beam in the test section. A $f = 75\,\text{mm}$ lens refocuses the laser on a pair of Si photo-detectors [75]. See appendix A for information on the setup and alignment process of a 2-point FLDI.

#### Longitudinal Sensitivity Study

Initially, it was necessary to confirm that the FLDI was rejecting signals away from the focus. With the FLDI setup in the Ludwieg tube, an experiment was conducted, similar to that conducted by Ceruzzi and Cadou [13]. A subsonic jet of air from a $\varnothing_{internal} =$

**Table 3.1:** List of FLDI Components

| Optical Component | Part | Manufacturer | URL |
|---|---|---|---|
| Laser Source | HeNe Laser, 632.8 nm, 5 mW, Polarized, HNL050LB | Thorlabs | [67] |
| Expanding Lens | N-SF11 Bi-Concave Lens, ⌀=9 mm, f=−9 mm, Uncoated, LD2568 | Thorlabs | [70] |
| 1.5° Wollaston Prism | Quartz Wollaston Prism, 30 × 30 mm, 1.5° beam divergence at 632.8 nm, AR coated for 632.8 nm both sides | United Crystals, Custom Order | [20] |
| Large Polarizer | ⌀=2 in Linear Polarizer with N-BK7 Windows, 400-700 nm, LPVISE200-A | Thorlabs | [72] |
| 5′ Wollaston Prisms | Custom order, Quartz Wollaston Prism, 50 × 50 mm, 5′ beam divergence at 632.8 nm, AR coated for 632.8 nm both sides | United Crystals, Custom Order | [20] |
| Dichroic Mirrors | ⌀=2 in Longpass Dichroic Mirror, 567 nm | Thorlabs | [66] |
| Field Lenses | N-BK7 Plano-Convex Lens, ⌀=75 mm, f=200 mm, Uncoated LA1353 | Thorlabs | [68] |
| Small Polarizer | ⌀=1 in Linear Polarizer with N-BK7 Windows, 400-700 nm, LPVISE100-A | Thorlabs | [71] |
| Focusing Lens | N-BK7 Plano-Convex Lens, ⌀=1 in, f=−50 mm, Uncoated, LC1715 | Thorlabs | [69] |
| Photo-detectors | Si Switchable Gain Detector PDA36A2 | Thorlabs | [75] |

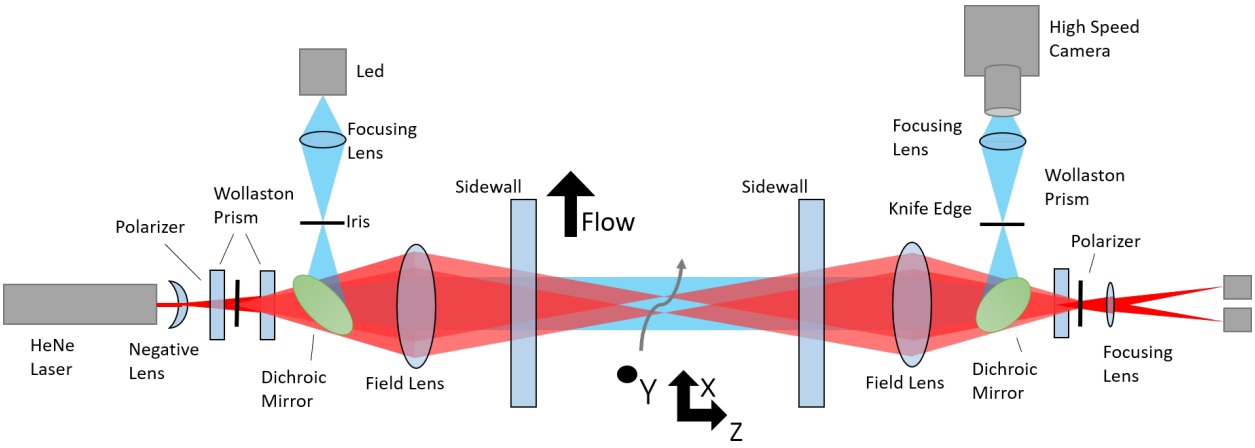
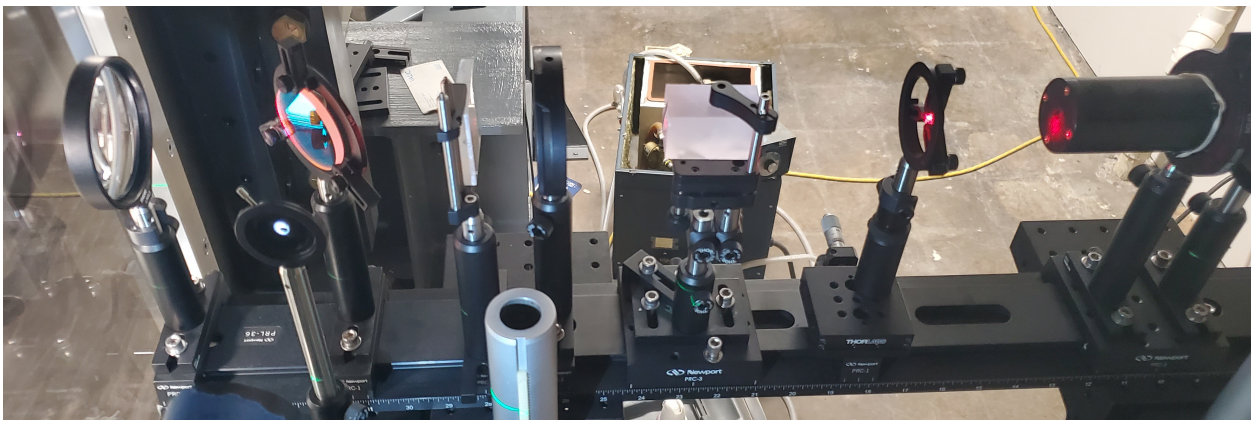
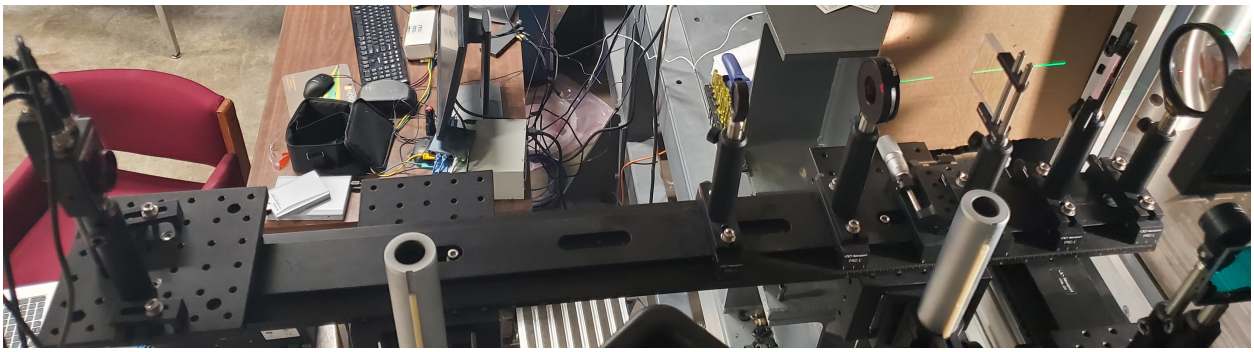



**Figure 3.7:** A schematic of the UTSI 2-point FLDI system, with integrated schlieren.



**(a)** 'Send' side of UTSI FLDI as installed



**(b)** 'Receive' side of UTSI FLDI as installed

**Figure 3.8:** Photographs of UTSI FLDI as installed in the TALon Mach 4 Ludwieg Tube.

3.175 mm($\frac{1}{8}$in) section of tubing was stepped in increments between the windows of the wind tunnel in the $z$ axis. The increments were generally 25.4 mm (1 in), but were 12.7 mm (0.5 in) around the focal region of the FLDI. Plenum pressure ahead of the length of tubing was 295 kPa $\pm$ 21 kPa (43 psia $\pm$ 3 psia). Results are shown in fig. 3.9 and they demonstrate that high and medium frequencies are spatially filtered by the focusing of the FLDI, but some low frequencies remain. The low frequencies are not a concern for the later experiments as they are far below the frequencies of interest for viscus structures in the flow. A Strouhal analysis predicts frequencies above 300 kHz based on a boundary layer height of 2 mm, for the Hollow Cylinder Flare, and the tunnel velocity of 677 m s$^{-1}$.

### Data Acquisition

After the Ludwig tube was readied for operations, the position of the FLDI was measured relative to the coordinate system defined in section 3.3 with an engineering scale with $\frac{1}{64}$in graduations. Then the spacing of the 4 beams was measured with the Newport LBP2-VIS2 beam profiler [45]. Results are imported to `MATLAB` to find geometric centers of the beam intensities and calculate distances $\Delta x_a$, $\Delta x_b$, and $\Delta X$. Typical values for these distances are $\Delta x_{a,b} = 0.28$ mm and $\Delta X = 3.4$ mm An example measurement from the beam profiler is given in fig. 3.10. Measurements were alternated between before and after the wind tunnel run in order to reduce the number of the times the tunnel was opened, thereby decreasing total test time.

The tunnel was then brought to vacuum, at which point the maximum and minimum brightness, $E_0$ and $\bar{E}$ were recorded for each beam, and the 2-point FLDI was set to the middle of the interference curve. Depending on the orientation of the 'send' side polarizer, the independent FLDIs either respond alike or opposite to each-other when a signal passes. The HCF runs were in phase and the HC runs were 180° out of phase, but this difference can be handled during data processing. The tunnel was partially pressurized, and then the vacuum machinery was turned off and sealed off from the system, so that a noise tare could be taken. During the noise tare, the compressor remains running, as it will run continuously during a Ludwieg tube test. The driver tube was pressurized until the diaphragms burst, running the tunnel. The pressure rise in the large connection pipe is observed by the tunnel

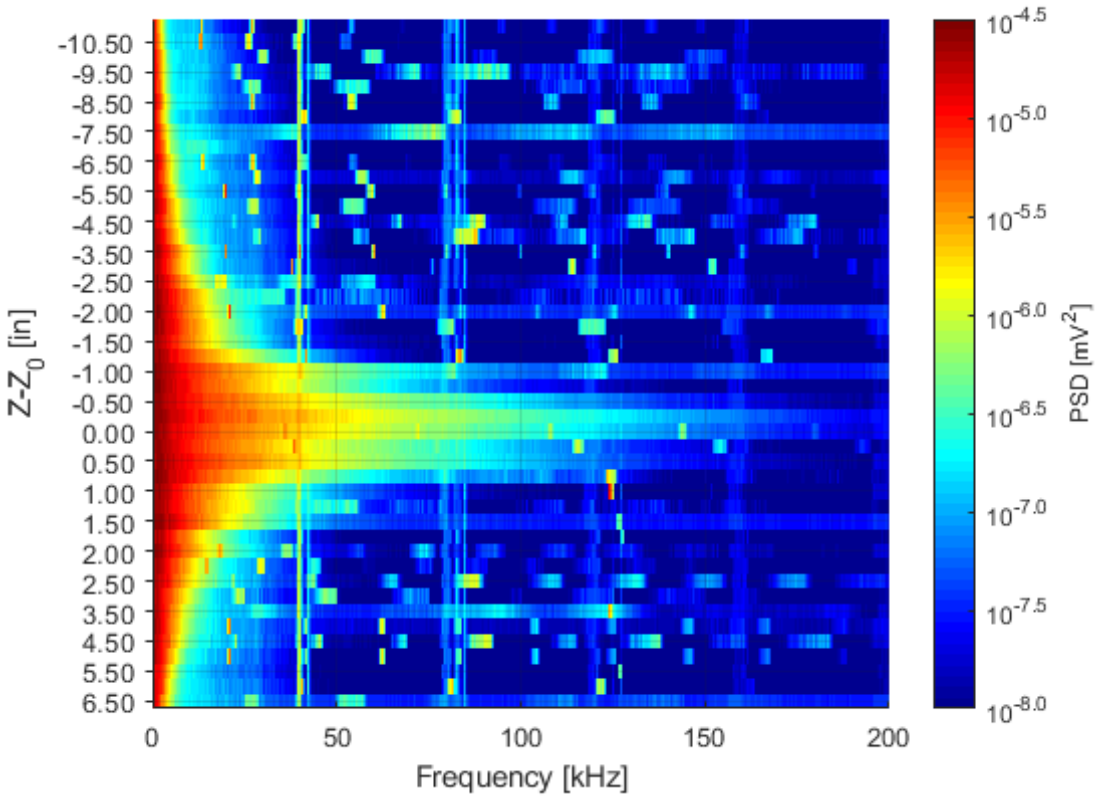



**Figure 3.9:** Results from sensitivity study: medium and high frequency noise at the tunnel wall is rejected by the focusing of the 2-point FLDI.

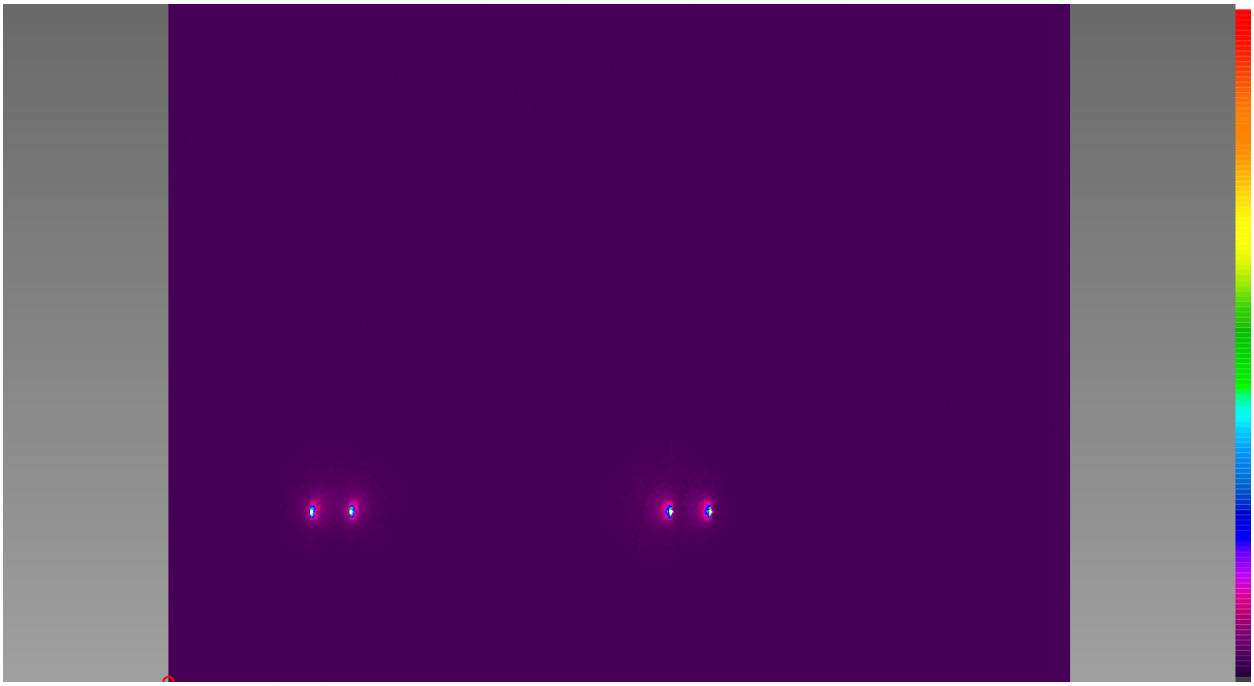


**Figure 3.10:** Measurement of beam separation with Newport LBP2-VIS2 beam profiler [45]. Results are imported to `MATLAB` to find geometric centers of the intensities and calculate system beam separation.

control system, sending a trigger TTL pulse to the schlieren camera and a Teledyne LeCroy WaveSurfer 10 recording the signal from the photo-diodes. The WaveSurfer 10 records a 1 s 8-bit signal at 20 MHz of both diodes synchronously.

The data is then passed to `MATLAB` with a custom driver for the WaveSurfer 10, where the signal, spectra, and calculated velocity are checked for anomalies. A second noise tare is taken after the run and then the wind tunnel is returned to atmospheric pressure.

#### Analysis of FLDI

To analyze the 2-point FLDI signal, first the tunnel pressure signal is imported to `MATLAB` and a window of quasi-steady flow is isolated. the FLDI signals were cropped to this region and the spectra were acquired using the Welch's method power spectral density estimate with a window sized four times smaller than the closest power of two to the signal length, i.e. $7.1873 \times 10^3$, using Hann windowing, with 50 % overlap.

Velocity calculations were performed as follows: the A and B channels[2]were compared using the `MATLAB xcorr()` cross-correlation function. This finds the number of data points of shift necessary to best overly the signals. Given the recording rate, $f_s$, and the data point lag, $i_{lag}$, the time delay, $T_{lag}$, can be found. Then, using the measured distance between the centers of each FLDI pair, $\Delta X$, the average velocity of eddies that contribute to the signal can be found.

$$\frac{i_{lag}}{f_s} = T_{lag} \tag{3.3a}$$

$$\frac{\Delta X}{T_{lag}} = U_{eddies} \tag{3.3b}$$

### 3.3.2 Schlieren Systems

Initial runs were taken of each model with the full scale schlieren of the TALon Mach 4 facility, and the Integrated schlieren system was trialled during the later experiments of the hollow cylinder.

[2]Note that the downstream diode is marked as channel A and given channel 1 on the oscilloscope as it records the upstream focal points due to a horizontal mirroring that occurs at the final focusing lens.

#### Full Scale Schlieren System

The full-scale schlieren setup is comprised of a high-power LED with a high-frequency driver. It is condensed to a point source with a $f = 75\,\text{mm}$, $\varnothing = 50.8\,\text{mm}$ lens and an iris. The beam is collimated, pass though the test section, and focused on a horizontal knife edge using $\varnothing = 31.75\,\text{cm}$ $(12.5\,\text{in})$, $f = 2.54\,\text{m}$ $(100\,\text{in})$ parabolic mirrors, in a typical z-type schlieren setup. The resulting schlieren images are captured with a Photron SA-Z-2100k [52] high speed camera with a Nikon Nikor 150 mm or 300 mm lens depending on required zoom level.

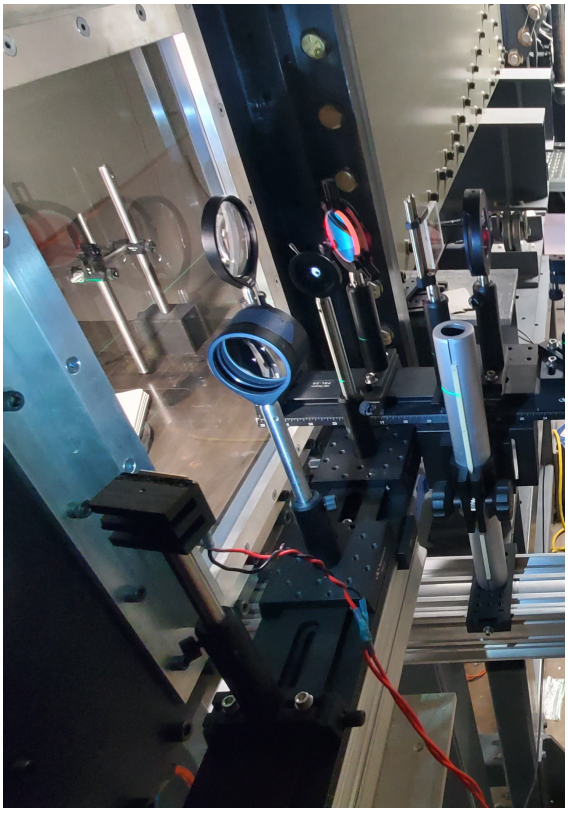
#### Integrated Schlieren System

The integrated schlieren system utilizes the FLDI field lenses for collimation of the schlieren light. Dichroic mirrors are used to pass the schlieren light into and out of the FLDI beam path without interfering with the FLDI Beam. The dichroic mirrors allow the red light of the FLDI to pass through, while reflecting the majority of the light from the white LED. Figure 3.7 illustrates the integrated schlieren incorporated into the 2-point FLDI. Photographs of the integrated schlieren system are available in fig. 3.11. Due to the significantly reduced ratio of diameter to focal length of the FLDI field lenses compared to the schlieren parabolic mirrors, the integrated schlieren system has significantly reduced sensitivity. To account for this, the camera frame rate was reduced by a factor of 10 to 20 kHz and the illumination was maintained, but increasing the schlieren cutoff to nearly 100 %. This was able to increase sensitivity, and shocks and some portions of boundary layers were visible.

## 3.4 Uncertainty Quantification

### 3.4.1 Photo-diode response

As stated above the photo-diodes used in these experiments are Thorlabs PDA36A2 [75]. These diodes have a reported rise time of 29.2 ns and a bandwidth of 12 MHz when unamplified, and a rise time of 219 ns and a bandwidth of 1.6 MHz when amplified with a gain of 10 dB. This should be sufficient to resolve the Nyquist frequency based on the FLDI sampling rate of 20 MHz. Based on some initial results, where the roll-off of the



**(a)** 'Send' side of the UTSI integrated schlieren system as installed.



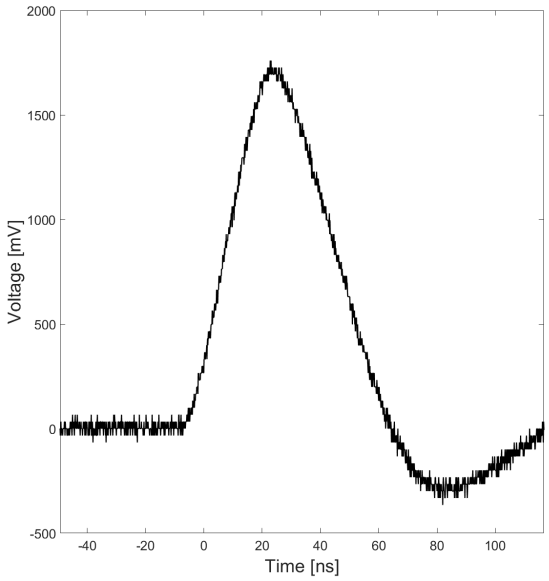
**(b)** 'Receive' side of the UTSI integrated Schlieren system as installed.

**Figure 3.11:** Photographs of the UTSI integrated schlieren system as installed in the TALon Mach 4 Ludwieg Tube.

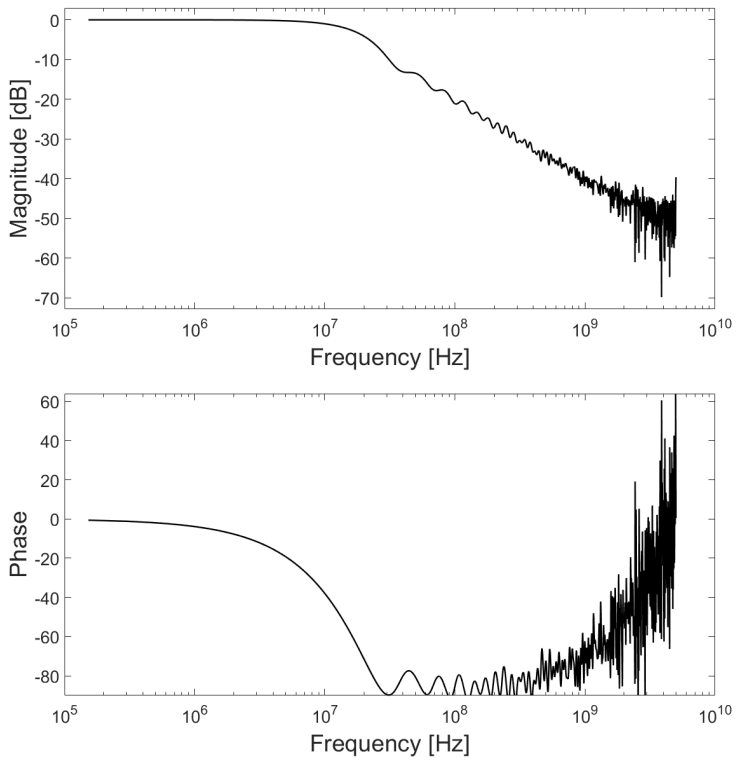
turbulent spectra was slightly faster than the expected $\frac{-5}{3}$, a question arose about whether the photo-diodes were damping the FLDI response. To determine that the photo-diodes were in specification and were not the source of the apparently damped signal, the frequency response function of the photo-diodes was calculated using their response to scattered light from a 1 ns square wave pulse from a Nd-YAG laser. The falling half of this response was taken to be a negative step response, and a Fast Fourier Transform was used to calculate the frequency response. The signal response and frequency response curves are shown in fig. 3.12 for the unamplified case and in fig. 3.13 for the 10 dB gain setting, used when taking measurements on the 24° flare of the Hollow Cylinder Flare. Further, this technique was validated using an example short rise-time photo-diode, a Thorlabs PDA10A2 [74], with a rise time of 2.3 ns and a bandwidth of 150 MHz. Signal and frequency response of the PDA10A2 is shown in fig. 3.14.

These results show that the PDA36A2 Photo-diode responds within specification, above 12 MHz when unamplified, and above 1.6 MHz with a gain of 10 dB. The reported specification of the PDA10A2 is also demonstrated. Thus it is reasonable to conclude that the photo-diodes are not the source of any damping of the high-frequency end of the measured turbulent spectrum.

The other fundamental component of the data acquisition system is the Teledyne LeCroy WaveSurfer 10 oscilloscope. This system however has a possible bandwidth of up to 10 GHz, and so will not have any linearity of aliasing issues at the comparatively slow acquisition rate of 20 MHz. Therefore, and damping of the expected turbulent spectra at hight frequencies is likely due to the spatial filtering of the FLDI due to the finite beam spacing, as outlined by Fulghum [26, p. 65].

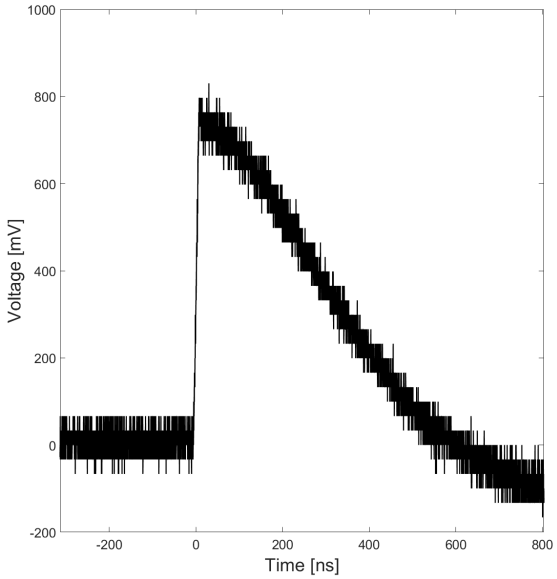



**(a)** 1 ns square wave response.

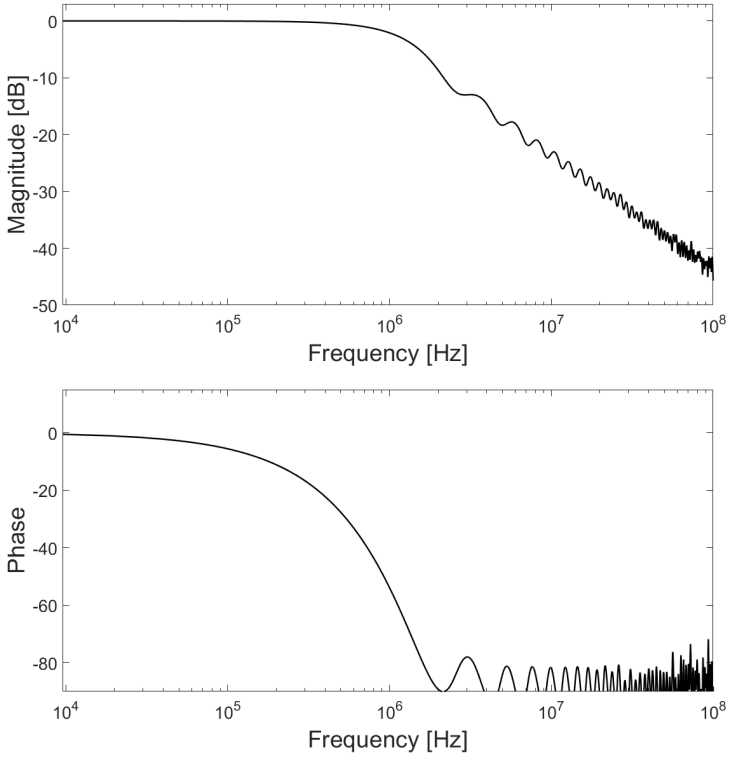



**(b)** Magnitude and phase of calculated frequency response.

**Figure 3.12:** Frequency response of PDA36A2 Photo-diode, used in this experiment, with no gain, as calculated from response to 1 ns square wave.

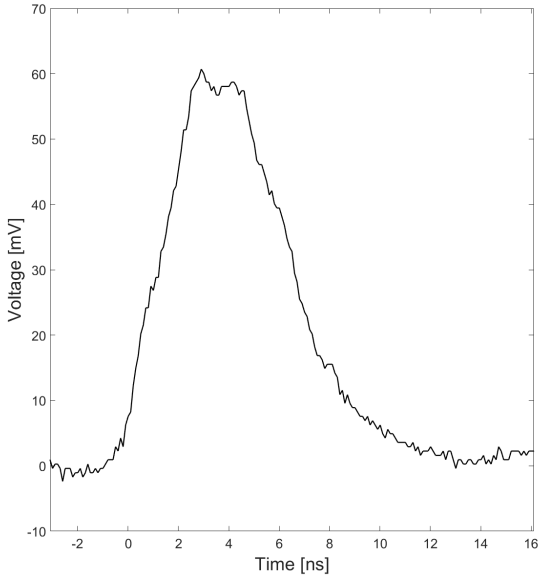



**(a)** 1 ns square wave response.

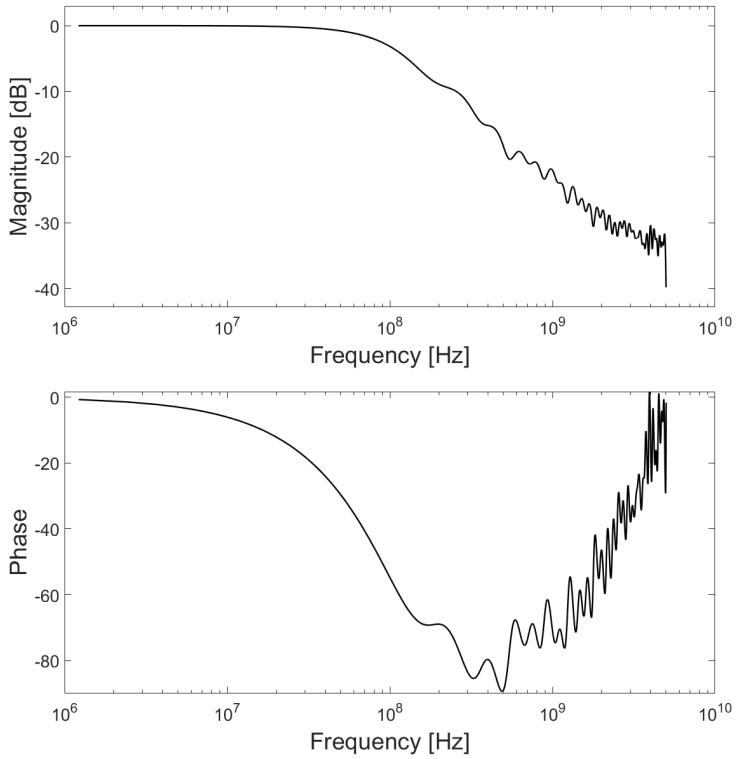



**(b)** Magnitude and phase of calculated frequency response. Note change of $x$-axis.

**Figure 3.13:** Frequency response of PDA36A2 Photo-diode, used in this experiment, with 10 dB gain, as calculated from response to 1 ns square wave.




**(a)** 1 ns square wave response.




**(b)** Magnitude and phase of calculated frequency response.

**Figure 3.14:** Frequency response of example short rise-time Photo-diode as calculated from response to 1 ns square wave.

# Chapter 4

# Results

## 4.1 Hollow Cylinder Flare

### 4.1.1 Schlieren

#### Full-Scale Schlieren

Schlieren with the full-scale facility apparatus has been used to determine the overall behavior of the flow field and positions for investigation with FLDI. Figure 4.1 provides a montage of the flow from the ninth Hollow Cylinder Flare run: un-tripped, $Re = 1.77 \times 10^7\,\mathrm{m}^{-1}$, $f_s = 200\,\mathrm{kHz}$, the images reproduced here are $\Delta = 5 \times 10^{-5}\,\mathrm{s}$ apart. Note the turbulent eddy passing in images 2 and 4. Based on these schlieren results, FLDI locations were selected to measure the boundary layer upstream of the intersection of the separation shock, the separation at the flare junction, and in the center of the flare as viewed in fig. 4.1. Further, note the extremely small size of the laminar boundary layer.

### 4.1.2 FLDI

Twelve FLDI measurements were successfully taken on the hollow cylinder flare at various heights above the model and at three streamwise locations: in the center of the cylinder, upstream of the impingement of the separation shock, $x = 6.35\,\mathrm{cm}$ (2.5 in) from the leading

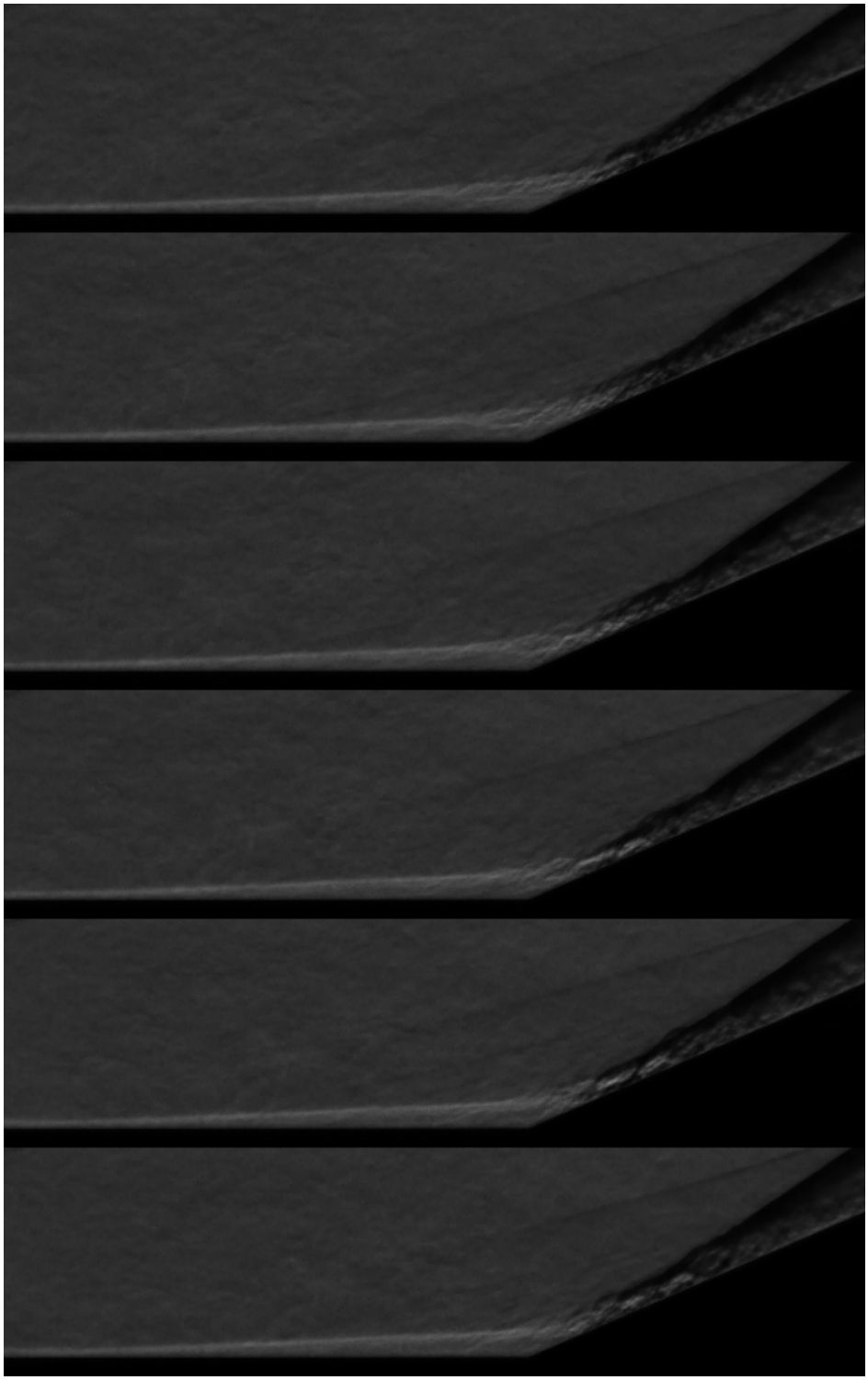


**Figure 4.1:** A montage of the flow from the ninth Hollow Cylinder Flare run, $Re = 1.77 \times 10^7\,\mathrm{m}^{-1}$, $f_s = 200\,\mathrm{kHz}$, images reproduced as recorded, i.e. $\Delta t = 5 \times 10^{-6}\,\mathrm{s}$. Note change in the shape of the separation region above the flare junction from concave to convex in 2 and 4, suggesting a turbulent eddy.

edge; above the flare junction in the separation region, $x = 12.3\,\text{cm}$ $(4.85\,\text{in})$; and in the center of the reattachment on the flare, $x = 15.2\,\text{cm}$ $(6.0\,\text{in})$.

Note that as the 2-point FLDI needs to be aligned with the flow for Taylor's hypothesis to hold, the FLDI beam pairs needed to be rotated for the measurement on the flare. Rather than rotate the whole apparatus, only the laser, 1.5° Wollaston prism and the polarizers were adjusted to the 24° flare angle. This allowed the 2-point FLDI to be aligned with its streamwise spacing parallel to the flare, although the individual FLDI pairs, i.e. $\Delta x_{a,b}$ remained aligned to the horizontal. This resulted in a significant loss of intensity $E_0$, due to absorption in the polarizers, and therefore there is an increased uncertainty in the measurements on the flare. Further, to account for the decreased illumination, the gain was turned up on the photo-diodes, which has a significant negative effect on their response time. For these reasons, future work should rely on rotating the entirely of the FLDI structure, or all polarization optics.

Figure 4.2 outlines the results of these runs using a color waterfall plot. Measurements are grouped on the $y$-axis by the streamwise location of the measurement, and are then sorted by wall-normal position, increasing along the $y$-axis. As should be expected due to the vastly different physics present, the streamwise positing groups are distinct from one another. However, differences in wall-normal position do not show significant differentiation, and in fact the trend is not monotonic. These spectra can be examined in more detail in fig. 4.3, which contains more conventional spectral plots, grouped by streamwise position. It becomes apparent that the measurements in the laminar boundary layer are fairly indistinguishable from the free stream measurement. To some extent, this is reasonable in the laminar boundary layer where there are not large eddies for the FLDI to track. Peak frequencies are in the range of 1.5 kHz, which, based on the sensitivity study, are frequencies that cannot be spatially filtered by the FLDI. This suggests that a significant component of the laminar boundary layer measurement are actually measurement of the turbulent boundary layer on the tunnel walls; however, the roughly three fold increase in energy at these frequencies in the measurements in the laminar boundary layer as compared to the freestream suggest that some behavior of the laminar boundary layer is being measured. As the repeated lowest case at 0.4 mm represents both the lowest and highest energy case, it is reasonable to conclude

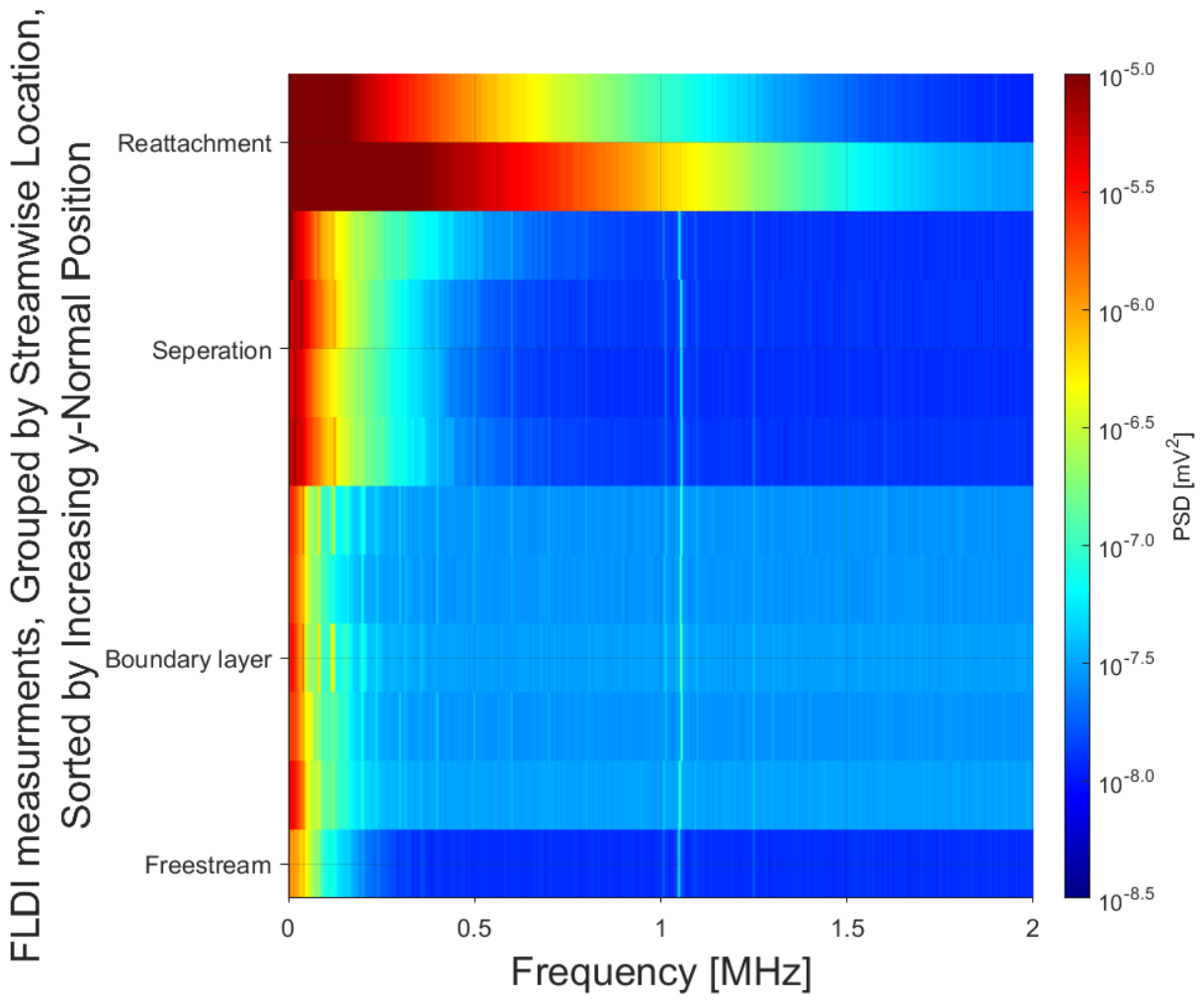



**Figure 4.2:** Color waterfall plot of HCF FLDI measurements. Grouping by streamwise positional is significant, as expected, but by differences caused by wall-normal are subtle and not monotonic

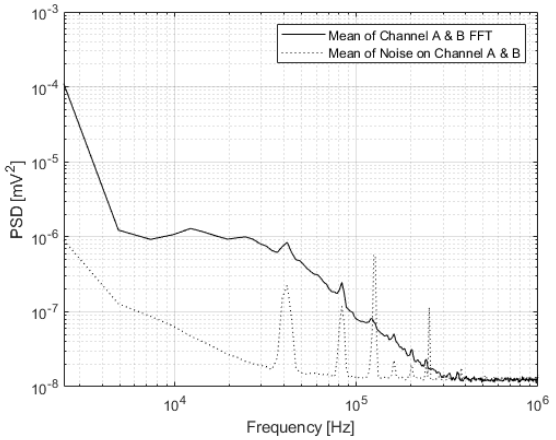
that changes in measurement height through the boundary layer do not have an effect that is measured here. It is surprising, however, that the 2.9 mm case, which is significantly outside of the boundary layer, does not have a spectral density at peak frequency similar in magnitude to the freestream case.

Continuing to the separation region, there is a 2 to 3 fold increase in total energy and a 3 to 4 fold increase in peak frequency. Further, the roll-off angle has changed, clearly showing the effect of turbulent pockets and recirculation in the separation region. Results are not correlated with height in the separation region, except for the 9.4 mm case slightly above it, which has a significant amount of low frequency energy. This is likely due to signal spikes as the separation shock passes between the FLDI beam pairs during the burst of energy as shown in fig. 4.1, although, as this behavior was not apparent again, it is difficult to draw conclusions. This is supported by the low correlation between the A and B channels for this low frequency behavior, suggesting it is not caused by something convecting downstream.

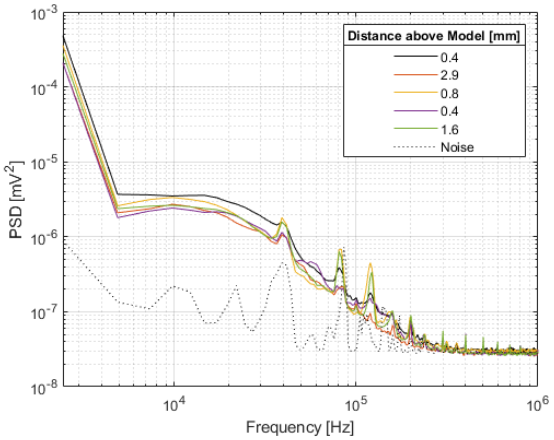
Finally, the reattachment region on the flare shows typical broadband turbulence, with roughly double the energy at peak frequencies to the separation region.. The measurement at 1.2 mm, closer to the flare, shows higher peak frequencies, but comparable total energy to the 2.4 mm case. Signal filtering by both the FLDI and photo-diodes is apparent in the 1.2 mm. Future work will need to further explore this region without gain on the photo diodes, and perhaps with smaller FLDI beam spacing in order to get a better sense of the turbulence roll-off angle, but these results demonstrate the feasibility of that approach.

### Integrated Schlieren

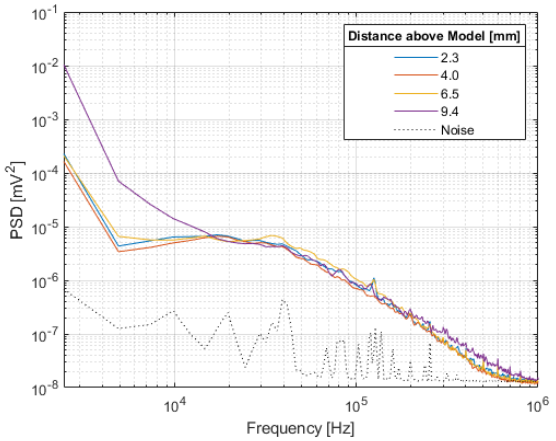
Integrated Schlieren was used on the the HCF during the FLDI runs. Figure 4.4 shows a montage from the last FLDI run, along the flare. As necessary settings to detect the boundary layer due to the reduced sensitivity of the integrated schlieren system, were still being determined, the turbulent reattachment region is not clearly visible. Note the out of focus appearance of the shock due to the multiple exposure of the camera in order to increase sensitivity.



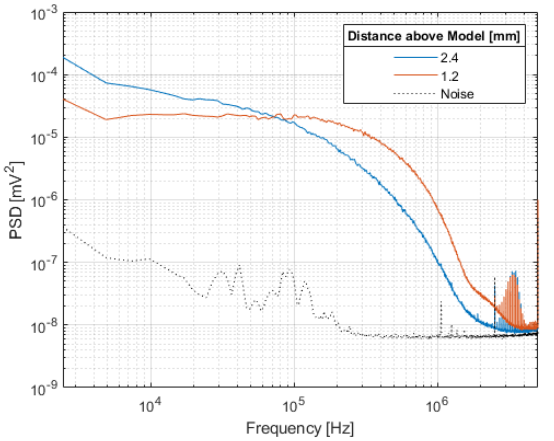

**(a)** Free-stream FLDI measurement




**(b)** Spectra on HCF model, $x = 6.35\,\text{cm}$ (2.5 in), along the laminar boundary layer.




**(c)** Spectra on HCF model, $x = 12.3\,\text{cm}$ (4.85 in), above flare junction. Note change of $y$ axis.




**(d)** Spectra on HCF model, $x = 15.2\,\text{cm}$ (6.0 in), at the center of reattachment. Note change of $x$ axis.

**Figure 4.3:** Spectra from FLDI measurements on HCF model at different $x$-locations.

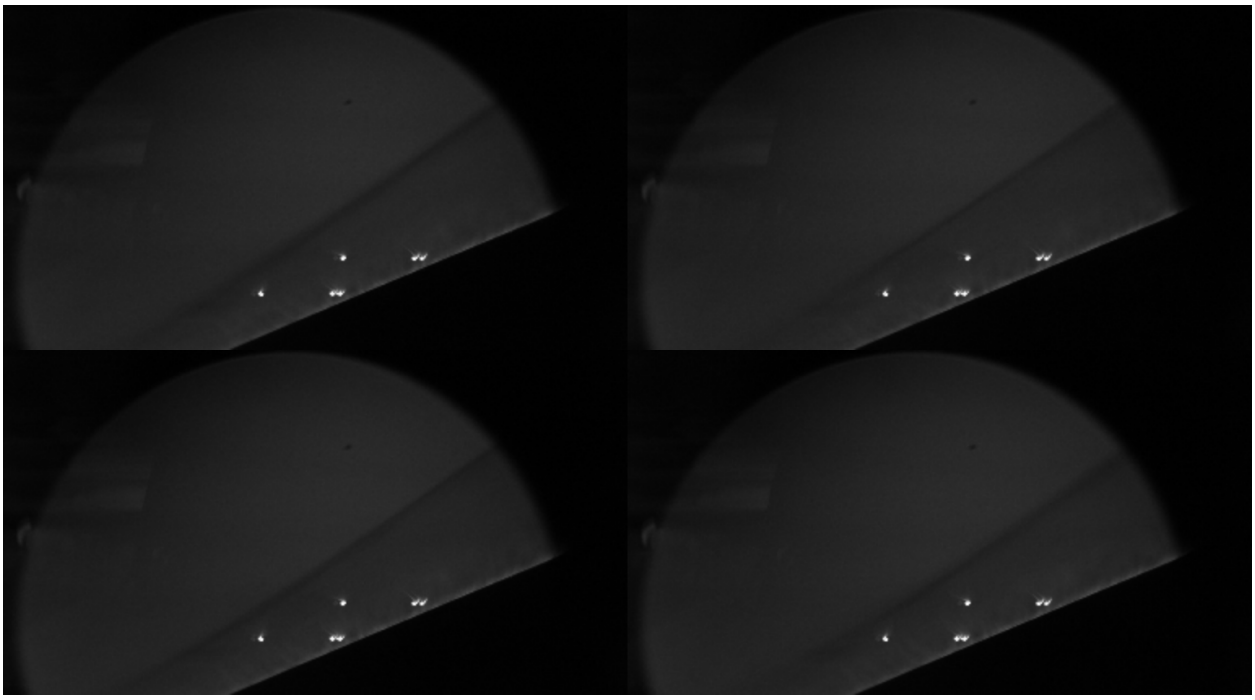


**Figure 4.4:** A montage of integrated schlieren of the hollow cylinder flare reattachment region. Note the reflection of the FLDI off the back surface of the dichroic mirrors, showing up as a 3rd point spaced away from each FLDI beampair.

## 4.2 Hollow Cylinder

### 4.2.1 Schlieren

#### Full-Scale Schlieren

Figure 4.5 provides a montage of the boundary layer in the turbulent region near the end of the model during the 27th run of the Hollow Cylinder, $Re = 1.49 \times 10^7\,\mathrm{m}^{-1}$, $f_s = 200\,\mathrm{kHz}$, reproduced every ten images, i.e. $\Delta t = 5 \times 10^{-5}\,\mathrm{s}$. Both the aforementioned shock from the supersonic jets exiting the model as well as rolling motion indicative of turbulent eddies upstream of this are visible. In order to facilitate further analysis, the boundary layer height was found along the model using Canny edge-finding in `MATLAB` [12], averaged across every image. Reasonable growth along the boundary layer is demonstrated, and both the change in slope in the transitional region as well as the shock at the downstream extreme of the model are observable in fig. 4.6.

Spectra were calculated from the full-scale schlieren. Figure 4.7 shows a false color image of the relative intensity of frequency oscillation in the range of 1.5 kHz in each pixel. This clearly shows the region with a significant amount of turbulence, likely a fully turbulent boundary layer. However, extractions of the full spectra, averaged over a region of pixels, show differences in power, but not differences in spectral shape (see fig. 4.8. The only slight difference in spectral shape is behind the shock from the supersonic jet.

#### Integrated Schlieren

Due to the need to adjust the schlieren every time the FLDI was moved, only five of the twelve integrated schlieren runs were successful in imaging the boundary layer. Further, as the LED and camera were both mounted on separate rails from FLDI, vibration during the run causes the schlieren system to sway in and out of aliment, leading to only a hundred or so images that are usable in a row. Future work using this technique will need to further integrate the optomechanics holding the FLDI and schlieren systems to correct these issues. Figure 4.9 shows a montage of integrated schlieren, which clearly demonstrates the boundary layer height. This measurement was coupled with the 2-point FLDI velocity estimate to calculate

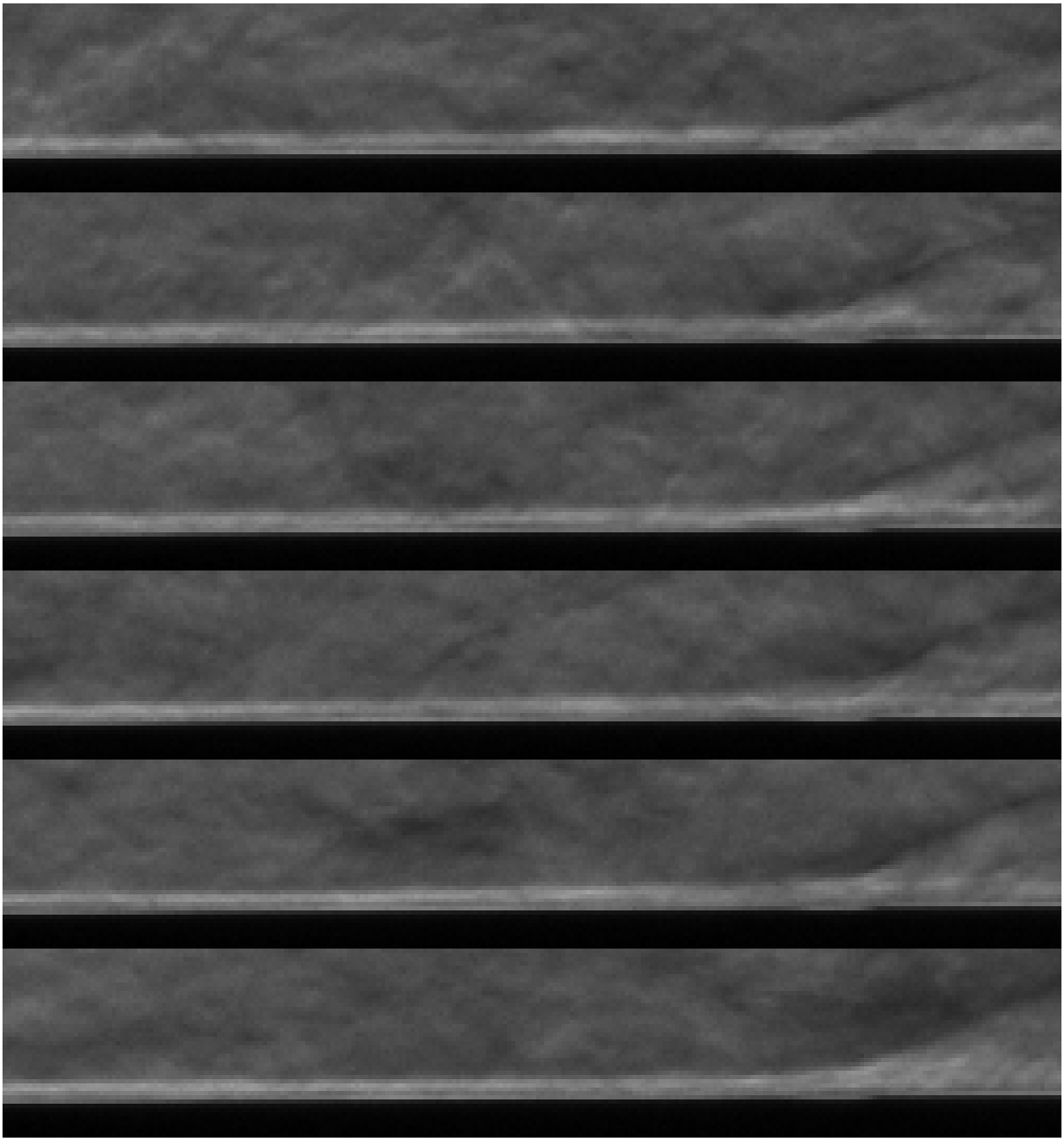


**Figure 4.5:** A montage of the boundary layer above the Hollow Cylinder, zoomed into the turbulent region, $Re = 1.49 \times 10^7\,\mathrm{m}^{-1}$, $f_s = 200\,\mathrm{kHz}$, reproduced every ten images, i.e. $\Delta t = 5 \times 10^{-5}\,\mathrm{s}$. Note the shock from the supersonic jets exiting the holes in the model, as well as the turbulent eddies before this shock.

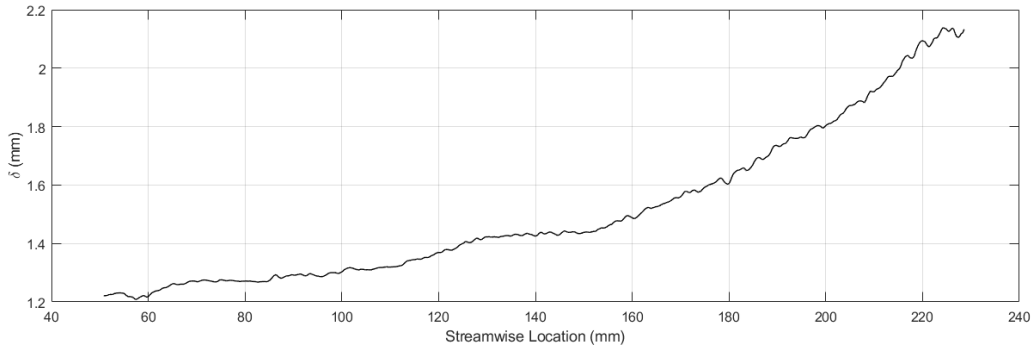



**Figure 4.6:** Calculated boundary layer height along the hollow cylinder model, demonstrating a reasonable boundary layer growth and the expected change in slope during transition.

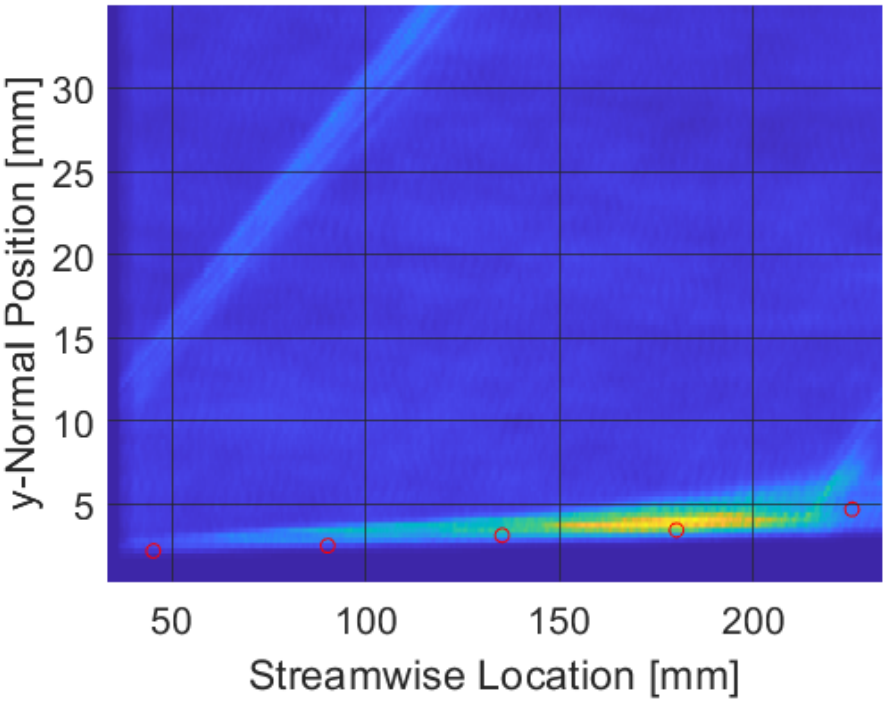



**Figure 4.7:** Schlieren image colored with frequency fluctuation intensity in the range of 1.5 kHz, centers of extraction for fig. 4.8 are shown as red circles.

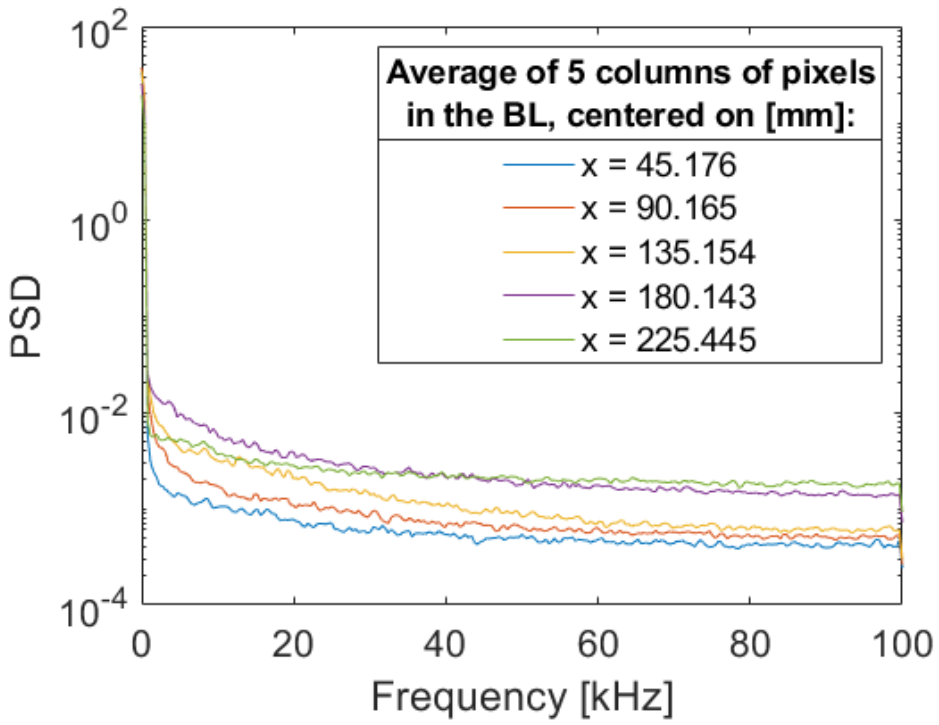



**Figure 4.8:** Spectra extracted from schlieren on the Hollow Cylinder. Results show a difference in intensity, but not spectral shape.

a Strouhal number estimate of peak frequency for that test. The Strouhal number estimate is marked in green in fig. 4.11.

### 4.2.2 FLDI

As compared to the other methods discussed so far, 2-point FLDI was able to pinpoint the transition location. Looking at the color waterfall plot, fig. 4.10, a clear change occurs between a local Reynolds number of $1.63 \times 10^5$ to $1.71 \times 10^5$. Other than this shift, the spectra display gradual, monotonic change. Looking at the spectra, in fig. 4.11 there is a clear shift from a laminar, low-frequency-peak spectral distribution, to spectra with significant energy at the predicted frequency scale of the boundary layer (marked in green), at a local Reynolds number of $Re = 1.71 \times 10^5$. This structure then turns to a full turbulent spectra around $Re = 2.58 \times 10^5$. Thus 2-Point FLDI is capable capable of determining the boundary layer state, and transition location can be found to within the accuracy of positioning the diagnostic. Some of the behavior in the transition region is interesting, including the 'jagged' shape of the spectra at $Re = 1.74e5$. One explanation this might be that the FLDI is located to far from the model and the boundary layer edge is passing over the FLDI beams as turbulent eddies pass.

Additional interesting results are apparent from the spectrogram of the FLDI signal, shown in fig. 4.12, which suggest an intermittent behavior in regions that are undergoing transition. Future work will involve finding an intermittence distribution for these spectra, further quantifying the transitional region along the model. A sudden onset of turbulence occurs at $t = 0.14\,\mathrm{s}$ and $t = 0.08\,\mathrm{s}$ for the $Re = 1.71 \times 10^5$ and $Re = 1.74 \times 10^5$ cases, respectively. No obvious sign of diaphragm impact on the model was present for these runs; however the model being struck by diaphragm material is the current hypothesis for the cause of this sudden onset. The apparent intermittent behavior at $Re = 2.58 \times 10^5$ may suggest that the boundary layer is not completely turbulent until $Re = 3.34 \times 10^5$ and therefore that the spectrogram is a more reliable visualization of FLDI results in transitional regions.

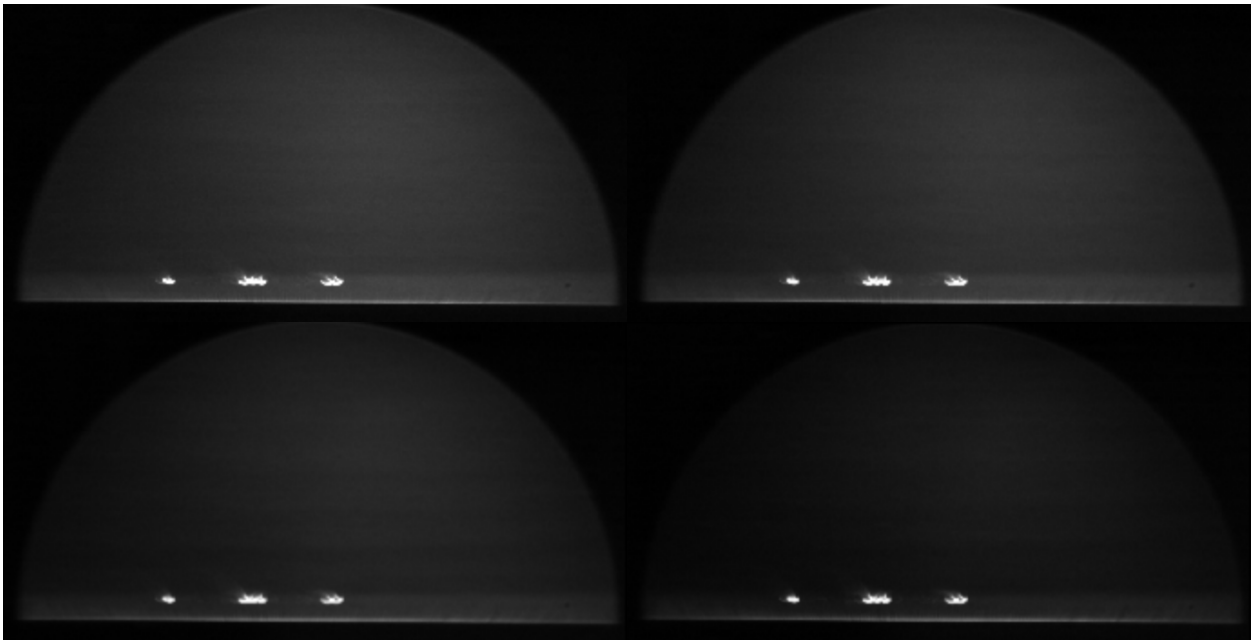


**Figure 4.9:** A montage of the boundary layer above the Hollow Cylinder, as imaged with integrated schlieren $R_{e_x} = 1.706 \times 10^7\,\mathrm{m}^{-1}, Re = 1.71 \times 10^5, f_s = 20\,\mathrm{kHz}$, reproduced every image.

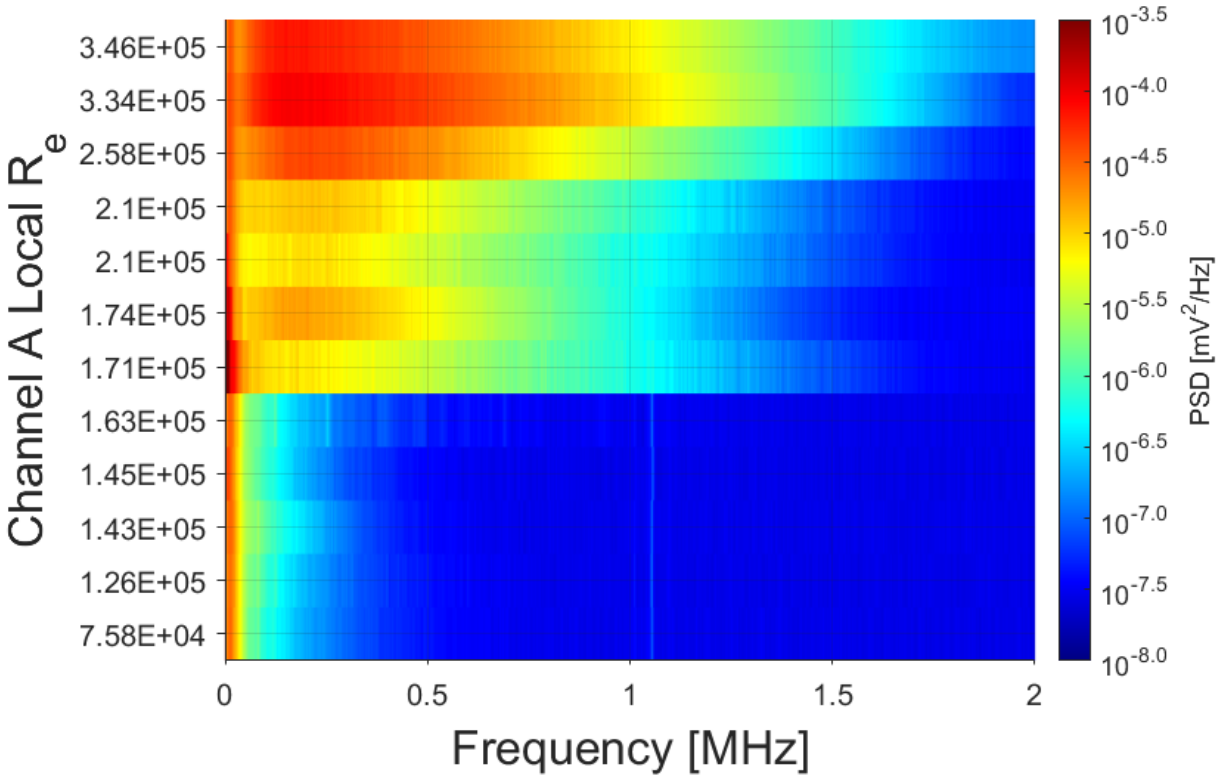



**Figure 4.10:** Color waterfall plot of HC runs, using calculated local Re

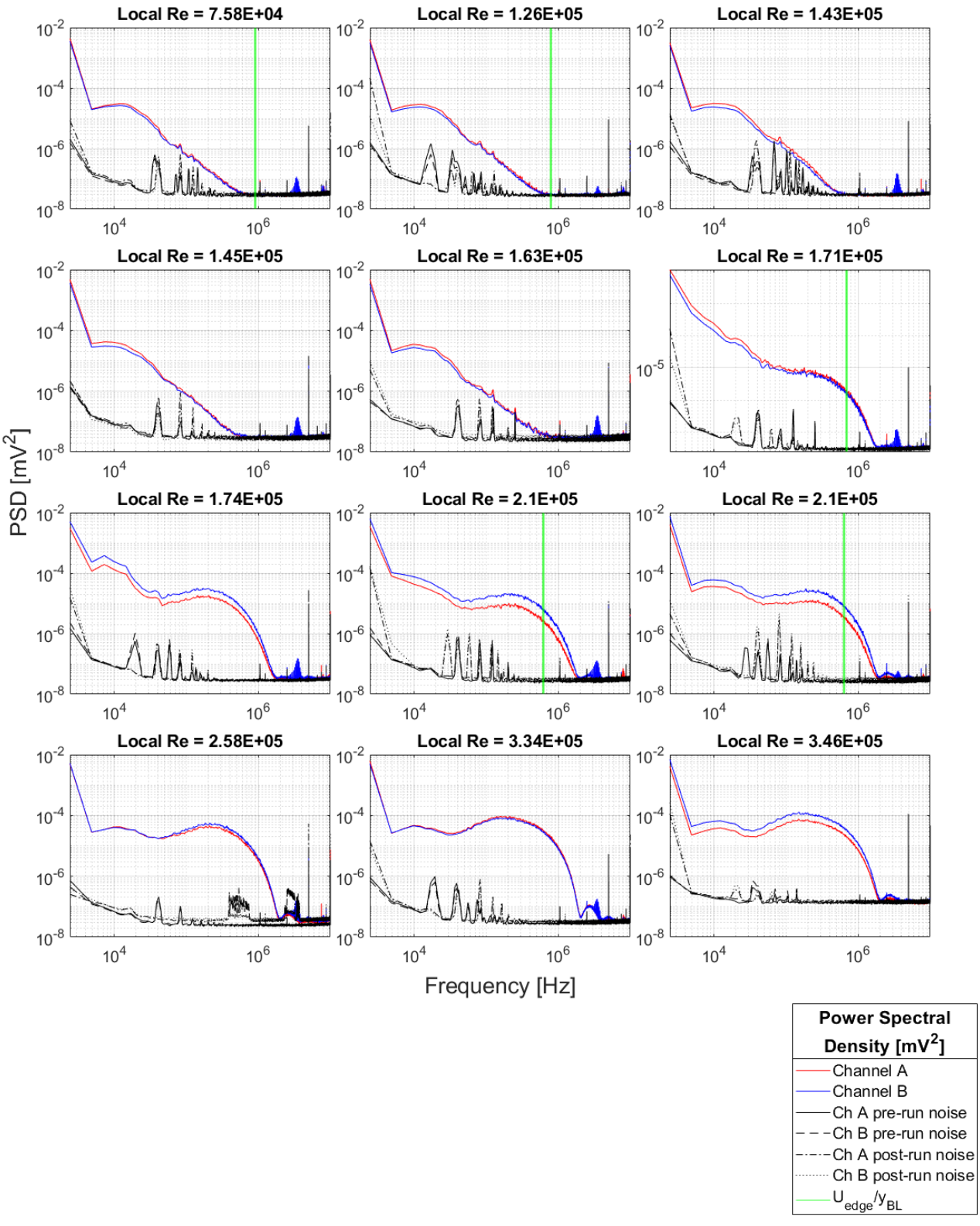



**Figure 4.11:** Density Fluctuation spectra calculated using 2-point FLDI along the Hollow Cylinder model. Green lines mark the estimated peak frequency of the turbulent spectra using a Strouhal analysis. Legend at left.

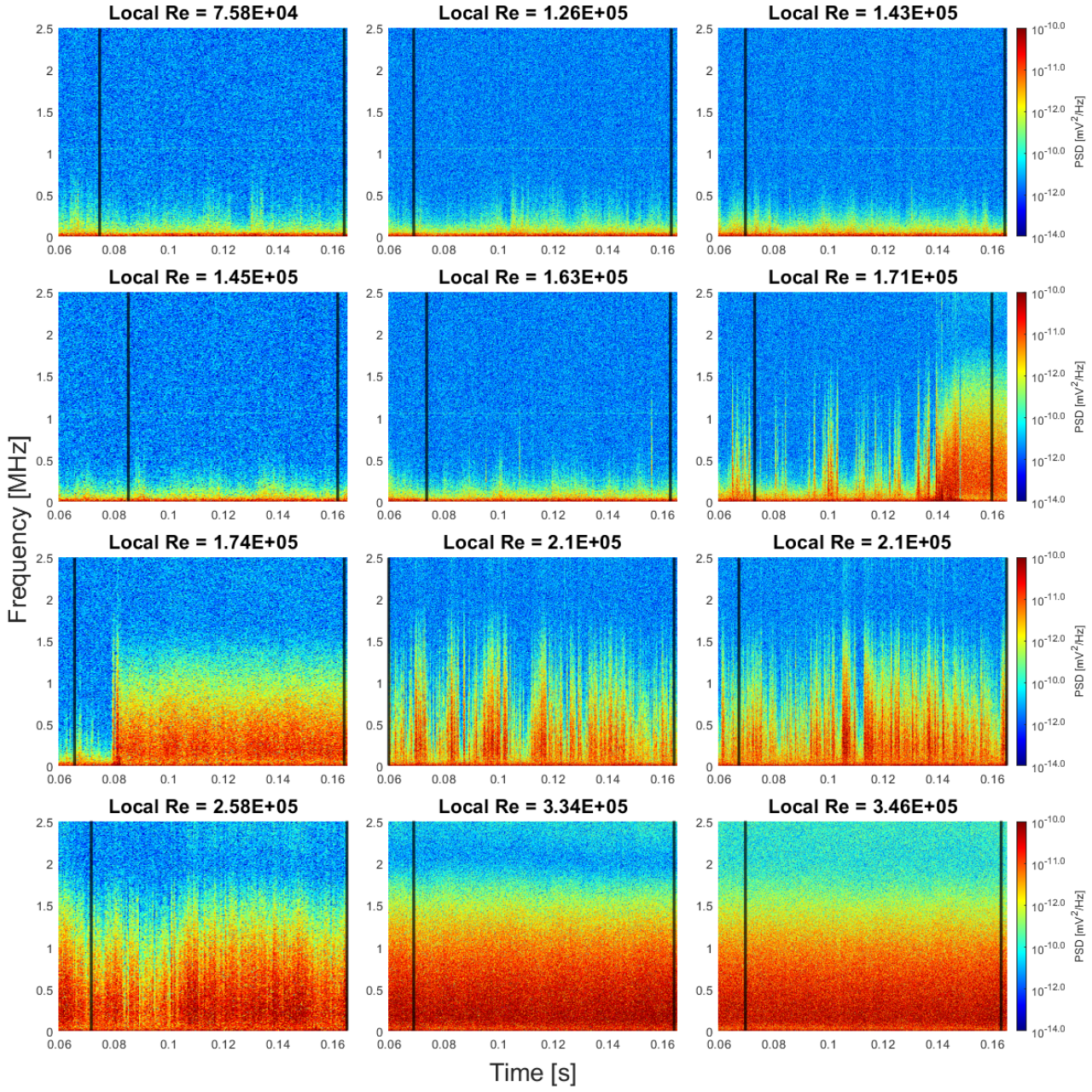



**Figure 4.12:** Spectrogram of 2-point FLDI measurement along the Hollow Cylinder model, showing the change in spectra in time. Black lines mark the start and end of quasi-steady-stagnation conditions.

# Chapter 5

# Conclusions and Future Work

## 5.1 Conclusion

Despite 80 years of continued progress, the field of hypersonics has a number of open questions. The urgency and motivation to answer these questions has substantially increased in the last 20 years as hypersonic capabilities have come to be one of the highest priories for the Department of Defense and foreign governments. The design of broad class of hypersonic vehicles, the air-breathing, high-lift, hypersonic cruise missile, is complicated by system integration considerations, and progress in the understanding and prediction of a number of viscous phenomena, such as boundary layer transition and the shock wave boundary layer interaction would substantially decrease technical risk in the design and deployment of these systems.

In order to further the experimental investigation of these phenomena, this work undertook to construct and demonstrate the use of a focused laser differential interferometer in the University of Tennessee Space Institute's Mach 4 Ludwieg tube in the Tennessee Aerothermodynamics Laboratory. This optical diagnostic is well suited to measuring these viscous phenomena due to its high frequency response and its non-intrusive nature. In order to facilitate further use of the system at UTSI, the theory and design of such a system was discussed at length.

In order to determine the effectiveness of the FLDI system, two aluminum models were constructed, a hollow cylinder and a hollow cylinder flare. The hollow cylinder flare is

increasingly being used as a canonical axisymmetric SBLI generator, and so it lends itself to this study well. Additionally, schlieren was used to further understand the flow field around these models, and an integrated schlieren design was tested, which may simplify future combined FLDI/schlieren studies. Throughout the experiment, a number of lessons have been learned which have directly affected the design of upcoming experiments at the University Tennessee Space Institute.

This study began by asking to what degree optical diagnostics can determine the state of a Mach 4 axisymmetric boundary-layer, and has since demonstrated that FLDI is more than capable of measuring boundary layer physics in the case of transitional and turbulent boundary layers. The system was able to pinpoint the onset of the transitional region significantly upstream of where schlieren could, and was even able to differentiate the fully turbulent region of the boundary layer from regions that were still transitioning. Some promising results from the spectrogram of runs taken along the Hollow Cylinder suggest that FLDI may be able to project the length of a transition region based on an intermittence distribution.

In the case of a laminar boundary layer; however, FLDI is not suited. The lack of turbulent eddies to generate a strong refractive index change for the FLDI results in the interferometer being unable to differentiate the wind tunnel wall boundary layer from the laminar boundary layer of interest. Even in regions of significant fluctuating motion, such as the separation region on the Hollow Cylinder Flare, the interferometer may struggle to meticulously probe the flow field.

## 5.2 Future Work

A number of avenues remain to further progress this work.

### 5.2.1 FLDI Study of Transitional SBLI and Upstream Influence Shock

First and foremost, the work that motivated this study remains to be completed. The laminar SBLI studied here is fairly well understood, and although this work is an important stepping of point for future study at UTSI, its relevance to the broader aerospace community may be limited. One direct effect of this study on the study of Transitional SBLI at UTSI is in the design of the new model. Due to lessons learned here, the new model constructed has an adjustable flare, and importantly, is mounted from that flare, significantly reducing the need to meticulously move the FLDI and remeasure its position.

### 5.2.2 Improvements to FLDI Apparatus

Additionally, a fair bit of work could go into improving the 2-point FLDI system used in this work. Studies are benign to demonstrate multi-FLDI or array-FLDI systems that are a direct improvement to this system in terms of flow field structure measurement and facility use time. Outside of these paradigm-shifting changes, a number of direct upgrades could be made. These generally fall into a category of making the system more stable, and transitioning it from a 'bread-boarding' configuration to something more permanent. Reducing the number of adjustable parts, employing vibration reducing optomechanics, and possibly changing optical rails for lens tube and cage systems may significantly reduce the amount that the FLDI needs to be adjusted in practice. Further, if the difficulties related to the relative motion between the model, tunnel, and FLDI can be sufficiently resolved, that would be significant progress for the system at UTSI.

### 5.2.3 Interferometric Schlieren

Unfortunately, the integrated schlieren system tested in this work was not reliable. Primarily, this is due the the significant reduction in sensitivity due to the focal length and diameter of the FLDI field lenses. This let to the use of a slower schlieren frame rate, motion blur due to long exposure times, and significantly reduced relevant information being extracted from the boundary layer. One possible avenue to improve this system is the introduction of Schlieren

Interferometry [62, p. 132]. Such a device could be constructed by passing the schlieren light though one of the Wollaston prisms before it is diverted by the dichroic mirror. Although this technique from a physics perspective is closer to an imaging LDI than an interfering Schlieren system (the measurement is of the gradient as in interferometer rather than of the direct refractive index), the increase in sensitivity and ease of construction make it a promising option. Further, the combination of such a system aligned for an finite-fringe interferogram, and edge-finding techniques in `MATLAB` may allow quantitative results.

# Bibliography

[1] Anderson, J. D. (2004). *Modern compressible flow : with historical perspective*. McGraw-Hill, Boston, 3 edition, ISBN: 0-07-242443-5 978-0-07-242443-0. 19

[2] Anderson, J. D. (2019). *Hypersonic and high-temperature gas dynamics*. AIAA Education Series. American Institute of Aeronautics ands Astronautics, Inc., Reston, Virginia, ISBN: 978-1-62410-514-2. OCLC: 1136504685. 1, 13, 14, 20

[3] Babinsky, H. and Harvey, J., editors (2011). *Shock wave-boundary-layer interactions*. Cambridge Aerospace Series. Cambridge University Press, Cambridge ; New York, ISBN: 978-0-521-84852-7. OCLC: ocn701672464. 22

[4] Bathel, B. F., Weisberger, J. M., Herring, G. C., King, R. A., Jones, S. B., Kennedy, R. E., and Laurence, S. J. (2020). Two-point, parallel-beam focused laser differential interferometry with a Nomarski prism. *Applied Optics*, 59(2):244, ISSN: 1559-128X, 2155-3165, DOI: 10.1364/AO.59.000244, https://www.osapublishing.org/abstract.cfm?URI=ao-59-2-244. 21, 36

[5] Benay, R., Chanetz, B., Mangin, B., Vandomme, L., and Perraud, J. (2006). Shock Wave/Transitional Boundary-Layer Interactions in Hypersonic Flow. *AIAA Journal*, 44(6):1243–1254, ISSN: 0001-1452, 1533-385X, DOI: 10.2514/1.10512, http://arc.aiaa.org/doi/10.2514/1.10512. 19, 22

[6] Benitez, E. K., Esquieu, S., Jewell, J. S., and Schneider, S. P. (2020a). Instability Measurements on an Axisymmetric Separation Bubble at Mach 6. In *AIAA AVIATION 2020 FORUM*, VIRTUAL EVENT. American Institute of Aeronautics and Astronautics, ISBN: 978-1-62410-598-2, DOI: 10.2514/6.2020-3072, https://arc.aiaa.org/doi/10.2514/6.2020-3072. 33

[7] Benitez, E. K., Jewell, J. S., and Schneider, S. P. (2020b). Focused Laser Differential Interferometry for Hypersonic Flow Instability Measurements with Contoured Tunnel Windows. In *AIAA Scitech 2020 Forum*, Orlando, FL. American Institute of Aeronautics and Astronautics, ISBN: 978-1-62410-595-1, DOI: 10.2514/6.2020-1282, https://arc.aiaa.org/doi/10.2514/6.2020-1282. 33

[8] Bertin, J. J. and Cummings, R. M. (2003). Fifty years of hypersonics: where we've been, where we're going. *Progress in Aerospace Sciences*, 39(6-7):511–536, ISSN: 03760421, DOI: 10.1016/S0376-0421(03)00079-4, https://linkinghub.elsevier.com/retrieve/pii/S0376042103000794. 1, 3

[9] Bonnet, J. P., Grésillon, D., and Taran, J. P. (1998). NONINTRUSIVE MEASUREMENTS FOR HIGH-SPEED, SUPERSONIC, AND HYPERSONIC FLOWS. *Annual Review of Fluid Mechanics*, 30(1):231–273, ISSN: 0066-4189, 1545-4479, DOI: 10.1146/annurev.fluid.30.1.231, http://www.annualreviews.org/doi/10.1146/annurev.fluid.30.1.231. 16, 17

[10] Born, M. and Wolf, E. (1999). *Principles of optics; electromagnetic theory of propagation, interference, and diffraction of light, by Max Born and Emil Wolf, with contributions by A.B. Bhatia [et al.* Pergamon Press, Oxford, New York, 7 edition, ISBN: 978-0-08-013987-6. OCLC: 45634897. 25, 28, 29

[11] Button, K. (2018). The New Arms Race. *Aerospace America*, 56(6):20. 5, 6

[12] Canny, J. (1986). A Computational Approach to Edge Detection. *IEEE Transactions on Pattern Analysis and Machine Intelligence*, PAMI-8(6):679–698, ISSN: 1939-3539, DOI: 10.1109/TPAMI.1986.4767851. Conference Name: IEEE Transactions on Pattern Analysis and Machine Intelligence. 69

[13] Ceruzzi, A. and Cadou, C. P. (2017). Turbulent Air Jet Investigation using Focused Laser Differential Interferometry. In *53rd AIAA/SAE/ASEE Joint Propulsion Conference*, Atlanta, GA. American Institute of Aeronautics and Astronautics, ISBN: 978-1-62410-511-1, DOI: 10.2514/6.2017-4834, https://arc.aiaa.org/doi/10.2514/6.2017-4834. 17, 28, 29, 33, 48

[14] Ceruzzi, A. and Cadou, C. P. (2019). Simultaneous Velocity and Density Gradient Measurements using Two-Point Focused Laser Differential Interferometry. In *AIAA Scitech 2019 Forum*, San Diego, California. American Institute of Aeronautics and Astronautics, ISBN: 978-1-62410-578-4, DOI: 10.2514/6.2019-2295, https://arc.aiaa.org/doi/10.2514/6.2019-2295. 17, 36

[15] Ceruzzi, A., Callis, B., Weber, D., and Cadou, C. P. (2020). Application of Focused Laser Differential Interferometry (FLDI) in a Supersonic Boundary Layer. In *AIAA Scitech 2020 Forum*, Orlando, FL. American Institute of Aeronautics and Astronautics, ISBN: 978-1-62410-595-1, DOI: 10.2514/6.2020-1973, https://arc.aiaa.org/doi/10.2514/6.2020-1973. 36

[16] Collicott, S., Schneider, S., and Messersmith, N. (1996). Review of optical diagnostic methods for hypersonic low-noise facilities. In *34th Aerospace Sciences Meeting and Exhibit*, Reno,NV,U.S.A. American Institute of Aeronautics and Astronautics, DOI: 10.2514/6.1996-851, http://arc.aiaa.org/doi/10.2514/6.1996-851. 16

[17] Combs, C. S., Lash, E. L., Kreth, P. A., and Schmisseur, J. D. (2018). Investigating the Unsteady Dynamics of Cylinder-Induced Shock-Wave/Transitional Boundary-Layer Interactions. *AIAA journal*, 56(4):1588–1599, ISSN: 0001-1452, DOI: 10.2514/1.J056553, https://arc.aiaa.org/doi/pdf/10.2514/1.J056553. 14, 22

[18] Covault, C. (2009). STS-119 Shuttle Report: Discovery's re-entry to collect hypersonic research. https://spaceflightnow.com/shuttle/sts119/090327blt/index.html. 3, 4

[19] Crawford, F. S. j. (1968). *Waves*. Number 3 in Berkeley Physics Course. Education Development Center, Inc., Newton, MA, 3 edition, https://ia902702.us.archive.org/15/items/Waves_371/Berkeley3-Waves_text.pdf. 25

[20] Crystals, U. (2020). Wollaston Prisms - alpha-BBO, Quartz, YVO4, Calcite, MgF2. https://unitedcrystals.com/Wollaston.html. 49

[21] Cummings, R. M., Mason, W. H., Morton, S. A., and McDaniel, D. R. (2015). *Applied Computational Aerodynamics: A Modern Engineering Approach*. Cambridge Aerospace Series. Cambridge University Press, Cambridge, ISBN: 978-1-107-05374-8. OCLC: 913052106. 10

[22] Dolling, D. S. (2001). Fifty Years of Shock-Wave/Boundary-Layer Interaction Research: What Next? *AIAA Journal*, 39(8):1517–1531, ISSN: 0001-1452, DOI: 10.2514/2.1476,

https://doi.org/10.2514/2.1476. Publisher: American Institute of Aeronautics and Astronautics _eprint: https://doi.org/10.2514/2.1476. 22

[23] Douglas B. Murphy, Jan Hinsch, Edward D. Salmon, Kenneth R. Spring, Matthew J. Parry-Hill, Robert T. Sutter, and Michael W. Davidson (2016). Wavefront Shear in Wollaston and Nomarski Prisms. https://micro.magnet.fsu.edu/primer/java/dic/wollastonwavefronts/. 36

[24] Durão, D. F. G., Heitor, M. V., Whitelaw, J. H., and Witze, P. O., editors (1992). *Combustings Flow Diagnostics*. Springer Netherlands, Dordrecht, ISBN: 978-94-010-5142-2 978-94-011-2588-8, DOI: 10.1007/978-94-011-2588-8, http://link.springer.com/10.1007/978-94-011-2588-8. 16

[25] Economist, T. (2019). Hypersonic missiles - Gliding missiles that fly faster than Mach 5 are coming | Science & technology. *The Economist*, https://www.economist.com/science-and-technology/2019/04/06/gliding-missiles-that-fly-faster-than-mach-5-are-coming. 7, 8

[26] Fulghum, M. R. (2014). *Turbulence Measurements In High-speed Wind Tunnels Using Focusing Laser Differential Interferometry*. PhD Thesis, The Pennsylvania State University. 17, 24, 25, 27, 28, 29, 33, 34, 35, 48, 58, 96

[27] Gaitonde, D. V. (2015). Progress in shock wave/boundary layer interactions. *Progress in Aerospace Sciences*, 72:80–99, ISSN: 03760421, DOI: 10.1016/j.paerosci.2014.09.002, https://linkinghub.elsevier.com/retrieve/pii/S0376042114000815. 14, 15, 22, 23

[28] Gerrard, A. and Burch, J. M. (1975). *Introduction to matrix methods in optics*. Wiley Series in Pure and Applied Optics. John Wiley & Sons, Ltd., London, 1 edition, ISBN: 0471296856 9780471296850471 29685 6. 25

[29] Ghosh, G. (1999). Dispersion-equation coefficients for the refractive index and birefringence of calcite and quartz crystals. *Optics Communications*, 163(1-3):95–102, ISSN: 00304018, DOI: 10.1016/S0030-4018(99)00091-7, https://linkinghub.elsevier.com/retrieve/pii/S0030401899000917. 28, 29, 30

[30] Gladstone, J. H. and Dale, T. P. (1863). Researches on the refraction, dispersion, and sensitiveness of liquids. *Philosophical Transactions of the Royal Society of London*, 153:317–343, DOI: 10.1098/rstl.1863.0014, https://royalsocietypublishing.org/doi/abs/10.1098/rstl.1863.0014. Publisher: Royal Society. 27

[31] Gregory, J. W., Asai, K., Kameda, M., Liu, T., and Sullivan, J. P. (2008). A review of pressure-sensitive paint for high-speed and unsteady aerodynamics. *Proceedings of the Institution of Mechanical Engineers, Part G: Journal of Aerospace Engineering*, 222(2):249–290, ISSN: 0954-4100, 2041-3025, DOI: 10.1243/09544100JAERO243, http://journals.sagepub.com/doi/10.1243/09544100JAERO243. 43

[32] Hameed, A., Parziale, N. J., Paquin, L. A., Butler, C., and Laurence, S. J. (2020). Hypersonic Slender-Cone Boundary-Layer Instability in the UMD HyperTERP Shock Tunnel. In *AIAA Scitech 2020 Forum*, Orlando, FL. American Institute of Aeronautics and Astronautics, ISBN: 978-1-62410-595-1, DOI: 10.2514/6.2020-0362, https://arc.aiaa.org/doi/10.2514/6.2020-0362. 36

[33] Jimenez, J. (2004). TURBULENT FLOWS OVER ROUGH WALLS. *Annual Review of Fluid Mechanics*, 36(1):173–196, ISSN: 0066-4189, 1545-4479, DOI: 10.1146/annurev.fluid.36.050802.122103, http://arjournals.annualreviews.org/doi/abs/10.1146%2Fannurev.fluid.36.050802.122103. 13

[34] Kianvashrad, N. and Knight, D. D. (2016). Simulation of Hypersonic Shock Wave Laminar Boundary Layer Interaction on Hollow Cylinder Flare. In *54th AIAA Aerospace Sciences Meeting*, San Diego, California, USA. American Institute of Aeronautics and Astronautics, ISBN: 978-1-62410-393-3, DOI: 10.2514/6.2016-0349, http://arc.aiaa.org/doi/10.2514/6.2016-0349. 22

[35] Klare, M. T. (2019). An 'Arms Race in Speed': Hypersonic Weapons and the Changing Calculus of Battle. *Arms Control Today*, 49(5):6+, ISSN: 0196125X, https://link.gale.com/apps/doc/A592785946/AONE?u=tel_a_utl&sid=AONE&xid=986cb21d. Section: 6. 7

[36] Knight, D. and Mortazavi, M. (2017). Hypersonic Shock Wave Transitional Boundary Layer Interactions - A Review. In *47th AIAA Fluid Dynamics Conference*,

page 26, Denver, Colorado. American Institute of Aeronautics and Astronautics, DOI: 10.2514/6.2017-3124. 13, 14, 22

[37] Korkegi, R. H. (1971). Survey of viscous interactions associated with high Mach number flight. *AIAA Journal*, 9(5):771–784, ISSN: 0001-1452, 1533-385X, DOI: 10.2514/3.6275, http://arc.aiaa.org/doi/10.2514/3.6275. 43

[38] Korkegi, R. H. (1975). Comparison of Shock-Induced Two- and Three- Dimensional Incipient Turbulent Seperation. *AIAA Journal*, 13(4):534–535, ISSN: 0001-1452, 1533-385X, DOI: 10.2514/3.49750, http://arc.aiaa.org/doi/10.2514/3.49750. 43

[39] Laurence, S. J., Wagner, A., and Hannemann, K. (2016). Experimental study of second-mode instability growth and breakdown in a hypersonic boundary layer using high-speed schlieren visualization. *Journal of Fluid Mechanics*, 797:471–503, ISSN: 0022-1120, 1469-7645, DOI: 10.1017/jfm.2016.280, https://www.cambridge.org/core/product/identifier/S0022112016002809/type/journal_article. 17, 37

[40] Lockie, A. (2018). Russia's new hypersonic missiles were reportedly leaked to Western spies, infuriating the Kremlin. https://www.businessinsider.com/russias-hypersonic-kinzhal-avangard-reportedly-leaked-to-western-spies-2018-7. 11

[41] Mack, L. M. (1975). Linear Stability Theory and the Problem of Supersonic Boundary-Layer Transition. *AIAA Journal*, 13(3):278–289, ISSN: 0001-1452, 1533-385X, DOI: 10.2514/3.49693, https://arc.aiaa.org/doi/10.2514/3.49693. 21

[42] MacLean, M., Holden, M., and Dufrene, A. (2014). Comparison between CFD and Measurements for Real-gas Effects on Laminar Shockwave Boundary Layer Interaction, I. https://www.cubrc.org/_iassets/docs/CUBRC_laminar_Atlanta.pdf. 22

[43] Malitson, I. H. (1965). Interspecimen Comparison of the Refractive Index of Fused Silica. *Optical Society of America*, 55(10):1205–1209, DOI: https://doi.org/10.1364/JOSA.55.001205, https://www-osapublishing-org.

proxy.lib.utk.edu/DirectPDFAccess/4CB41C4A-09E9-9E59-5F1DCB54F5232A4B_52806/josa-55-10-1205.pdf?da=1&id=52806&seq=0&mobile=no. 29, 30

[44] Mitutoyo (2020). Surftest SJ-210- Series 178-Portable Surface Roughness Tester. https://ecatalog.mitutoyo.com/Surftest-SJ-210-Series-178-Portable-Surface-Roughness-Tester-C1794.aspx. 43

[45] Newport (2020). LBP2-VIS2 Laser Beam Profiler. https://www.newport.com/p/LBP2-VIS2. 52, 54, 96

[46] Norris, G. (2017). Hyper Threat. *Aviation Week & Space Technology*, https://archive.aviationweek.com/issue/20170220. 5

[47] O'Farrell, C. and Martín, M. P. (2009). Chasing eddies and their wall signature in DNS data of turbulent boundary layers. *Journal of Turbulence*, 10:N15, ISSN: 1468-5248, DOI: 10.1080/14685240902852701, http://www.tandfonline.com/doi/abs/10.1080/14685240902852701. 36

[48] Office of the Secretary of Defense (2019). 2019 MISSILE DEFENSE REVIEW. https://www.defense.gov/Portals/1/Interactive/2018/11-2019-Missile-Defense-Review/The%202019%20MDRexecutive%20Summary.pdf. 6, 7

[49] Parziale, N. (2013). *Slender-Body Hypervelocity Boundary-Layer Instability*. PhD Thesis, California Institute of Technology. 36

[50] Parziale, N., Shepherd, J., and Hornung, H. (2012). Reflected Shock Tunnel Noise Measurement by Focused Differential Interferometry. In *42nd AIAA Fluid Dynamics Conference and Exhibit*, New Orleans, Louisiana. American Institute of Aeronautics and Astronautics, ISBN: 978-1-60086-933-4, DOI: 10.2514/6.2012-3261, http://arc.aiaa.org/doi/10.2514/6.2012-3261. 33

[51] Parziale, N. J., Shepherd, J. E., and Hornung, H. G. (2013). Differential Interferometric Measurement of Instability in a Hypervelocity Boundary Layer. *AIAA Journal*, 51(3):750–754, ISSN: 0001-1452, 1533-385X, DOI: 10.2514/1.J052013, http://arc.aiaa.org/doi/10.2514/1.J052013. 33

[52] Photron (2020). FASTCAM SA-Z provides megapixel resolution up to 21,000fps. https://photron.com/fastcam-sa-z/. 56

[53] Pope, A. and Goin, K. L. (1965). *High Speed Wind Tunnel Testing*. John Wiley & Sons, inc. 18

[54] Pope, S. B. and Cambridge University Press (2019). *Turbulent flows*. Cambridge University Press, Cambridge, ISBN: 978-0-521-59125-6 978-0-521-59886-6. OCLC: 1153271725. 21

[55] Salyer, T. R. (2002). *Laser differential interferometry for supersonic blunt body receptivity experiments*. PhD Thesis, Purdue University. 28

[56] Sanderson, S. R. (2005). Simple, adjustable beam splitting element for differential interferometers based on photoelastic birefringence of a prismatic bar. *Review of Scientific Instruments*, 76(11):113703, ISSN: 0034-6748, 1089-7623, DOI: 10.1063/1.2132271, http://aip.scitation.org/doi/10.1063/1.2132271. 31

[57] Sayler, K. M. (2019). Hypersonic Weapons: Background and Issues for Congress. CRS Report R45811, Congressional Research Service. 6, 7, 8, 9, 10, 11

[58] Schlichting, H. and Gersten, K. (2016). *Boundary-layer theory*. Springer Berlin Heidelberg, New York, NY, 9 edition, ISBN: 978-3-662-52917-1. 13

[59] Schmisseur, J. D. (2015). Hypersonics into the 21st century: A perspective on AFOSR-sponsored research in aerothermodynamics. *Progress in Aerospace Sciences*, 72:3–16, ISSN: 03760421, DOI: 10.1016/j.paerosci.2014.09.009, https://linkinghub.elsevier.com/retrieve/pii/S0376042114000980. 9, 10, 12, 20

[60] Schneider, S. P. (2015). Developing mechanism-based methods for estimating hypersonic boundary-layer transition in flight: The role of quiet tunnels. *Progress in Aerospace Sciences*, 72:17–29, ISSN: 0376-0421, DOI: 10.1016/j.paerosci.2014.09.008, http://www.sciencedirect.com/science/article/pii/S0376042114000876. 21

[61] Schwartzentruber, T. E., Scalabrin, L. C., and Boyd, I. D. (2008). Hybrid Particle-Continuum Simulations of Hypersonic Flow Over a Hollow-Cylinder-Flare Geometry. *AIAA Journal*, 46(8):2086–2095, ISSN: 0001-1452, 1533-385X, DOI: 10.2514/1.36681, http://arc.aiaa.org/doi/10.2514/1.36681. 22

[62] Settles, G. S. (2001). *Schlieren and shadowgraph techniques: visualizing phenomena in transparent media*. Experimental Fluid Mechanics. Springer, Berlin Heidelberg, softcover reprint of the hardcover 1st edition 2001 edition, ISBN: 978-3-642-63034-7. OCLC: 248149245. 37, 82

[63] Shinkman, P. D. (2020). China, U.S. Escalate Forces, Threats in South China Sea. *US News & World Report*, https://www.usnews.com/news/world-report/articles/2020-07-20/china-us-escalate-forces-threats-in-south-china-sea. 7

[64] Smeets, G. and George, A. (1996). Laser-Differential Interferometer Applications in Gas Dynamics. DEFENSE TECHNICAL INFORMATION CENTER ADA307459, DEFENSE TECHNICAL INFORMATION CENTER. 24, 25, 26, 29, 31, 33, 36

[65] Speier, R. H., Nacouzi, G., Carrie, L., and Moore, R. M. (2017). *Hypersonic missile nonproliferation: hindering the spread of a new class of weapons*. RAND Corporation, Santa Monica, CA, https://www.rand.org/pubs/research_reports/RR2137.html. 7, 8, 9, 10

[66] Thorlabs (2020a). DMLP567L Ø2" Longpass Dichroic Mirror, 567 nm Cut-On. https://www.thorlabs.com/thorproduct.cfm?partnumber=DMLP567L. 49

[67] Thorlabs (2020b). HNL050LB HeNe Laser, 632.8 nm, 5 mW, Polarized, 100 - 240 VAC Power Supply Included. https://www.thorlabs.com/thorproduct.cfm?partnumber=HNL050LB. 48, 49

[68] Thorlabs (2020c). LA1353 N-BK7 Plano-Convex Lens, Ø75.0 mm, f = 200 mm, Uncoated. https://www.thorlabs.com/thorproduct.cfm?partnumber=LA1353. 49

[69] Thorlabs (2020d). LC1715 N-BK7 Plano-Concave Lens, Ø1", f = -50.0 mm, Uncoated. https://www.thorlabs.com/thorproduct.cfm?partnumber=LC1715. 49

[70] Thorlabs (2020e). LD2568 N-SF11 Bi-Concave Lens, Ø9 mm, f = -9.0 mm, Uncoated. https://www.thorlabs.com/thorproduct.cfm?partnumber=LD2568. 49

[71] Thorlabs (2020f). LPVISE100-A Ø1" Linear Polarizer with N-BK7 Windows, 400-700 nm. https://www.thorlabs.com/thorproduct.cfm?partnumber=LPVISE100-A. 49

[72] Thorlabs (2020g). LPVISE200-A Ø2" Linear Polarizer with N-BK7 Windows, 400-700 nm. https://www.thorlabs.com/thorproduct.cfm?partnumber=LPVISE200-A. 49

[73] Thorlabs (2020h). MT1 1/2" Translation Stage with Standard Micrometer, 1/4"-20 Taps. https://www.thorlabs.com/thorproduct.cfm?partnumber=MT1#ad-image-0. 96

[74] Thorlabs (2020i). PDA10A2 Si Fixed Gain Detector, 200 - 1100 nm, 150 MHz BW, 0.8 $mm^2$, Universal 8-32 / M4 Taps. https://www.thorlabs.com/thorproduct.cfm?partnumber=PDA10A2. 58

[75] Thorlabs (2020j). PDA36A2 Si Switchable Gain Detector, 350 - 1100 nm, 12 MHz BW, 13 $mm^2$, Universal 8-32 / M4 Taps. https://www.thorlabs.com/thorproduct.cfm?partnumber=PDA36A2. 48, 49, 56

[76] US Air Force (2020). X-15 in flight. https://www.edwards.af.mil/News/Photos/igphoto/2001667598/. 1, 2

[77] Vavasseur, X. (2020). Analysis: Russia's Tsirkon Hypersonic Missile Trials Enter Final Stage – Part 2. https://www.navalnews.com/naval-news/2020/03/analysis-russias-tsirkon-hypersonic-missile-trials-enter-final-stage-part-2/. 11

[78] Vergun, D. (2019). Freedom of Navigation in South China Sea Critical to Prosperity, Says Indo-Pacific Command. https://www.defense.gov/Explore/News/Article/Article/2025105/freedom-of-navigation-in-south-china-sea-critical-to-prosperity-says-indo-pacif/. 7

[79] Wadhams, T., Holden, M., and MacLean, M. (2014). Comparisons of Experimental and Computational Results from "Blind" Turbulent Shock Wave Interaction Study Over Cone Flare and Hollow Cylinder Flare Configurations. 22

[80] White, F. M. (2006). *Viscous fluid flow*. McGraw-Hill Higher Education, Boston; Montreal, 3 edition, ISBN: 978-0-07-240231-5. OCLC: 693819619. 22

# Appendices

# A Setup and Alignment of FLDI

Setup of a 2-point FLDI system should proceed as follows. First, mount the optical rails and other optomechanics on either side of the test section, as close to the windows as can be reasonably achieved without scratching them. The rails must be entirely aligned in the $x$ and $y$ axes and rotationally in $\alpha, \beta,$ and $\gamma$. This can most easily be dialed in by mounting the laser and running an iris or target along the rails. The laser is first aligned with the 'send' rail.leaving room for all send side optical components, and then the 'receive' rail is aligned to the laser. A level or laser-level may also be helpful, although it is not inherently necessary for the rails to be level, just aligned. With the rails and laser in place, the field lenses should be installed as close to the tunnel windows as possible. Note that excessive space between the field lenses and the tunnel walls will negatively effect the FLDIs ability to filter noise generated by the walls [26, p. 83]. Install the 'send' side lens first, checking that the laser hits it centered and normal by checking that the reflection returns to the laser and at the expanded laser on the 'receive' side is still centered on the iris or target, then install the 'receive' side lens similarly. Next, mount the expanding lens, creating the 'double-diamond' shape of the FLDI. If a small ($<$1 in) optic is being used, as in this study, extreme precision is required in its $x, y$, and rotational positioning, in order to prevent diffraction, suggesting the use of a high precision stage, e.g. Thorlabs MT1 [73]. Place it so that the focal point of the whole FLDI is approximately in the center of the region of interest (this will be adjusted later). A laser beam profiler makes the alignment of all off the lenses somewhat more straightforward. The Newport LBP2-VIS2 beam-profiler [45] was used here.

With the majority of the lenses in place, it is time to place the Wollaston prisms. Place both Wollaston prisms 1 focal length away from their respective field lens. Their x and y positions are not important if the laser is wholly within them. The 'receive' side Wollaston prism will need to be finely adjustable in $z$ and $x$ [1]with a range of several inches, and coarsely adjustable in $z$ (along the rail). Ensure that the refraction of the Wollaston prisms is in plane with the optical rails. Then, to create the two point interferometer, install the large angle Wollaston after the expanding lens and then a polarizer large enough for the expanded beam

to pass through. Position the expanding lens and the large angle Wollaston prism so that the focal point of the FLDI is on the centerline of the tunnel.

The rotational position of the laser and first polarizer are adjusted so that the intensity of the 4 points in the test section are equal. This will be achieved when the laser light is polarized to 45° to the wide angle Wollaston prism, and the first polarizer has its axis aligned halfway between the polarizations of light leaving the first Wollaston prism, i.e. at 45° or 135°. Then, the final polarizer is adjusted until interference is observed. Finally, the last Wollaston prism's position is adjusted for system sensitivity based on the output of the photo-diodes.

[1]Fine adjustment of the second Wollaston prism in $x$ will be used to adjust the phase shift in the beams of the FLDI (see section 2.2.1, page 31).

# B FLDI Processing Code

All FLDI data processing code is available at https://github.com/JackCobourn/FLDI, and can be cloned with `Git`, or by contacting the author at jcobourn@utk.edu

# Vita

Jack Cobourn was born in Ann Arbor, MI and grew up in Phoenix, AZ. He graduated from Veritas Preparatory Academy in 2014. He then attended Lafayette College in Easton, PA, where he attained a B.S. in Mechanical Engineering and a B.A. in Russian and Eastern European Studies in 2018. Jack enjoys hiking and cooking. He currently lives in Tullahoma, TN with his two cats, Rey and Finn.